UNIVERSIDADE ESTADUAL PAULISTA “JÚLIO DE MESQUITA FILHO”
FACULDADE DE ENGENHARIA
CAMPUS DE ILHA SOLTEIRA

LARISSA DREWS WAYHS LOPES

INFLUENCE OF CONTROL SURFACE FREEPLAY ON LIMIT CYCLE OSCILLATIONS IN AEROELASTIC SYSTEMS

ILHA SOLTEIRA
2023

LARISSA DREWS WAYHS LOPES

INFLUENCE OF CONTROL SURFACE FREEPLAY ON LIMIT CYCLE OSCILLATIONS IN AEROELASTIC SYSTEMS

Thesis submitted to the Faculdade de Engenharia de Ilha Solteira - UNESP in partial fulfillment of the requirements for obtaining the Doctorate degree in Mechanical Engineering. Knowledge area: Solid Mechanics

Advisor: Prof. Dr. Douglas Domingues Bueno

ILHA SOLTEIRA
2023

FICHA CATALOGRÁFICA
Desenvolvido pelo Serviço Técnico de Biblioteca e Documentação

W357i

Wayhs-Lopes, Larissa Drews.
Influence of control surface freeplay on limit cycle oscillations in aeroelastic systems / Larissa Drews Wayhs-Lopes. -- Ilha Solteira: [s.n.], 2023
139 f. : il.

Tese (doutorado) - Universidade Estadual Paulista. Faculdade de Engenharia de Ilha Solteira. Área de conhecimento: Mecânica dos Sólidos, 2023

Orientador: Douglas Domingues Bueno
Inclui bibliografia

1. Freeplay. 2. Limit cycle oscillations. 3. Extended Hénon'S technique. 4. Describing function. 5. Equivalent linearization technique. 6. Coulomb friction.

Elaborada por Raiane da Silva Santos - CRB-8/9999

UNIVERSIDADE ESTADUAL PAULISTA

Câmpus de Ilha Solteira

CERTIFICADO DE APROVAÇÃO

TÍTULO DA TESE: INFLUENCE OF CONTROL SURFACE FREEPLAY ON LIMIT CYCLE OSCILLATIONS IN AEROELASTIC SYSTEMS

AUTORA: LARISSA DREWS WAYHS LOPES

ORIENTADOR: DOUGLAS DOMINGUES BUENO

Aprovada como parte das exigências para obtenção do Título de Doutora em Engenharia Mecânica, área: Mecânica dos Sólidos pela Comissão Examinadora:

Prof. Dr. DOUGLAS DOMINGUES BUENO (Participaçao Virtual)
Departamento de Matematica / Faculdade de Engenharia de Ilha Solteira - UNESP

Prof. Dr. LEONARDO SANCHES (Participaçao Virtual)
Departamento de Mecânica, Estruturas e Materiais / Institut Supérieur de l'Aéronautique et de l'Espace, ISAE, França

Prof. Dr. MARCIO ANTONIO BAZANI (Participaçao Virtual)
Departamento de Engenharia Mecânica / Faculdade de Engenharia de Ilha Solteira - UNESP

Prof. Dr. RODOLFO ANDRÉ KUCHE SANCHES (Participaçao Virtual)
Departamento de Engenharia de Estruturas / Universidade de São Paulo / USP

Professor Associado LEOPOLDO PISANELLI RODRIGUES DE OLIVEIRA (Participaçao Virtual)
Departamento de Engenharia Mecânica / Universidade de São Paulo - USP

Ilha Solteira, 31 de agosto de 2023

To my amazing husband and best friend, Kayc,
and to my beloved parents, Ricardo and Márcia

Acknowledgments

First of all, I would like to express my gratitude to God for the complexity and perfection of nature's mechanisms, the curiosity, health, persistence, and learning ability that have been bestowed upon me.

I am also grateful to my advisor Prof. Dr. Douglas D. Bueno, for the opportunity to work with him since my undergraduate studies. I appreciate all the technical and emotional support he has provided me with, as well as his encouragement and trust in me to carry out this research. I am also thankful for the international doors he has opened for me.

I would also like to acknowledge and thank Prof. Dr. Earl H. Dowell for his contributions and helpful technical comments during my short-term internship at Duke University. I am deeply grateful to Prof. Dr. Carlos E. S. Cesnik for the opportunity to work with him for a full year at the University of Michigan, where I gained numerous new experiences in both professional and personal areas. It was truly a year of growth for me.

I extend my gratitude to the São Paulo Research Foundation (FAPESP) for the support given to me since 2017 (grant number 2017/08008-1), as well as for the Direct Doctorate period (grant number 2019/22730-7). I also appreciate the funding I received for two scholarships to research abroad, at Duke University in 2019 (grant number 2018/23348-6) and at the University of Michigan in 2022-2023 (grant number 2021/12383-8).

I am grateful for the people in my life during these years. This research faced four different periods. Regarding the time before the pandemic, I would like to thank Renan for being there for me every day in the lab, sharing the same experiences regarding research. I thank my friends Mari and Douglas, Gi and Jessé, Joyce, Dani, Simone, and Mari for the great times in Ilha Solteira that gave me strength to stay steady.

Regarding the time I spent abroad, I appreciate all the special new friendships Michigan gave me, such as Thiagão and Sâmila, Thiago and Camila, Bernardo, Jasmine, Braden, and Patrizio. I give special thanks to Divya for always being there to help. I also particularly thank Ana and Bilal for all the adventures we shared in Michigan. Elisa and Charles have a special place in my heart, and I thank them for being our Michigan parents and sharing great moments with us.

As for the time I spent in Brazil after the pandemic, I am thankful for the kind new friends that God gave me, Mateus, Fernanda, Rafa, and Belinha. They were of great help during the period of completing this thesis. I am also grateful to my friend Clara for giving me joy and support during an amazing week close to the end of this cycle. Besides, I give special thanks to my husband's family, Sueli and Gláucio, Kaio, Carla, Cauana, Iggor and Leo, for being there for me. We shared several happy moments around the table with delicious food and nice talk.

For those who provided me with important support, joy, and love - essential to this research - with a special role during the pandemic, I sincerely thank my parents and sisters, Ricardo and Márcia, Gabriela, and Bárbara. They have been present in all stages of this research, giving me strength and recharging my energy whenever I needed it. I could not have gone through these years without them.

Finally, to the one who has *always* stood by my side, accompanying me on countless outdoor walks while I poured out my frustrations and joys about this research (many many times), and with whom I have shared moments of happiness, tears, and celebration, I am profoundly grateful to my husband, Kayc. His care, immense support, encouragement, and immeasurable love have enriched my life in ways words cannot capture, and continue to do so.

With my best thanks,

Larissa

''Commit to the LORD whatever you do, and He will establish your plans"

Proverbs 16:3

Abstract

The nonlinear aeroelasticity is an important field and stability analysis is part of the requirements to certificate aircraft. Specifically, freeplay is a discontinuous nonlinearity commonly appearing in hinge connections of control surfaces and it can change the stability of the system by generating limit cycle oscillations (LCOs), which may be detrimental to the structure in terms of fatigue. The present work is focused on the important first step of performing LCO prediction, which involves predicting the amplitude and frequency of motion that occurs for each particular flight condition. Then, the main focus of this research is to improve conventional numerical methods to address the aeroelastic analysis considering freeplay. The main contributions include an improved Hénon's technique for time marching solutions and, regarding frequency domain, a new way of looking to the combination of describing functions with the eigenvalue analysis of an equivalent aeroelastic system. A general formulation in matrix form is proposed to the Hénon's technique to include discontinuous nonlinearities in any desired degree of freedom (DOF). Two physical applications are presented, one involving a 3-DOF airfoil with asymmetric freeplay and solid friction in the control surface hinge; and also a 4-DOF airfoil with freeplay in two hinges of trailing edge control surfaces. This formulation includes an event location method, and it is used to capture extremes during the time integration, useful to detect LCO, to plot bifurcation diagrams, and also to plot Poincarè sections. In addition, two new describing functions are proposed, such that a first one predicts the first and third LCO harmonics for systems with freeplay, and the other one considers freeplay and friction in the control surface hinge. Theoretical results demonstrate that the proposed approaches contribute to investigate aeroelastic systems with discontinuous nonlinearities.

Keywords: Freeplay. Limit Cycle Oscillations. Extended Hénon's Technique. Describing Function. Equivalent Linearization Technique. Coulomb Friction. Multiple Harmonics. Combined Discontinuous Nonlinearities.

Resumo

Aeroelasticidade não-linear é um campo de importância atual e a análise de estabilidade é parte dos requisitos para certificar aeronaves. Especificamente, folga geométrica é uma não-linearidade descontínua comumente observadas nas conexões de superfícies de controle, e pode alterar a estabilidade do sistema gerando oscilações de ciclo limite (LCOs), tipicamente prejudiciais à estrutura, inclusive em termos de fadiga. O presente trabalho é focado na importante etapa de previsão da LCO. Isso envolve prever a amplitude e a frequência do movimento para condições de voo específicas. O foco principal desta pesquisa é aprimorar métodos numéricos convencionais para superar as dificuldades geradas pela descontinuidade da folga. As principais contribuições incluem melhorias na técnica de Hénon para soluções no tempo e, no domínio da frequência, uma nova forma combinar funções descritivas com a análise de autovalores de um sistema aeroelástico equivalente. Uma formulação geral na forma de matriz é proposta para a técnica de Hénon, permitindo a inclusão de diferentes não-linearidades descontínuas,em qualquer grau de liberdade arbitrário. Duas aplicações físicas são apresentadas, uma envolvendo um aerofólio de três graus de liberdade com folga assimétrica e atrito na conexão da superfície de controle; e também um aerofólio com quatro graus é investigado com folga em duas conexões de superfícies de controle do bordo de fuga. Esta formulação também permite usar a técnica como um método de localização de eventos, e é utilizada neste trabalho para capturar pontos extremos durante a integração de tempo, tipicamente útil para detectar LCO, construir diagramas de bifurcação, e também as seções de Poincarè. Além disso, duas novas funções descritivas são propostas, sendo uma para prever o primeiro e terceiro harmônicos de um sistema com folga, e a outra para considerar folga e atrito na conexão da superfície de controle. Resultados teóricos demonstram que as estratégias propostas contribuem para investigar sistemas aeroelásticos com não-linearidade descontínua.

Palavras-chave: Folga. Oscilação de Ciclo Limite. Técnica de Hénon Estendida. Função Descritiva. Técnica de Linearização Equivalente. Atrito de Coulomb. Múltiplos Harmônicos. Não-Linearidades Descontínuas Combinadas.

List of Figures

List of Tables

List of Acronyms

AC	-	Advisory Circular (p.32)
CS	-	Control Surface (p.46)
DF	-	Describing Function (p.36)
DOF	-	Degree of Freedom (p.33)
ELT	-	Equivalent Linearization Technique (p.39)
FAA	-	Federal Aviation Administration (p.32)
H	-	Hénon's Technique applied for both freeplay and friction (p.64)
HB	-	Harmonic Balance (p.38)
HB3-ELT	-	Harmonic Balance method including the third harmonic combined with Equivalent Linearization Technique (p.75)
HF	-	Hénon's Technique applied for freeplay only (p.64)
HOHB	-	High Order Harmonic Balance (p.39)
iterative-ELT	-	refers to the iterative procedure of the Equivalent Linearization Technique to use the DF for combined friction and freeplay (p.75)
LCO	-	Limit Cycle Oscillation (p.31)
MGCS	-	Modified Generalized Coordinate System (p.61)
MIL-A	-	Military Specification A (p.32)
NASTRAN	-	NASA Structure Analysis (p.89)
ODE	-	Ordinary Differential Equation (p.36)
RFA	-	Rational Functions Approximation (p.52)
RK	-	classical Runge-Kutta method (p.62)
w.r.t	-	with respect to (p.54)

List of Symbols

$(\ )_k$	-	refers to the k-th row where the state generating discontinuity is located (p.57)
$(\ )^l$, $(\ )_l$	-	superscript and subscript l relates to features of the l-th degree of freedom (part of $\mathbf{u}$) presenting the nonlinearity (freeplay or friction) (p.46)
$(\ )_r$	-	refers to the r-th structural mode, associated to the mode of u_l (p.61)
$(\dot{\ })$, $(\ddot{\ })$	-	first and second derivative of ( ) with respect to time
$(\ )'$	-	first derivative of ( ) with respect to x_k
$(\hat{\ })$	-	indicates the linear equivalent term associated to the exact ( ) (p.75)
$(\ )^T$	-	transpose matrix of ( )
A_c, B_c	-	two intervals for the variable generating discontinuity $x_{k_c} = x_k = \dot{u}_l$ due to friction (p.60)
A_δ, B_δ, C_δ	-	three intervals for the variable generating discontinuity $x_{k_\delta} = x_k = u_l$ due to freeplay (p.57)
$\mathcal{A}_1, \mathcal{A}_2, \mathcal{A}_3$	-	indicate particular configurations of airfoils (p.55)

Scalars

C	-	amplitude of the friction torque (p.47)
C_T	-	generalized function of Theodorsen that brings the circulatory nature (p.51)
$\hat{d}_{u_l}$	-	equivalent structural damping of u_l (p.85, Eq. 20). When acting in CS, $\hat{d}_\beta$ is used (p.68)
D_{LCO}	-	scalar defined in Eq. 15 to detect two identical packages (p.72)
$E_j^{(i)}$	-	the i-th element of E_j (p.72)
f	-	the frequency in Hertz obtained as $\Im(\lambda)/(2\pi)$ (p.77)

$f_{(\,)}$	-	the fundamental frequency of motion. It can be either f_1 when obtained from time response or $f_{g=0}$ when obtained from eigenvalue extraction (Fig. 21, 30, 35)
f_1	-	the fundamental frequency of motion obtained when the Fast Fourier Transform is applied to the time response (p.68)
f_1^β	-	f_1 obtained by analyzing the CS response (p.110)
f_1^γ	-	f_1 obtained by analyzing the tab response (p.110)
f_F	-	flutter frequency of the linear (nominal) system (without freeplay, or outside of freeplay) (Fig. 20)
$f_{g=0}$	-	frequency in Hertz, i.e., $\Im(\lambda)/(2\pi)$ where $g = 0$ (marginally stable condition) (Fig. 20)
$\bar{f}_i$	-	the linear coefficient of the line equation of $f_{l,i}^\delta$ (p.136, Tab. 6)
f_l^C	-	the nonlinear torque acting on u_l due to Coulomb friction (p.47)
$f_{l,i}^C$	-	expression of f_l^C for the i-th region of non-zero f_l^C (p.136, Tab. 6)
$\hat{f}_l^C$	-	the linear equivalent restorative torque acting on u_l due to friction (p.85)
f_l^δ	-	the nonlinear restorative torque acting on u_l referring to the stiffness modified by freeplay (p.46)
$f_{l,i}^\delta$	-	expression of f_l^δ for the i-th region of non-zero f_l^δ (p.136, Tab. 6)
$\hat{f}_l^\delta$	-	the linear equivalent restorative torque acting on u_l due to freeplay (p.75)
f_r	-	the frequency range used when the Fast Fourier Transform is applied to the time response (p.68)
F_0	-	coefficients of the Fourier series applied to f_l^δ to write $\hat{f}_l^\delta$ (p.75)
F_1	-	the first harmonic of the Fourier series applied to f_l^δ to write $\hat{f}_l^\delta$ (p.77, Eq. 43, 47)
F_3	-	the third harmonic of the Fourier series applied to f_l^δ to write $\hat{f}_l^\delta$ (p.83, Eq. 17, 48)
$F_{c_1}^C$	-	the first harmonic of the Fourier series applied to f_l^C to write $\hat{f}_l^C$ (p.85, Eq. 44)
F_{c_n}, F_{s_n}	-	the coefficients multiplying $\cos(n\theta)$ and $\sin(n\theta)$, respectively, of the Fourier series applied to f_l^δ to write $\hat{f}_l^\delta$ (p.75)
$F_{c_n}^C, F_{s_n}^C$	-	the coefficients multiplying $\cos(n\theta)$ and $\sin(n\theta)$, respectively, of the Fourier series applied to f_l^C to write $\hat{f}_l^C$ (p.75)
$F_{c_n,i}, F_{s_n,i}$	-	parcels of F_{c_n} and F_{s_n}, respectively, for the i-th region of non-zero f_l^δ (p.136)

F_n	-	lighter notation for F_{s_n} (p.75)
$\bar{F}_n$	-	defined as $F_n/(k_{u_l}\delta)$, it is the non-dimensional value for F_n (p.77, Eq. 17)
g	-	non-dimensional real part of the eigenvalue λ, defined as $\Re(\lambda)/\lvert\lambda\rvert$ (p.77, 81)
g_i	-	value of g when $V = V_i$ (p.86)
h_j	-	the value of $\mathbf{h}$ at the j-th row, for $j = 1, ..., N$ (p.59)
$\tilde{h}_j$	-	the value of $\tilde{\mathbf{h}}$ at the j-th row, for $j = 1, ..., N$ (p.59)
i_c	-	number of the non-zero f_l^C region (Fig. 23)
i_δ	-	number of the non-zero f_l^δ region (Fig. 23)
j	-	when not subscripted, it is the pure imaginary number $\sqrt{-1}$ (p.51)
k	-	when not subscripted, it is the reduced frequency, $\omega b/V$ (p.51)
k_c	-	is the value of subscript k when dealing with friction nonlinearity ($k_c = l$) (p.60)
$\bar{k}_i$	-	the angular coefficient of the line equation of $f_{l,i}^\delta$ (p.136, Tab. 6)
k_{u_l}	-	stiffness of u_l (p.46)
$\hat{k}_{u_l}$	-	the linear equivalent stiffness acting on u_l (p.75)
k_δ	-	the value of subscript k when dealing with freeplay nonlinearity ($k_\delta = n_{\mathrm{dof}} + l$) (p.57)
M_β	-	angular moment resulting from aerodynamics acting on CS (p.76)
n_{dof}	-	number of degrees of freedom (p.46)
n_{lag}	-	number of aerodynamic lag parameters (p.52)
n_{tru}	-	number of modes used to truncate the system (p.60)
N	-	number of states (order of the dynamic matrix when the first order equation is used to describe the system) (p.52)
N_{reg}	-	number of sub-linear regions in a complete period from 0 to 2π where the nonlinearity effort is not zero (f_l^δ for freeplay, and f_l^C for friction) (p.136)
p	-	defined herein as the ratio $\hat{k}_{u_l}/k_{u_l}$ (p.77)
p_j	-	the j-th value of p in the range $0 < p < 1$ (p.84)
p_R	-	defined herein as the ratio $\delta_R^\beta/(\delta_R^\beta + \delta_L^\beta)$ (p.65)
q	-	dynamic pressure, $\rho V^2/2$ (p.51)
R	-	ratio between freeplay on tab with respect to freeplay on CS, defined herein as $\delta^\gamma/\delta^\beta$ (p.106)
s	-	Laplace variable, ωj (p.51)
$\tilde{s}$	-	modified Laplace variable, kj (p.51)

s_v - discrete integration step of the independent variable (p.57)

t - time in seconds (p.46)

t_i - the i-th time instant (p.57)

Δt - regular time integration step (p.57)

$\Delta \tilde{t}$ - time between t_i and the switching point (p.58)

u_i^ϕ - the i-th generalized displacement of $\mathbf{u}_\phi$, for $i = 0, ..., n_{\mathrm{dof}}$ (p.61)

u_l - the l-th degree of freedom in $\mathbf{u}$ (p.46)

$\dot{u}_l$ - velocity of the l-th degree of freedom (p.47)

$\hat{u}_l$ - mathematical expression composed by harmonic functions to describe the expected LCO (p.75)

U_1 - amplitude of the first harmonic of the assumed LCO $\hat{u}_l$ (p.77)

U_3 - amplitude of the third harmonic of the assumed LCO $\hat{u}_l$ (p.82)

U_n - the coefficients multiplying $\sin(n\theta)$ for the assumed LCO $\hat{u}_l$ indicating the amplitude of the n-th harmonic (Fig. 18)

$\bar{U}_n$ - non-dimensional amplitude of the n-th harmonic of the assumed LCO $\hat{u}_l$, defined as U_n/δ (p.77, Eq. 17)

v - independent variable of a generic dynamic system (p.57)

v_i - i-th value of the independent variable (p.57)

V - airspeed or flow velocity (p.52)

V_0 - airspeed for $i = 0$ either when performing iterative-ELT (p.86) or in the context of bifurcation diagrams constructed with time simulations (p.107)

V_F - flutter velocity of the linear (nominal) system (without freeplay, or outside of freeplay) (p.75)

V_{F1}^β - first airspeed for where there is some $g = 0$ for the sub-linear system of the airfoil $\mathcal{A}_3$ when inside of CS freeplay only (Tab. 5)

$V_{F1}^\gamma, V_{F2}^\gamma, V_{F3}^\gamma$ - first, second and third airspeeds for where there is some $g = 0$ for the sub-linear system of the airfoil $\mathcal{A}_3$ when inside of tab freeplay only (Tab. 5)

$V_{g=0}$ - airspeed where $g = 0$ (marginally stable condition) (Fig. 19)

V_i, V_{i+1} - the i-th and the $(i+1)$-th airspeeds, where the time simulation for V_i is run before than the simulation for V_{i+1} (p.72)

V_{max} - maximum airspeed considered for time domain simulation (p.72)

V_{min} - minimum airspeed considered for time domain simulation (p.72)

V_{sea} - airspeed at sea level (p.81)

V_{sta} - airspeed to start the iterative-ELT procedure of eigenvalues extraction (p.86)

V_{sto} - maximum airspeed considered for the iterative-ELT procedure of eigenvalues extraction (p.86)

$\bar{V}_{(\ )}^{(\ )}$ - non-dimensional airspeed $V_{(\ )}^{(\ )}/V_F$ (Tab. 5)

ΔV - airspeed step considered for either time domain simulations to construct bifurcation diagrams (p.72) or for iterative-ELT (p.86)

x_k - the k-th state in $\mathbf{x}$. It is the variable generating discontinuity (p.57)

x_{k_c} - x_k when dealing with friction nonlinearity (p.60)

$x_{k,i}$ - x_k at $t = t_i$ (p.59)

x_k^{sp} - x_k at the switching point (p.59)

x_{k_δ} - x_k when dealing with freeplay nonlinearity (p.57)

$\tilde{x}_{k_\delta}$ - the k_δ-th state in $\tilde{\mathbf{x}}$ (which is time) (p.58)

Δx_k - step in variable x_k from time t_i to the switching point (p.59)

β^0 - value of β when $t = 0$ (p.107)

β_L - modulus of the CS inversion point on the negative side when in steady state motion (p.65)

β_R - modulus of the CS inversion point on the positive side when in steady state motion (p.65)

β_{tot} - total LCO amplitude, defined as $\beta_R + \beta_L$ (p.66)

$\beta_{\dot{\beta}=0}$ - inversion point (extreme) of CS, i.e., value of β when $\dot{\beta} = 0$ (Fig. 10)

$\bar{\beta}$ - middle position between inversion points, defined as $[\beta_R + (-\beta_L)]/2$ (p.66)

γ^0 - value of γ when $t = 0$ (p.107)

$\gamma_{\dot{\gamma}=0}$ - inversion point (extreme) of tab, i.e., value of γ when $\dot{\gamma} = 0$ (Fig. 37)

δ - lighter notation of δ^l used in chapter 4 (p.76)

δ^l - freeplay boundary of u_l (in module), particularly when freeplay is symmetric $\delta^l = \delta_R^l = \delta_L^l$ (p.47)

δ_L - lighter notation of δ_L^l (p.57)

δ_L^l - freeplay boundary of u_l (in module) on the negative (or left) side (p.46)

δ_R - lighter notation of δ_R^l (p.57)

δ_R^l	-	freeplay boundary of u_l (in module) on the positive (or right) side (p.46)
$\bar{\delta}$	-	geometric center of freeplay, defined as $[\delta_R^\beta + (-\delta_L^\beta)]/2$ (p.66)
δ_{tot}	-	total LCO amplitude, defined as $\delta_R^\beta + \delta_L^\beta$ (p.66)
ϵ	-	tolerance to consider convergence of iterative-ELT (p.86)
ϵ_{LCO}	-	tolerance to consider two packages as identical (p.72)
ε	-	tolerance to consider convergence of Newton-Raphson (Eq. 19)
θ	-	reduced time defined as $\omega_{u_l} t$ (p.75)
θ_δ	-	value of θ when $\hat{u}_l = \delta$ (p.76)
$\theta_{\delta 1}$	-	first value of θ when $\hat{u}_l = \delta$, when first and third harmonic are assumed (p.83)
$\theta_{\delta 2}$	-	second value of θ when $\hat{u}_l = \delta$, when first and third harmonic are assumed (p.83)
λ	-	a generic eigenvalue of $\hat{\mathbf{A}}$ (p.77)
ξ_{eq}	-	equivalent damping ratio (p.68)
ρ	-	air density (p.52)
ρ_i	-	air density at the i-th flight condition (in this work, fixed at ρ_{sea}) (p.81)
ρ_{sea}	-	air density at sea level (1.225 kg/m^3) (p.81)
ϱ	-	lag parameter (p.52)
ϕ_{ij}	-	the element of $\mathbf{\Phi}$ in the i-th row and j-th column (p.61)
ω	-	fundamental frequency of motion in rad/s (p.51)
ω^0	-	initial guess for ω_{u_l} in rad/s used in iterative-ELT (p.86)
ω_{u_l}	-	frequency of the first (fundamental) harmonic of the assumed LCO $\hat{u}_l$ in rad/s, obtained as the imaginary part of the eigenvalue with $g = 0$ (p.76)

Vectors

$\mathbf{b}_l^C$	-	$N \times 1$ vector of zeros with $\mathbf{M}_a^{-1}\mathbf{f}_l^C$ in the first n_{dof} rows (Eq. 11)
$\mathbf{b}_l^\delta$	-	$N \times 1$ vector of zeros with $\mathbf{M}_a^{-1}\mathbf{f}_l^\delta$ in the first n_{dof} rows (Eq. 11)
$\bar{\mathbf{b}}^\delta$	-	$N \times 1$ vector of state space equation - for a particular sub-linear system - with parcels not involving any state and including effect of all combined freeplays (p.100, Tab. 4)
$\bar{\mathbf{b}}_l^\delta$	-	$N \times 1$ vector with the parcels of $\mathbf{b}_l^\delta$ not involving any state (p.99)

E_j	-	computational vector indicating the j-th package with 50 consecutive extremes of u_l (p.71)
$\mathbf{f}_l^C$	-	$n_{\text{dof}} \times 1$ vector of zeros with f_C^l in the l-th row (Eq. 3)
$\mathbf{f}_l^\delta$	-	$n_{\text{dof}} \times 1$ vector of zeros with f_δ^l in the l-th row (Eq. 3)
$F(v, \mathbf{y})$	-	function defining the particular explicit numerical integration method (p.57)
$\mathbf{F}(\mathbf{z})$	-	algebraic system defining the new describing function to consider the third harmonic (Eq. 17)
$\mathbf{F}_a(t)$	-	$n_{\text{dof}} \times 1$ vector of unsteady aerodynamics written in time domain (p.49, Eq. 8)
$\mathbf{F}_a(s)$	-	$n_{\text{dof}} \times 1$ vector of unsteady aerodynamics written in frequency domain (p.49, Eq. 8)
$\mathbf{g}(v, \mathbf{y})$	-	function describing the generic dynamic system which returns a vector $\dot{\mathbf{y}} = \mathbf{g}(v, \mathbf{y})$ (p.57)
$\mathbf{h}(t, \mathbf{x})$	-	function describing the aeroelastic system in time domain which returns a vector $\dot{\mathbf{x}} = \mathbf{h}(t, \mathbf{x})$ (p.57)
$\tilde{\mathbf{h}}(x_k, \tilde{\mathbf{x}})$	-	function describing the modified system to perform Hénon iteration in the independent variable x_k which returns a vector $\tilde{\mathbf{x}}' = \tilde{\mathbf{h}}(x_k, \tilde{\mathbf{x}})$ (p.59, Eq. 13)
$\mathbf{k}_j$	-	different approximations for the first derivative $\dot{\mathbf{y}}$ in Runge-Kutta methods (p.57, Eq. 38, 39)
$\hat{\mathbf{q}}$	-	$(n_{\text{lag}} + 1)n_{\text{dof}} \times 1$ vector with the harmonic expressions for the degrees of freedom of $\mathbf{u}$ and for the aerodynamic states of Eq. (9) (p.76)
$\mathbf{q}_{c_n}, \mathbf{q}_{s_n}$	-	$(n_{\text{lag}} + 1)n_{\text{dof}} \times 1$ vector with the harmonic amplitudes for the degrees of freedom of $\mathbf{u}$ and for the aerodynamic states of Eq. (9) (p.76)
$\mathbf{R}$	-	$n_{\text{dof}} \times 1$ vector, part of the aerodynamic efforts that multiply the constant C_T, i.e., it appears in circulatory terms (p.51, 129)
$\mathbf{S}_1$	-	$1 \times n_{\text{dof}}$ vector, part of the aerodynamic circulatory terms that multiply $\mathbf{u}$ (p.51, 129)
$\mathbf{S}_2$	-	$1 \times n_{\text{dof}}$ vector, part of the aerodynamic circulatory terms that multiply $\dot{\mathbf{u}}$ (p.51, 129)
$\mathbf{u}$	-	$n_{\text{dof}} \times 1$ vector with degrees of freedom (displacements and rotations) (p.46, 49)
$\mathbf{u}_{a,1}$, ..., $\mathbf{u}_{a,n_{\text{lag}}}$	-	$n_{\text{dof}} \times 1$ vector with aerodynamic states (p.52)

$\mathbf{u}_\phi$ - $n_{\text{dof}} \times 1$ vector with degrees of freedom in generalized coordinates (contains generalized displacements) (p.61)

$\mathbf{u}_\psi$ - $n_{\text{dof}} \times 1$ vector with degrees of freedom written in the MGCS (p.62)

$\mathbf{v}$ - $N \times 1$ vector of zeros with 1 at the k-th row (Eq. 13)

$\mathbf{w}_l$ - $n_{\text{dof}} \times 1$ vector of zeros with 1 at the l-th row (Eq. 14)

$\mathbf{x}$ - $N \times 1$ vector with states of the system (p.52)

$\mathbf{x}_i$ - the vector $\mathbf{x}$ at $t = t_i$ (p.58)

$\mathbf{x}_i^0$ - the vector $\mathbf{x}$ at $t = 0$ (initial condition) for the time simulation when $V = V_i$ (p.73)

$\mathbf{x}_i^{end}$ - the vector $\mathbf{x}$ at the last time when the LCO is detected for the time simulation when $V = V_i$ (p.73)

$\mathbf{x}^{sp}$ - the vector $\mathbf{x}$ at the switching point (p.59)

$\mathbf{x}_\phi$ - $N \times 1$ vector with the generalized states (p.61)

$\tilde{\mathbf{x}}$ - the $N \times 1$ modified state vector that contains time at the k-th row (p.59)

$\tilde{\mathbf{x}}_i$ - the vector $\tilde{\mathbf{x}}$ at $t = t_i$ (p.59)

$\tilde{\mathbf{x}}^{sp}$ - the vector $\tilde{\mathbf{x}}$ at the switching point (p.59)

$\mathbf{y}$ - $N \times 1$ vector with the dependent variables of a generic dynamic system (p.57)

$\mathbf{y}_i$ - the vector $\mathbf{y}$ at $v = v_i$ (p.57)

$\mathbf{z}$ - vector with the unknown non-dimensional amplitudes of the assumed harmonics for $\hat{u}_l$. When first and third are considered, it is a 2×1 vector (p.83)

$\mathbf{z}_j$ - converged vector $\mathbf{z}$ for $p = p_j$ (p.84)

$\mathbf{z}_{j,k}$ - vector $\mathbf{z}$ for the k-th iteration during Newton-Raphson convergence procedure when $p = p_j$ (p.84)

$\delta\mathbf{z}$ - increment of $\mathbf{z}$ for each Newton-Raphson iteration (Eq. 19)

$\mathbf{\Phi}_j$ - $n_{\text{dof}} \times 1$, the j-th vector of $\mathbf{\Phi}$ for $j = 1, ..., n_{\text{dof}}$, which is the j-th structural undamped mode (p.61)

Matrices

$\mathbf{A}$ - $N \times N$ aeroelastic dynamic matrix of the linear model (p.52, Eq. 22)

$\mathbf{A}_l$ - $N \times N$ aeroelastic dynamic matrix with $\mathbf{K}_l$ used instead of $\mathbf{K}$ to construct the matrix $\mathbf{A}$ of Eq. 22 (p.52)

$\bar{\mathbf{A}}$	-	$N \times N$ actual aeroelastic dynamic matrix of a particular sub-linear system from which eigenvalues are extracted (p.100, Tab. 4)
$\bar{\mathbf{A}}_l$	-	$N \times N$ actual aeroelastic dynamic matrix of a particular sub-linear system (outside or inside of freeplay) including the effect of freeplay on u_l (p.99)
$\hat{\mathbf{A}}$	-	$N \times N$ linear equivalent aeroelastic dynamic matrix (p.77, 127)
$\mathbf{C}_Q$	-	$n_{\text{dof}} \times n_{\text{dof}}(n_{\text{lag}} + 3)$ matrix of coefficients resulting from Roger's method (p.52)
$\mathbf{D}$	-	$n_{\text{dof}} \times n_{\text{dof}}$ structural damping matrix (p.49, 127, 128)
$\mathbf{D}_{nc}$	-	$n_{\text{dof}} \times n_{\text{dof}}$ non-circulatory aerodynamic damping matrix (p.51, 129)
$\mathbf{K}$	-	$n_{\text{dof}} \times n_{\text{dof}}$ structural stiffness matrix of the linear model (p.127, 128)
$\mathbf{K}_l$	-	$n_{\text{dof}} \times n_{\text{dof}}$ structural stiffness matrix modified with zero instead of k_{u_l} in the l-th row with l-th column (p.49, 127, 128)
$\mathbf{K}_{nc}$	-	$n_{\text{dof}} \times n_{\text{dof}}$ non-circulatory aerodynamic stiffness matrix (p.51, 129)
$\mathbf{M}$	-	$n_{\text{dof}} \times n_{\text{dof}}$ structural mass matrix (p.49, 127, 128)
$\mathbf{M}_{nc}$	-	$n_{\text{dof}} \times n_{\text{dof}}$ non-circulatory aerodynamic mass matrix (p.51, 129)
$\mathbf{Q}_0$, $\mathbf{Q}_1$, $\mathbf{Q}_2$	-	$n_{\text{dof}} \times n_{\text{dof}}$ matrices resulting from Roger's method. Coefficients multiplying $\mathbf{u}$, $\dot{\mathbf{u}}$ and $\ddot{\mathbf{u}}$, respectively (p.52)
$\mathbf{Q}_3$, ..., $\mathbf{Q}_{n_{\text{lag}}+2}$	-	$n_{\text{dof}} \times n_{\text{dof}}$ matrices resulting from Roger's method. Coefficients multiplying the extra states from aerodynamic lag (p.52)
$\mathbf{Q}_a(s)$	-	$n_{\text{dof}} \times n_{\text{dof}}$ matrix resulting from the original expression of for the aerodynamic efforts of Theodorsen written in frequency domain (p.51)
$\mathbf{Q}_{a,ap}(s)$	-	$n_{\text{dof}} \times n_{\text{dof}}$ matrix resulting from the approximated expression for the aerodynamic efforts after Roger's method applied, written in frequency domain (p.52)
$\mathbf{W}$	-	$N \times N$ matrix defined at Eq. 13
$\mathbf{\Phi}$	-	$n_{\text{dof}} \times n_{\text{dof}}$ matrix of undamped elastic modes (eigenvector matrix of $\mathbf{M}^{-1}\mathbf{K}$). It can be $n_{\text{dof}} \times n_{\text{tru}}$ if truncated with n_{tru} modes (p.61)
$\mathbf{\Psi}$	-	$n_{\text{dof}} \times n_{\text{tru}}$ matrix to perform transformation between the physical and modified generalized coordinate systems (p.61)
$\left.\dfrac{\partial \mathbf{F}}{\partial \mathbf{z}}\right\vert_{\mathbf{z}_{j,k},p_j}$	-	partial derivative of $\mathbf{F}$ with respect to $\mathbf{z}$ computed at $\mathbf{z} = \mathbf{z}_{j,k}$ and $p = p_j$, resulting in a 2×2 matrix (Eq. 19)

Theodorsen Model Symbols

Abbreviations

$m.s.$	-	middle section (p.48)
$e.c.^w$	-	elastic center of wing (p.48)
$e.c.^{CS}$	-	elastic center of CS (p.48)
$e.c.^t$	-	elastic center of tab (p.48)
$g.c.^w$	-	gravitational center of main wing only (p.48)
$g.c.^{CS}$	-	gravitational center of CS only (p.48)
$g.c.^t$	-	gravitational center of tab only (p.48)

Scalars

m_w	-	mass of main wing only, per unit span (p.127)
m_{CS}	-	mass of CS only, per unit span (p.127)
m_t	-	mass of tab only, per unit span (p.127)
m	-	total mass per unit span (p.127)
h, α, β, γ	-	plunge (vertical displacement), pitch, CS rotation, tab rotation, respectively (p.48)
b, s_p	-	semi-chord and span, respectively, of the airfoil (p.48)
a, c, d	-	distances w.r.t b to indicate where the elastic centers are located from $m.s.$ (p.48). See Tab. 1 for a detailed description
g_w, g_{CS}, g_t	-	distances to indicate where the gravitational centers of each part separately are located from each respective elastic center (p.48,127)
I_w, I_{CS}, I_t	-	individual inertia moments of mass of each part around its own gravitational center, per unit span (p.127)
I_α, I_β, I_γ	-	total inertia moments of mass, per unit span (p.50). See Tab. 1 for a detailed description
S_α, S_β, S_γ	-	total static moments of mass, per unit span (p.50). See Tab. 1 for a detailed description
k_h, k_α, k_β, k_γ	-	stiffness of each degree of freedom, per unit span (p.50). See Tab. 1 for a detailed description
x_α, x_β, x_γ	-	non-dimensional parameters such that $x_i = S_i/(mb)$ (p.132)
r_α, r_β, r_γ	-	non-dimensional parameters such that $r_i^2 = I_i/(mb^2)$ (p.132)

$\bar{h}$	-	non-dimensional plunge h/b (p.132)
T_i	-	constants of Theodorsen to reduce the expressions in aerodynamic matrices that captures the effect of the main control surface (depend on c) and its interaction with the main wing (p.130)
T_i^d	-	constants of Theodorsen to reduce the expressions in aerodynamic matrices that captures the effect of the tab (depend on d) and its interaction with the main wing (p.130)
Y_i	-	constants of Theodorsen to reduce the expressions in aerodynamic matrices that captures the combined effect of the main control surface and the tab (depend on c and d) (p.130)
s_c	-	defined herein as $\sqrt{1-c^2}$ (p.130)
s_d	-	defined herein as $\sqrt{1-d^2}$ (p.131)
o_c	-	defined herein as $\arccos(c)$ (p.130)
o_d	-	defined herein as $\arccos(d)$ (p.131)

Contents

1 Introduction

This thesis states the following sentence: "*Alternative approaches for predicting limit cycle oscillations induced by control surface freeplay are important to the field of nonlinear aeroelasticity and can contribute to understand the physics associated to this nonlinearity.*" To prove it, this chapter presents the general context of the work, its objectives as well as the actual reached contributions, including the associated publications. Also, a detailed literature review is presented as the basis for all other chapters, whose content description is included in the last section of this chapter.

1.1 The Context of the Work

Aeroelasticity is the science studying the interaction of elastic, inertial and aerodynamic forces. Different phenomena can be well modeled considering only elastic and inertial forces, which combined compose the structural vibrations field. However, in the aerospace industry, for example, it is impossible to neglect the effect of the flow in which the aircraft is immersed, since it generates considerable forces acting on the structure. A typical analysis of linear aeroelasticity is the flutter analysis, where the system stability is evaluated for each particular flight condition, and the interactions between aerodynamic and structural forces can lead to divergent motion that can be fatal.

Another important topic to be considered in nature is the nonlinear dynamics. Indeed, several fields of nature as biological, chemical, and other physical applications present nonlinear behavior that can not be accurately predicted with linear mathematical models. Then, aeroelastic systems can also involve nonlinear dynamics and a typical behavior is the emergence of limit cycle oscillations (LCOs) that, in practice, are self sustained oscillations limited at some amplitude with certain frequency which can be detrimental for the structure mainly in terms of fatigue. Furthermore, according to Dowell, Edwards and Strganac (2003), often a single nonlinear mechanism is primarily responsible for the LCO. Among several sources of nonlinearities, this work is focused on the LCO generated by geometric freeplay, typically present in hinge connections, such as the one that connects the control surface to the wing. In this sense, this work is part of the nonlinear aeroelasticity.

In addition to the harmful effects of the LCOs, such as fatigue issues or influence on the system controllability, the importance of predicting them is reassured by the aeronautical standards for certifying an aircraft. Airworthiness regulations - such as MIL-A-8870C, by United States Military Standard; AC 23.629-1B and AC 25.629-1B by Federal Aviation Administration (FAA) - establish maximum limits of freeplay allowed in the hinges. Then, lubrication and measurement cycles are required during the lifetime of the aircraft, and these procedures imply additional maintenance costs. Therefore, the nonlinear aeroelastic analysis to predict LCO may be a useful and valuable tool for reducing maintenance costs and improve the aircraft certification process (DOWELL; EDWARDS; STRGANAC, 2003).

The limit cycle oscillations prediction in aeroelasticity includes determining the flight conditions in which the phenomenon occurs, i.e, the pair of air density and airspeed. In practice, the engineer needs to determine the amplitude and frequency of motion, and time domain analysis involves performing time marching methods for each flight condition, including a time long enough to ensure that the LCO is fully reached. On the other hand, regarding the frequency domain methods, the classic flutter analysis for linear systems basically consists in extracting the eigenvalues of the aeroelastic dynamic matrix and the presence of a single eigenvalue with real positive part indicates an unstable system with divergent response. If all eigenvalues have negative real part, the system is stable and the response decays. The smallest flight condition for which an eigenvalue has null real part is called flutter condition, and it indicates the maximum limit of the flight envelope for the aircraft. This approach can be adapted for nonlinear systems, involving a linear equivalent system related to the LCO amplitude, and the eigenvalue analysis can be performed as described herein. In this case, the conditions with eigenvalues having null real parts are indicative of possible LCO.

If discontinuous nonlinearities are considered, the LCO prediction includes additional challenges in both time and frequency domains. Note that the freeplay in the control surface hinge is an angle gap with zero stiffness, which assumes a nominal value outside of the gap. Regarding the time domain, the position of the control surface must be known to integrate the correct corresponding equation in each time iteration. In this sense, this work applies the Hénon's technique to properly identify the switching times when the system changes zones (outside to inside of freeplay and vice-versa). Then, the novelty introduced in this work is a general formulation in matrix form to have an event detector. This new approach addresses two different issues, i.e., a numerical detector to capture inversion points in integration processes and the inclusion of discontinuous nonlinearities. Herein, it is applied for combined freeplay and friction, as well as for freeplay in more than one degree of freedom (DOF). Regarding the frequency domain, the solution including discontinuity demands a linear equivalent dynamic matrix to perform the eigenvalue analysis. This work employs the Equivalent Linearization Technique combined with Describing Functions. The main novelty introduced in this present work includes a new way of looking to the linearization problem, involving a new describing function to consider freeplay and friction effects and another one including information about the third harmonic of motion.

In this context, this work is aimed to improve existing methods to predict LCO arising from freeplay in control surfaces. An interesting application of the general Hénon technique formulation is included to study an aeroelastic system with freeplay in two hinges simultaneously. Although required by the airworthiness regulation, considering multiple freeplay is still a quite recent topic in nonlinear aeroelasticity, highlighting the importance of this study. This thesis also presents numerical results with bifurcation diagrams showing the influence of freeplay and friction on the aeroelastic responses. The findings contribute to establish new process to develop safer aircraft.

1.2 Objectives

The general objective of this research is to contribute to the nonlinear aeroelasticity by developing new features to numerical methods to improve the limit cycle oscillations prediction due to freeplay in control surfaces. Specific objectives are summarized below:

- develop a general methodology and computational algorithm of the Hénon's technique to consider multiple discontinuous nonlinearities in arbitrary degree of freedom;
- develop new describing functions to consider freeplay and Coulomb friction simultaneously in control surface;
- investigate the use of describing functions for LCO presenting the first and third harmonics;
- construct bifurcation diagrams to understand the physical effects considering both fricton and freeplay as well as freeplay acting on two different hinges;

1.3 Literature Overview

Real dynamic systems often may be nonlinear Hartog (1985). In the aeroelasticity context, nonlinearities have their first mentions around 1950s, when Woolston, Ruyan and Byrdsong (1955), Woolston, Ruyan and Andrews (1957) explain that they can appear in each of the three force types (inertia, damping and elastic) arising either from aerodynamic or structural sources. Aerodynamic sources include, for instance, shock in transonic flow; flow separation (the most common in transonic flow); viscous effect; dynamic stalls. Besides, Breitbach (1978) suggests that structural sources are separated in distributed and concentrated nonlinearities. The first type of nonlinearity acts on the whole structure by elasto dynamic deformations and it can appear in components of the main structure itself. It can also be observed in connections with bolts, screws or rivets, since these usually small elements appear in a huge amount distributed in a relatively continuous way throughout the structure - and the resulting damping and stiffness are considered distributed nonlinearities. On the other hand, the concentrated nonlinearities act locally specially on control mechanisms or connecting parts between wing and external stores or pylon, pylon and engine, and others.

A typical classification of nonlinearities refers to the mathematical expressions used to represent their behavior, and they can be divided in continuous and discontinuous nonlinearities. In terms of dynamics, representing the force with the presence of a discontinuous nonlinearity includes a sudden change at particular displacements, velocities or accelerations, and they can be called switching points. A common continuous nonlinearity is the cubic stiffness, either hard or soft and, although it can appear as concentrated nonlinearity, it often appears as distributed nonlinearities in bolts, screws and rivets. On the other hand, the most common concentrated structural nonlinearities are also discontinuous, such as freeplay (without and with preload), bilinear stiffness, hysteresis, solid friction, and others (WOOLSTON; RUYAN; ANDREWS, 1957; BREITBACH, 1978; LEE; PRICE; WONG, 1999; DOWELL; TANG, 2002). The present work focuses on structural nonlinearities concentrated in a control surface hinge, specially freeplay and solid friction.

Freeplay

Freeplay is a kind of backlash - or gap - that appears on rotation of control surface hinge (BREITBACH, 1978; BLOCK; STRGANAC, 1998). It makes the stiffness to change discontinuously with the control surface rotation angle (the stiffness inside the freeplay zone is zero). Symmetric freeplay means that the center of freeplay is coincident to the zero hinge line (null control surface rotation). However, Arévalo (2008) comments that symmetric freeplay does not represent all possible real configurations, and a few number of authors consider the presence of asymmetry. A typical source of asymmetry considered by different authors is a preload, which means that the system equilibrium point is displaced from the center of freeplay and it is no longer located in the zero stiffness zone, on the contrary, it is in linear zone (CHEN; LEE; LIU, 2006; ANDERSON; MORTARA, 2007; KHOLODAR; DICKINSON, 2010). This preload can arise from aerodynamic loads (variate with flow speed), when the hinge line where the freeplay acts is not aligned with flow direction, mainly due to a change in the angle of attack, for instance (KHOLODAR, 2014), or from mechanical loads (do not variate with flow speed), such as the influence of structure weight (YANG; ZHAO, 1988). Another type of asymmetry mentioned by Lee, Price and Wong (1999) refers to the asymmetrical freeplay without preload (the equilibrium is also displaced from the freeplay center, but now is in the zero stiffness zone). This latter is included in the studies of the present work.

A typical effect caused by freeplay is the limit cycle oscillations, as already mentioned by Woolston, Ruyan and Andrews (1957), and they have been observed in operational aircraft as well in wind-tunnel. LCO is a typical behavior associated to nonlinear systems and, if it is stable, the limit cycle is a periodic trajectory that attracts other trajectories in its neighborhood. Thus, regardless of the initial condition, as long as it belongs to this defined neighborhood of influence, the steady motion ends up reaching the LCO.

When occurring at airspeeds above the flutter condition (supercritical bifurcation), despite damages in structural integrity due to fatigue when the amplitudes are too large, the LCO may introduce a good effect because it attenuates the exponentially growing oscillations that occur in an unstable linear system (DOWELL; TANG, 2002). However, aeroelastic system can exhibit a well known subcritical bifurcation, where LCOs occur at airspeeds below the flutter condition, and therefore, the system stability changes and fatigue is again an issue that needs attention. The relevance of this topic is also highlighted in the US FAA memorandum, that explicitly requires including the freeplay in stability analysis (SCHNEIDER; MARTIN, 2007). Then, an important task for aeronautical engineers is to predict the flight conditions (velocity and air density) in which this oscillatory phenomenon takes place, including its amplitude and frequency.

Due to poor agreement observed between the first theories and experimental flutter tests being attributed to nonlinear structural stiffness (BREITBACH, 1978), several researchers have investigated the effect of freeplay, in both theoretical and experimental point of view. The most common experimented systems include a typical airfoil section; a delta wing with store; and all-movable horizontal tail, and Tang and Dowell (2011) is a great reference for noting that. However, the challenges of nonlinear aeroelasticity include the development of efficient and accurate numerical methods and analytical approaches, mainly to solve ordinary differential equations (ODEs) employed to model the aeroelastic systems and, then, apply them to predict LCOs during the aircraft development process.

Methods to Solve Systems with Freeplay

Several methods can be found in the literature, such as the numerical methods for time integration, the frequency domain-based methods, analytical methods and even iterative methods which allow one to predict the system dynamics if a certain physical or geometric parameter is varied. Then, a commented description for most of them, including their pros and cons, can be found in a review article published as part of this work contributions (BUENO; WAYHS-LOPES; DOWELL, 2022). These information help choosing the most suitable method, which depends on the analyst's objective. In addition, a brief description of the main works including experimental tests performed to demonstrate different of those methods is included below.

- **Experimental tests focused on demonstrating the methods**

Different methods have been demonstrated by considering the 2-DOF airfoil, including results from an analog computer described by Woolston, Ruyan and Byrdsong (1955), Woolston, Ruyan and Andrews (1957), from Describing Functions (DF) by Yang and Zhao (1988), from the Normal Form method by Abdelkefi *et al.* (2012) and also considering buffeting flow with the angle of attack effect by Tang and Dowell (2013). For the 3-DOF system with freeplay acting on the control surface degree of freedom, experimental tests are compared with theoretical results obtained from Hénon's technique by Conner *et al.* (1997), Trickey, Virgin and Dowell (2002), from DF with continuation parameter by Gordon, Meyer and Minogue (2008), considering gust effect by Tang, Kholodar and Dowell (2000), Lee *et al.* (April 2010); whereas Verstraelen *et al.* (2017) consider a 3-DOF typical section with freeplay acting on the pitch DOF. In addition, Al-Mashhadani *et al.* (2017) carry out experimental tests for a 4-DOF typical section with control surface and tab. These works also confirm the importance of including freeplay in aeroelasticity.

- **Time domain-based methods**

The classical numerical integration methods in the time domain, such as the Runge-Kutta methods, are known for their relatively simple computational implementation and for allowing to find solutions for different problems, including behavior such as decay, LCO, quasi-periodic and even chaotic transient motion. These are clear advantages when it comes to continuous nonlinearities. However, for discontinuous nonlinearities such as freeplay, Conner, Virgin and Dowell (1996) show that the discontinuity produces numerical errors if classic time marching methods are employed. Therefore, improved approaches are required to successfully find the solution via this type of method.

Reduced errors can be achieved either using a continuous function to approximate the discontinuous nonlinearity before executing the classical method (VASCONCELLOS *et al.*, 2012); or applying a switching point search technique (for instance, Hénon's technique) to integrate the correct equation (suitable for the region) in each time iteration. The first strategy requires prior knowledge of the continuous function or a thorough search for it, whereas the second can be implemented in a more general way. This work considers the latter strategy by particularly employing the Hénon's technique, which basically perform an iteration with a different independent variable (spatial instead of time) to properly locate the switching points. Dai *et al.* (2015) compares this technique with the conventional Runge-Kutta algorithm to predict chaotic behavior. Additionally, since this technique has been demonstrated by experimental tests such as Conner *et al.* (1997), Trickey, Virgin and Dowell (2002), Vasconcellos *et al.* (2012), it has been considered by several authors as a reference approach to support the results from other methods or to explore the freeplay effects, as described by Vasconcellos *et al.* (2014), He, Yang and Gu (2017), He *et al.* (2020). The method is also used to evaluate the performance of controllers designed to suppress LCO (LI; GUO; XIANG, 2010; BUENO; GÓES; GONÇALVES, 2014).

Still regarding time domain methods, when dealing with discontinuous nonlinearities and specially for those that are piecewise linear, an alternative approach considers the classical analytical solutions for a matrix-based linear ODE involving the matrix exponential notation. In this type of solution, the time integration for methods such as the Precise Integration Method (TIAN; YANG; GU, 2017) takes place analogously to classical numerical integration methods, but using the analytical solution and relying on a thorough search of the switching point via predictor-correction algorithm. Another method is the Point Transformation Method (LIU; WONG; LEE, 2002), for which the traveling time to the switching points can be computed with the analytical solution, allowing the use of larger time steps. The analytical solutions tend to have more precise answers than the numerical, but typically they are known for a limited number of practical problems.

Despite the disadvantage of computational costs to integrate a whole time range for each parameter when looking for bifurcation diagrams, time domain-based methods have been successfully employed to integrate the actual discontinuous nonlinear system and, in the absence of experimental results for comparison, they are welcome methods to be used as reference to evaluate the accuracy of other numerical methods. In this context, the present work improves the Runge-Kutta classic method with the Hénon technique. This technique has not been found in a detailed and practical way in literature, and a contribution of this work is providing a general formulation to easily implement the technique for any arbitrary discontinuous nonlinearity, including when more than one are considered simultaneously acting on the system.

- **Iterative and Local Analytical methods**

The construction of bifurcation diagrams can be achieved employing iterative methods such as Numerical Continuation (DIMITRIADIS, 2008a) and Perturbation Incremental Method (CHUNG; CHAN; LEE, 2007). Their goal it to characterize the aeroelastic system response according to a particular system parameter and they allow one to avoid integration over the entire time interval for each evaluated parameter. In practice, once a steady state solution is known for a certain parameter value, it is possible to search for the new solution incrementally by varying this parameter value in some amount, which decreases the execution time when compared to classic temporal integration. On the other hand, local analytical methods such as the Normal Form (VIO; COOPER, 2005) and Center Manifold (LIU; WONG; LEE, 2000) avoid using not only time integration but also iterative processes, which is a great advantage in terms of computational time. However, they are based on reducing the dimension of the system to its normal form to remove the less significant nonlinear parts, and then, they require to previously know the corresponding normal form, that is, they require prior calculations that are specific for each particular system. In addition, its higher accuracy is limited to the neighborhood of a critical point.

- **Frequency domain-based methods**

The computational time associated to a time domain-based solution can be reduced by using frequency domain methods. The Harmonic Balance-based (HB) methods usually assume a harmonic motion for LCO of the nonlinear DOF and approximate the nonlinear force (continuous or discontinuous) by periodic expressions via Fourier series. There are different versions based on this idea, such as for an example, Breitbach (1980) considers the LCO with a single harmonic, whereas Dimitriadis (2008b) presents a synthesis comparing similarities and differences among several variations of the HB. The approaches consider high order harmonics in the Fourier series (High Order Harmonic Balance - HOHB) (LIU; DOWELL, 2005) or, alternatively, change the problem to the time domain via the Fourier Transform (High Dimensional Harmonic Balance or Time Domain Collocation) (LIU; DOWELL; THOMAS, 2005; DAI *et al.*, 2014).

There are basically two approaches to deal with the harmonic expressions approximating the force and motion. In the first one, usually employed in the HOHB methods, these harmonic expressions are replaced directly into the equation of motion and, an algebraic system of equations with multiple variables is defined by performing the harmonic balance between the two sides of the resulting equation (LIU; DOWELL, 2005). On the other hand, in the second approach, the harmonic balance does not involve the equation of motion itself and it is performed between the force and an assumed motion, defining an equivalent linear term (describing function). Particularly for freeplay, a linear equivalent stiffness is defined and it is related to the freeplay boundary and the LCO amplitude. Therefore, if the Equivalent Linearization Technique (ELT) made possible through the Describing Function is used, the second approach accounts to the advantage of using the classical linear stability analysis, avoiding the need for time integration process for each flight condition. In addition, it can be employed to identify multiple LCOs for each flight condition without substantially increasing the computational cost (BUENO; WAYHS-LOPES; DOWELL, 2022).

This second approach introduced above combines the describing function with the classic linear stability analysis, and it is roughly referred in literature as simply Describing Function Method, particularly when considering a single harmonic. It is used in several works to predict LCO accurately (SHEN, 1959; YANG; ZHAO, 1988; PRICE; ALIGHANBARI; LEE, 1995; TANG; DOWELL; VIRGIN, 1998; ANDERSON; MORTARA, 2007; KHOLODAR; DICKINSON, 2010; ZHANG; WU, 2015; YANG; HE; GU, 2016; HE; YANG; GU, 2017; PADMANABHAN; DOWELL, 2017; VERSTRAELEN *et al.*, 2017). Although the formulation considered by them includes the first harmonic information only, Tamura, Tsuda and Sueoka (1981) assures that the prediction of the third harmonic can be important to improve the accuracy of the HB-based method. Comparing these both described approaches, a HOHB method usually involves more complex algebraic manipulations and requires a non trivial solution of a high order system of nonlinear equations. On the other hand, the DF method comes to simplify the LCO prediction since the equivalent linear stiffness is related to the amplitude of motion by a simple scalar mathematical equation, but it is also related to the airspeed and frequency via the linear stability analysis. In this sense, the advantage of the DF method is clearly related to the reduced computational time, since it uses the eigenvalue-based solution, as typically employed during the stability analysis in an aircraft development cycle. Despite it is restricted to identify periodic solutions, this approach is employed in this present work, since its main interest is the periodic LCO prediction. Then, this thesis introduces a new approach by adapting the well known DF method to predict the first and third harmonics in limit cycle oscillations.

Combined Nonlinearities

The significance of accounting for multiple nonlinearities has been acknowledged since the earliest documents discussing sources of concentrated nonlinearities in aeroelastic systems, which already suggest the potential of considering them combined. (WOOLSTON; RUYAN; ANDREWS, 1957; BREITBACH, 1980). Although important, considering combined nonlinearities usually includes additional computational costs, and because of that, only a few works were found at that time. Laurenson and Trn (1980) consider freeplay in both the roll and pitch degrees of freedom of the root support stiffness of a missile control surface. Their results indicate a different influence of freeplay in each degree of freedom, and the tolerance for the pitch degree of freedom is more critical than the roll degree of freedom to achieve a successful design. Additionally, Lee (1986) considers bilinear stiffness in both the plunge and pitch degrees of freedom, and the results show that the stability boundary of a system with multiple nonlinearities does not necessarily fall between the boundaries predicted by a linear flutter analysis.

Indeed, the past twenty-five years have proven crucial in the development of enhanced numerical methods suitable for systems with concentrated nonlinearities. These advancements have been spurred by the remarkable progress in new technologies and the wider availability and popularity of more powerful computational tools. The scenario contributes to consider more than a single nonlinearity when addressing an aeroelastic problem. In this sense, works involving combined nonlinearities are becoming more common in recent years. For example, Padmanabhan, Dowell and Pasiliao (2018), Silva and Marques (2022) consider different structural nonlinearities such as cubic stiffness, freeplay and friction. Similarly, Vishal *et al.* (2022), Vishal *et al.* (2021) investigate the combination of freeplay with aerodynamic nonlinearities induced by dynamic stall. In this context, this thesis also focuses on considering combined discontinuous nonlinearities such as freeplay and friction acting on a single DOF, as well as considering more than one DOF with freeplay.

- **Freeplay and Coulomb Friction**

Coulomb friction is also a discontinuous structural nonlinearity, involving a constant friction force considered in a direction that changes according to the sign of the DOF velocity. Also called solid friction, it often arises from sliding contact of structural components (DOWELL; TANG, 2002). Breitbach (1978) highlights that theoretical results present a best match with data measured on real aircraft structures when both effects are simultaneously considered on the numerical analysis. Indeed, friction and freeplay are common in control surfaces, specially in hinge bearings between actuator and structure (BREITBACH, 1978) as well as between wing and external store (TANG; DOWELL, 2006).

Although its importance is conceptually recognized, there are not considerable number of works that consider friction (in comparison with freeplay) in aeroelasticity, and even less considering both freeplay and friction acting simultaneously on control surfaces. Silva and Marques (2022) present a parametric analysis combining different concentrated nonlinearities, including freeplay and friction, revealing bifurcation diagrams using time domain simulations. Eller (2007) considers friction and freeplay acting on a control surface coupled in a typical 3-DOF airfoil and notes that the effect of these friction forces is more important in small airplanes since they are often equipped with manually operated control system. Padmanabhan, Dowell and Pasiliao (2018) consider multiple nonlinearities including freeplay and friction in two different systems, an aircraft wing carrying a store and all-moving surface.

Hartog (1931) and Yeh (1966) introduced the first exact solutions to the equation of motion considering the friction force acting on systems with one and two degree-of-freedom. However, because of Coulomb friction is also a discontinuous nonlinearity, Awrejcewicz and Olejnik (2002) note that it also requires a careful process for numerical integration of the equations of motion. The authors employ the Hénon's technique to study a self-excited mechanical system with different types of friction, and demonstrate that their method provides reliable and computationally efficient results. In this sense, a contribution of the present research is a detailed formulation and a practical description of how to use the Hénon's technique for systems with both freeplay and friction (WAYHS-LOPES; DOWELL; BUENO, 2020).

Regarding frequency domain-based methods to solve systems in such configuration, Eller (2007) and Padmanabhan, Dowell and Pasiliao (2018) present describing functions to consider both freeplay and friction. However, their articles do not provide practical detailed procedure for the LCO prediction using these expressions. Thus, another contribution of this work is to propose a practical procedure to employ the classical eigenvalue analysis combined with a describing function to predict LCO in systems with both freeplay and friction (WAYHS-LOPES; DOWELL; BUENO, 2023).

- **Freeplay in Multiple DOFs**

The LCO typically generated by freeplay can be detrimental to the structure in terms of fatigue and change the system's controllability. Because of these effects, the airworthiness regulations (MIL-A-8870C, by United States Military Standard; AC 23.629-1B and AC 25.629-1B by Federal Aviation Administration) that establish maximum limits of freeplay allowed in the hinges also highlight the need of considering the freeplay not only in the main control surfaces but also in the corresponding tabs. Although the literature review for aeroelastic systems with freeplay in a single control surface provides several interesting works, only two recent studies are found to examine freeplay in multiple degrees of freedom. Yu, Damodaran and Khoo (2022) consider freeplay in both leading and trailing-edge control surfaces of a two dimensional airfoil. Although a similar system is studied by Al-Mashhadani *et al.* (2017) with the difference that the fourth DOF is a tab attached to the trailing edge of the control surface, these authors consider freeplay on the tab only. Finally, Bai, Wu and Yang (2023) perform an interesting detailed study of a all-movable fin with freeplay in both bending and torsional degrees of freedom. Then, this research also investigates the 4-DOF airfoil with freeplay in both main trailing edge control surface and an attached tab. The results show the main differences in comparison with the single freeplay case.

1.4 Contributions

This research provides incremental improvements to existing numerical methods in both time and frequency domains typically used to predict limit cycle oscillations induced by freeplay in a control surface hinge. The improvements are accomplished by adapting the methods to consider combined discontinuous nonlinearities such as freeplay and friction, as well as multiple DOFs with freeplay. Therefore, this research is a definite contribution to the field of nonlinear aeroelasticity and a list of publications in specialized journals as well as the articles resulting from attended conferences is presented at the end of this section. Finally, each contribution bellow is linked to a particular publication.

Specific Contributions

a. a general formulation including an simple matrix form developed to express the Hénon's Technique suitable for any arbitrary type or number of discontinuous nonlinearities (Article I.a);

b. the Hénon's Technique proposed to be also an event locator, such as local extremes of a time domain solution (Article I.a);

c. a discussion on the effect when considering asymmetric freeplay and friction acting on a single degree of freedom (Article I.a);

d. a new way of looking to the Equivalent Linearization Technique to predict LCO, combining describing functions (to associate the linear equivalent system to the LCO amplitude) with the linear eigenvalue analysis (Article I.b);

e. a new Describing Function to consider the dynamics of the third harmonic in systems with freeplay (Article I.b);

f. a new Describing Function to consider Coulomb friction as force proportional to velocity if freeplay is included (Article I.b);

g. an iterative-ELT procedure to predict the first harmonic of LCO in systems with friction and freeplay acting simultaneously on the control surface (Article I.b);

h. an airfoil with freeplay in two different control surfaces, including bifurcation diagrams and Poincarè sections showing LCO and quasi-periodic motions (Conference II.c);

i. a literature review on the numerical methods employed to solve aeroelastic nonlinear systems with freeplay (Article I.c).

Publications

I. *Publications in Journals*

- I.a - Wayhs-Lopes, L. D., Dowell, E. H. & Bueno, D. D. (2020), 'Infuence of friction and asymmetric freeplay on the limit cycle oscillation in aeroelastic system: An extended Hénon's technique to temporal integration', Journal of Fluids and Structures 96, 103054. **URL**: https://doi.org/10.1016/j.jfluidstructs.2020.103054. The main content refers to the chapter 3. (WAYHS-LOPES; DOWELL; BUENO, 2020)
- I.b - Wayhs-Lopes, L. D., Dowell, E.H. & Bueno, D. D. (2023), 'A new look at the Equivalent Linearization Technique to predict LCO in aeroelastic systems with discrete nonlinearities'. Journal of Fluids and Structures 119, 103867. **URL**: https://doi.org/10.1016/j.jfluidstructs.2023.103867. The content of this paper is included in chapter 4. (WAYHS-LOPES; DOWELL; BUENO, 2023)
- I.c - Bueno, D. D., Wayhs-Lopes, L. D. & Dowell, E. H. (2022), 'Control-surface structural nonlinearities in aeroelasticity: A state of the art review', AIAA Journal 60(6), 3364–3376. **URL**: https://arc.aiaa.org/doi/10.2514/1.J060714. Part of the content is included in the Literature Review in section 1.3. (BUENO; WAYHS-LOPES; DOWELL, 2022)

II. *Publications in Conferences*

- II.a - Wayhs-Lopes, L. D. & Bueno, D. D. (2021) 'Iterative Method to predict limit cycles in aeroelastic systems with freeplay and Coulomb friction via Describing Functions', 26th International Congress of Mechanical Engineering (COBEM). **URL**: https://doi.org/10.26678/ABCM.COBEM2021.COB2021-2326
- II.b - Wayhs-Lopes, L. D., Dowell, E. H., Cesnik, C. E. S. & Bueno, D. D. (2021) 'An adapted equivalent linearization to predict higher harmonics of LCO in aeroelastic system with freeplay', Online Symposium on Aeroelasticity, Fluid-Structure Interaction, and Vibrations. **URL**: https://www.aeroelasticity2021.com
- II.c - Wayhs-Lopes, L. D., Bueno, D. D. & Cesnik, C. E. S: "Aeroelastic limit cycle oscillations due to multi-element control surface with freeplay", Third International Nonlinear Dynamics Conference (NODYCON 2023). **URL**: https://www.springer.com/journal/11071/updates/17947870. The content is included in chapter 5 and the full paper is with the publication department of the conference to be published soon.

1.5 Work Organization

The general context of this research as well as the literature overview on the main topics involved are included in the present chapter. The main goals and also the accomplished contributions with the respective publications are also described herein. The content of the remaining chapters of this thesis is presented below.

- Chapter 2 presents the methodology for the aeroelastic systems used in this work (3-DOF and 4-DOF airfoil) including freeplay and friction formulation. It also includes particular configuration of physical and geometrical parameters of the airfoils employed;

- Chapter 3 presents the detailed formulation for Hénon's technique, suitable to use for any arbitrary discontinuous nonlinearity. A modified generalized coordinate system is defined to facilitate the use of Hénon's technique. As an application, the effect of friction and asymmetry freeplay in a 3-DOF airfoil is explored. At the end, this chapter also includes the procedure employed to properly identify the LCO in computational algorithms and also how using the Hénon's technique as a locator of local extremes of the time response. Finally, it describes how the bifurcation diagrams distributed in the chapters of this thesis are constructed by using time marching.

- Chapter 4 concerns frequency domain methods, based on Harmonic Balance. A new way of looking to the Equivalent Linearization Technique to predict LCO is introduced, combining describing functions (to associate the linear equivalent system to the LCO amplitude) with the linear eigenvalue analysis (to associate the linear equivalent system to the LCO flight condition and frequency). Two applications are presented: a new DF is proposed to consider the first and third harmonics in systems with freeplay; also, an iterative procedure to use a new describing function including friction and freeplay effects.

- Chapter 5 shows a detailed study of a 4-DOF airfoil with both hinges of trailing edge control surface and attached tab with freeplay. The Hénon's technique is used to perform time integration for both freeplays simultaneously and capture the resulting LCO. Bifurcation diagrams are constructed and the main differences observed when comparing this configuration with the single freeplay case are presented.

- Chapter 6 presents the final remarks of this work highlighting the main contributions and the final conclusions of this thesis.

2 Aeroelastic Dynamic Models

This chapter presents the mathematical models to represent the aeroelastic systems (airfoil based on Theodorsen (1935) formulation) used in this work as well as the considered discontinuous nonlinearities (freeplay and Coulomb friction). Two different aeroelastic models are studied: the three degree-of-freedom airfoil, where a trailing edge control surface (CS) is added to the pitch and plunge DOFs; and the four degree-of-freedom airfoil, where a tab is attached to the main control surface. Both of them consider the unsteady aerodynamics of Theodorsen (1935), which is based on the potential flow. This chapter shows the general ideas involved to obtain those models for both structural and aerodynamic efforts. The second order differential equation of motion in the presence of freeplay and friction is highlighted as well as the first order equation (state space notation). Details for the employed formulation are left in Appendix A. Finally, the end of this chapter shows particular parameters for different airfoil configurations employed in this work, which are properly referred in this document.

2.1 Discontinuous Nonlinearities

Discontinuous nonlinearities are called this way because, mathematically, its equation changes non-smoothly at some critical value. Freeplay nonlinearity is commonly present in hinge connections. The piecewise linear torque of a hinge with freeplay (gap of range $\delta_L^l + \delta_R^l$ in which the stiffness has no action) depends discontinuously on the hinge rotation angle, such that outside of the freeplay there is a linear torque while it is zero when inside of the gap. Considering a system with a displacement vector $\mathbf{u}$ with n_{dof} degrees of freedom (DOFs), the nonlinear restoring force f_l^δ acting on the l-th DOF subject to the freeplay nonlinearity is given by (HARTOG, 1931)

$$f_l^\delta(t) = \begin{cases} k_{u_l}\left[u_l(t) + \delta_L^l\right] & , \quad u_l < -\delta_L^l \\ 0 & , \quad -\delta_L^l < u_l < \delta_R^l \\ k_{u_l}\left[u_l(t) - \delta_R^l\right] & , \quad u_l > \delta_R^l \end{cases} \tag{1}$$

where the subscripts R and L refer to right and left hand sides, respectively, as illustrated in Fig. 1a. Asymmetric freeplay can be evaluated by considering $\delta_L^l \neq \delta_R^l$ whilst the symmetric case is defined by $\delta^l = \delta_R^l = \delta_L^l$ (note that both values δ_L^l and δ_R^l are positive, given in terms of their magnitude). Also, k_{u_l} is the nominal stiffness of u_l which acts linearly when outside of the freeplay.

The friction Coulomb, also appearing in hinge connections is modeled in such a way that presents a constant torque according to the sign of velocity $\dot{u}_l$ (see Fig. 1b.). An interesting effect is that, if considered in the same DOF of freeplay, there is no friction inside the freeplay, since there is no contact in the gap.

$$f_l^C(t) = \begin{cases} -C & , \quad \dot{u}_l < 0 \text{ and } (u_l < -\delta_L^l \text{ or } u_l > \delta_R^l) \\ 0 & , \quad -\delta_L^l < u_l < \delta_R^l \\ C & , \quad \dot{u}_l > 0 \text{ and } (u_l < -\delta_L^l \text{ or } u_l > \delta_R^l) \end{cases} \tag{2}$$

where C is the amplitude of the Coulomb friction torque, in Nm /m (because the equation of motion is written per unit span).

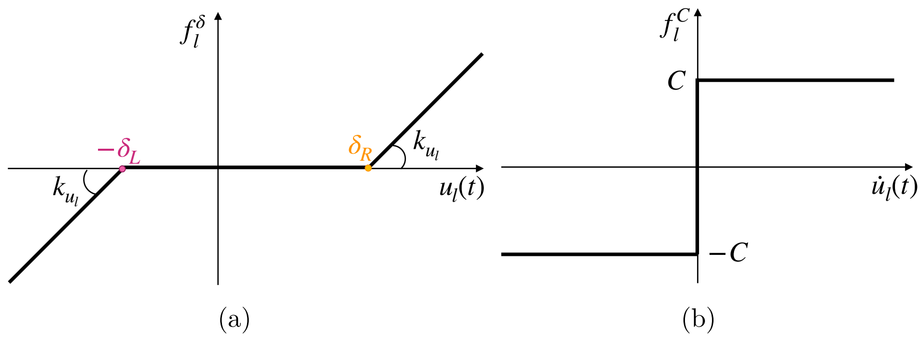

Figure 1 – Representation of nonlinearities effects: a) freeplay and b) Coulomb friction.

The dry friction model considered in this work is ideal and accounts for the slipping phase (kinetic friction) exclusively. In this model, when freeplay is present, it assumes that within the freeplay region, the control surface is disconnected from the mechanical components that transmit the friction torque, resulting in zero friction within the freeplay region (ELLER, 2007). However, a more practical friction model incorporates also the sticking phase, where viscous effects are considered, especially for small velocities $\dot{u}_l$, and the Stribeck curve may be employed (LEE; PRICE; WONG, 1999; LIU *et al.*, 2015). Alternatively, a different model can be used when friction forces are also considered inside the freeplay zone, allowing for the investigation of their effects on LCOs.

2.2 Aeroelastic Model: Second Order Equation

The original publication of the typical section of a wing - an airfoil - with control surface, as shown in Fig. 2, is found in Theodorsen (1935). In this work, the aeroelastic equations for the three degrees of freedom plunge (h), pitch (α) and the CS rotation (β) are provided. A few years latter, Theodorsen and Garrick (1942) extended the work by adding a fourth degree of freedom (γ), a tab attached to the main movable surface, as shown in Fig. 3. According to the authors, such configuration (WENZINGER, 1937) has direct application to the larger problem of flutter involving tail with control surfaces, including servo-controls, and this same model was also studied by Al-Mashhadani *et al.* (2017).

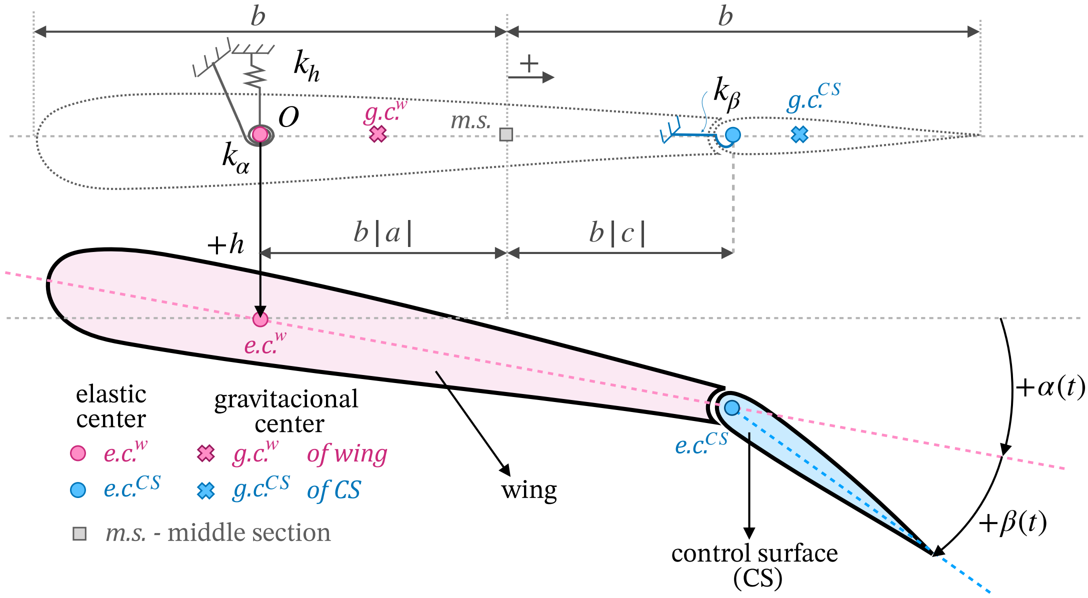

Figure 2 – 3 DOF airfoil with control surface. h is the vertical displacement plunge, α is the pitch angle of the system (wing-CS) around $e.c.^{w}$ and β is the rotation angle of control surface.

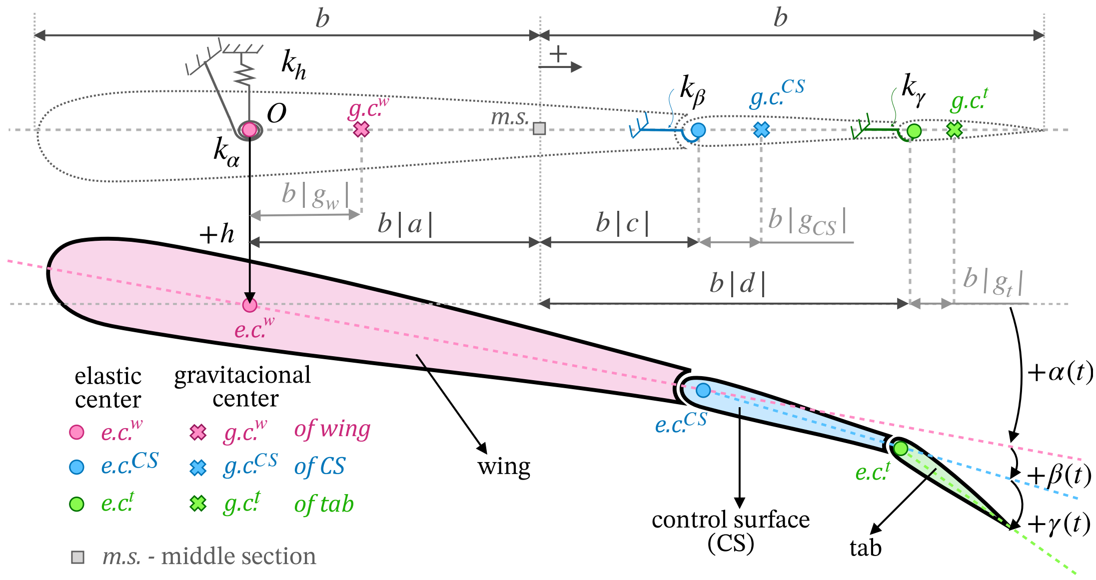

Figure 3 – 4 DOF airfoil with control surface. h is the vertical displacement plunge, α is the pitch angle of the system (wing-CS-tab) around $e.c.^w$; β is the rotation angle of CS-tab around $e.c.^{CS}$; and γ is the rotation angle of tab around $e.c.^t$.

The second order aeroelastic equation of motion for both systems (3-DOF or 4-DOF airfoil), including freeplay and friction in the l-th DOF is given by

$$\mathbf{M}\ddot{\mathbf{u}}(t) + \mathbf{D}\dot{\mathbf{u}}(t) + \mathbf{K}_l\mathbf{u}(t) + \sum_l \mathbf{f}_l^\delta(u_l, k_{u_l}, \delta^l) + \sum_l \mathbf{f}_l^C(\dot{u}_l, C) = \mathbf{F}_a(t) \tag{3}$$

where the displacement vector is $\mathbf{u} = \{h \quad \alpha \quad \beta\}^T$ and $\mathbf{u} = \{h \quad \alpha \quad \beta \quad \gamma\}^T$ for the 3-DOF and 4-DOF airfoil, respectively. $\mathbf{M}$, $\mathbf{D}$ and $\mathbf{K}_l$ are the $[n_{\text{dof}} \times n_{\text{dof}}]$ mass, damping and stiffness structural matrices (explicit in Appendix A). $\mathbf{F}_a(t)$ is the unsteady aerodynamics term (see section 2.2.2). The matrix $\mathbf{K}_l$ is modified to adapt the inclusion of freeplay in such a way that zero is used instead of the nominal stiffness k_{u_l} related to the l-th DOF. The vectors $\mathbf{f}_l^\delta$ and $\mathbf{f}_l^C$ are $n_{\text{dof}} \times 1$ vectors of zeros with, respectively, f_l^δ and f_l^C in their l-th row (see Eq. 1 and 2). The summation symbol is used to allow inclusion of these nonlinearities in multiple degrees of freedom.

2.2.1 Structural Dynamics

The left-hand side of the equations in Eq. (3) refers to the structural vibrations of the system, where elastic and inertial efforts are considered. To demonstrate the linear part (not including freeplay and friction forces), typical mechanics approaches as Newtonian or Lagrangian dynamics can be employed to obtain those equations, which are written in their scalar form omitting any aerodynamic terms for the three and 4-DOF airfoils, respectively, in Eq. (4) and (5). The main considerations to derive the structural dynamics include assuming the dimensional (physical) system; the elastic centers are not coincident with the gravitational centers and a linearization for small angles is performed (such that θ^2, $\dot{\theta}^2$ and $\ddot{\theta}^2$ are neglected, $\sin\theta \approx \theta$ and $\cos\theta \approx 1$).

$$
\begin{aligned}
& m\ddot{h} + S_\alpha\ddot{\alpha} + S_\beta\ddot{\beta} + k_h h = 0 \\
& S_\alpha\ddot{h} + I_\alpha\ddot{\alpha} + [I_\beta + b(c-a)S_\beta]\ddot{\beta} + k_\alpha\alpha = 0 \\
& S_\beta\ddot{h} + [I_\beta + b(c-a)S_\beta]\ddot{\alpha} + I_\beta\ddot{\beta} + k_\beta\beta = 0
\end{aligned} \tag{4}
$$

$$
\begin{aligned}
& m\ddot{h} + S_\alpha\ddot{\alpha} + S_\beta\ddot{\beta} + S_\gamma\ddot{\gamma} + k_h h = 0 \\
& S_\alpha\ddot{h} + I_\alpha\ddot{\alpha} + [I_\beta + b(c-a)S_\beta]\ddot{\beta} + [I_\gamma + b(d-a)S_\gamma]\ddot{\gamma} + k_\alpha\alpha = 0 \\
& S_\beta\ddot{h} + [I_\beta + b(c-a)S_\beta]\ddot{\alpha} + I_\beta\ddot{\beta} + [I_\gamma + b(d-c)S_\gamma]\ddot{\gamma} + k_\beta\beta = 0 \\
& S_\gamma\ddot{h} + [I_\gamma + b(d-a)S_\gamma]\ddot{\alpha} + [I_\gamma + b(d-c)S_\gamma]\ddot{\beta} + I_\gamma\ddot{\gamma} + k_\gamma\gamma = 0
\end{aligned} \tag{5}
$$

Geometric Parameters: in the representation of the figure, b is the aerodynamic semi-chord. a, c and d are non-dimensional with respect to b and indicate, respectively, the position of the elastic center ($e.c.$) of the airfoil, of the CS, and of the tab with respect to the middle section ($m.s.$). Also, g_w, g_{CS}, g_t are the non-dimensional distances with respect to b from $e.c.$ to $g.c.$ of each part. For example, g_{CS} is the distance from $e.c.^{CS}$ to $g.c.^{CS}$, where $g.c.^{CS}$ is the gravitational center of the CS singly, i.e., the blue piece only in Fig. 2 and 3.

Elastic and Inertial Parameters: the elastic parameters are the stiffnesses (k_h, k_α, k_β, k_γ) producing restorative efforts proportional to the respective displacements; the inertial parameters are the total mass of the whole airfoil (m), the inertia (I_α, I_β, I_γ) and static (S_α, S_β, S_γ) moments of mass. Note that S_i and I_i refers to the static and inertia moment of *all parts* that rotate with the gyration u_i. For example, for the 3-DOF airfoil, S_α and I_α are the static and inertia moments of the **wing-CS** around $e.c.^w$, whereas S_β and I_β are static and inertia moments of the **CS only** around $e.c.^{CS}$. On the other hand, for the 4-DOF airfoil, I_α is the inertia moment of the **wing-CS-tab** around $e.c.^w$; I_β is the inertia moment of the **CS-tab** around $e.c.^{CS}$; and I_γ is the inertia moment of the **tab only** around $e.c.^t$ (analogous for the static moments S_α, S_β and S_γ).

2.2.2 Unsteady Aerodynamics

Theodorsen (1935) presents the formulation for the unsteady aerodynamics of the 3-DOF airfoil. The potential flow for a bi-dimensional incompressible fluid is adopted. The main goal of Theodore Theodorsen in this original publication is basically to obtain the aerodynamic efforts (force and moments). For this, he considers the following procedure of dependency Efforts → Pressure → Potential velocity. This latter has its effects contributed by two parcels: source potential flow distributed around the airfoil contour (considered as a circle by the author); and vortex-type potential flow considered to represent the wake effect behind the airfoil (in the trailing-edge direction). The pressure is computed as a function of the potential velocities via unsteady Bernoulli equation for potential flow. Finally, the pressure can be integrated around the airfoil contour to obtain forces and moments.

The derivation of the efforts related to the vortex elements involves solving some integrals where the wake goes from the airfoil trailing edge to the infinite. And, the vortex strength of a single element is assumed to have an oscillatory nature - since this methodology was developed to study flutter. This hypothesis allows on to solve the complicate integrals - which actually are the generalized function of Theodorsen C_T - using Bessel and Henkel functions. As a result of this approach, the final equation for the aerodynamic efforts depends on the frequency of motion ω, such that it is written in the frequency domain $\mathbf{F}_a(s) = q\mathbf{Q}_a(s)\mathbf{u}(s)$, where $\mathbf{Q}_a(\tilde{s})$ is given by

$$\mathbf{Q}_a(\tilde{s}) = 2\left[\mathbf{M}_{nc}\ \tilde{s}^2 + (\mathbf{D}_{nc} + C_T(\tilde{s})\mathbf{R}\mathbf{S}_2)\tilde{s} + (\mathbf{K}_{nc} + C_T(\tilde{s})\mathbf{R}\mathbf{S}_1)\right] \tag{6}$$

where $s = \omega j$ is the Laplace variable, $\tilde{s} = kj$ is the modified Laplace variable which uses the reduced frequency $k = \omega b/V$ instead of the physical ω. Note that the generalized function of Theodorsen $C_T(\tilde{s})$ depends directly on the frequency. This matrix form of the aerodynamic efforts involving non-circulatory ($\mathbf{M}_{nc}$, $\mathbf{D}_{nc}$, $\mathbf{K}_{nc}$) and circulatory ($\mathbf{R}$, $\mathbf{S}_1$, $\mathbf{S}_2$) terms is presented by Edwards (1977), and they depend on the original constants of Theodorsen (1935) (T_i - indicating influence of the aileron). Check Appendix A to see the matrices.

The aerodynamic efforts need to be written in time domain $\mathbf{F}_a(t)$ to be included in the state space notation used to perform numerical simulations of the aeroelastic system in time domain. However, the function of Theodorsen $C_T(\tilde{s})$ involves transcendental functions, and therefore it is not possible to compute the inverse Laplace transform $\mathcal{L}^{-1}\{\mathbf{F}_a(s)\}$. Instead, $\mathbf{Q}_a(s)$ (Eq. 6) can be approximated by $\mathbf{Q}_{a,ap}(s)$ (Eq. 7) using Rational Functions Approximation (RFA). The minimum square method, known as Roger (1977) method, has been used since its original publication in some works (DIMITRIADIS, 2008a). Finally, the aerodynamic term can be computed with $\mathbf{F}_a(t) = \mathcal{L}^{-1}\{q\mathbf{Q}_{a,ap}(s)\mathbf{u}(s)\}$

(Eq. 8).

$$\mathbf{Q}_{a,ap}(s) = \left[\mathbf{Q}_0 + \left(\frac{b}{V}\right)\mathbf{Q}_1 s + \left(\frac{b}{V}\right)^2 \mathbf{Q}_2 s^2 + \sum_{j=1}^{n_{\text{lag}}} \frac{\mathbf{Q}_{(j+2)} s}{s + \frac{V}{b}\varrho_j}\right] \tag{7}$$

where n_{lag} is the number of aerodynamic lag parameters considered; ϱ_j is the j-th lag parameter. Also the matrices $\mathbf{Q}_i$, for $i = 0, ..., n_{\text{lag}} + 2$ are coefficients $\mathbf{C}_Q = \begin{bmatrix} \mathbf{Q}_0 & \mathbf{Q}_1 & \mathbf{Q}_2 & \dots & \mathbf{Q}_{n_{\text{lag}}+2} \end{bmatrix}$ obtained as the result of the minimum squares method. In summary, it uses Eq. (6), a range of reduced frequency and this lag parameters. See Appendix A for details of the method.

$$\mathbf{F}_a(t) = q\left[\mathbf{Q}_0\mathbf{u}(t) + \left(\tfrac{b}{V}\right)\mathbf{Q}_1\dot{\mathbf{u}}(t) + \left(\tfrac{b}{V}\right)^2\mathbf{Q}_2\ddot{\mathbf{u}}(t) + \sum_{j=1}^{n_{\text{lag}}} \mathbf{Q}_{(j+2)}\mathbf{u}_{a,j}(t)\right] \tag{8}$$

where $q = \rho V^2/2$ is the dynamic pressure, function of the flight condition (ρ is the air density and V the flow velocity); $\mathbf{u}_{a,j}(t) = \{u^h_{a,j}(t) \quad u^\alpha_{a,j}(t) \quad u^\beta_{a,j}(t) \quad u^\varrho_{a,j}(t)\}^T = \mathcal{L}^{-1}\left\{\frac{s}{s+\varrho_j V/b}\mathbf{u}(s)\right\}$ is the vector of aerodynamic lag states referring to the j-th lag state. Using the Convolution Theorem for the inverse Laplace Transform (ABELL; BRASELTON, 2018), the additional equation referring to the j-th lag states and that are part of the set of equations of the aeroelastic system is given by

$$\dot{\mathbf{u}}_{a,j}(t) = \dot{\mathbf{u}}(t) - \frac{V}{b}\varrho_j\mathbf{u}_{a,j}(t) \tag{9}$$

2.3 State Space Notation: First Order Equation

The first order equation for the aeroelastic model written with the state space notation when Roger approximation is used for the aerodynamics assumes the state vector as $\mathbf{x} = \{\dot{\mathbf{u}} \ \mathbf{u} \ \mathbf{u}_{a,1} \ ... \ \mathbf{u}_{a,n_{\text{lag}}}\}^T$, where each sub-vector has order $n_{\text{dof}} \times n_{\text{dof}}$, in such a way that $\mathbf{A}_l$ is the $N \times N$ aeroelastic matrix, with $N = (n_{\text{lag}} + 2)n_{\text{dof}}$. The aeroelastic equation Eq. (3) and the additional Eq. (9) due to the lag states are used to write the final state space equation given by

$$\dot{\mathbf{x}} = \mathbf{A}_l\mathbf{x} - \sum_l \mathbf{b}^\delta_l(u_l) - \sum_l \mathbf{b}^C_l(\dot{u}_l) \tag{10}$$

such that

$$\mathbf{b}^\delta_l(u_l) = \left\{\mathbf{M}_a^{-1}\mathbf{f}^\delta_l \ 0 \ ... \ 0\right\}^T \quad \text{and} \quad \mathbf{b}^C_l(\dot{u}_l) = \left\{\ \mathbf{M}_a^{-1}\mathbf{f}^C_l \ 0 \ ... \ 0\right\}^T \tag{11}$$

where the subscript l in $\mathbf{A}_l$ indicates that the modified $\mathbf{K}_l$ described in Eq. 3 to include the freeplay effect is used instead of the full diagonal stiffness matrix $\mathbf{K}$ to construct the matrix $\mathbf{A}$ described in Appendix A. The vectors $\mathbf{b}^\delta_l$ and $\mathbf{b}^C_l$ are $N \times 1$, analogous to that presented by Conner, Virgin and Dowell (1996) for freeplay. $\mathbf{f}_l^\delta$ e $\mathbf{f}_l^C$ are described in Eq. (3) and accounts for the discontinuous effects created by the presence of freeplay and friction, respectively.

2.4 Particular Configuration of Airfoils

The meaning/description of the physical and geometric symbols of the structural model are indicated in Tab. 1. Note that I_α, I_β, S_α, S_β have different meanings for the 3-DOF and 4-DOF airfoils. Also, the inertia moments, the static moments, the mass and the stiffness are all written per unit span, since this is the typical way of writing the Eq. (4) and (5).

Three different airfoils are utilized in this study; their specific configurations are detailed in Table 2. The parameters for airfoil $\mathcal{A}_1$ have been selected to maintain consistency with the levels employed in previous works by Conner *et al.* (1997) and Liu and Dowell (2005). Airfoil $\mathcal{A}_2$ features adjusted parameters to observe time responses that include higher harmonics. Lastly, airfoil $\mathcal{A}_3$ shares the same geometric and mass parameters as airfoil $\mathcal{A}_1$, with necessary modifications to incorporate a trailing edge tab on the primary control surface. For practical purposes, the NACA 0012 airfoil is used, and the mass parameters can be determined by considering the masses and geometric measurements (refer to Eq. 26 and 29 in Appendix A). In terms of stiffness, each structural degree of freedom can be excited independently, leading to the extraction of uncoupled natural frequencies, denoted as $\omega_{(.)}$. Subsequently, the stiffness parameters are calculated as follows: $k_h = m\omega_h^2$, $k_\alpha = I_\alpha\omega_\alpha^2$, $k_\beta = I_\beta\omega_\beta^2$, and $k_\gamma = I_\gamma\omega_\gamma^2$. It is worth noting that this work assumes zero structural damping.

For the aerodynamics, all the systems consider $n_{\text{lag}} = 7$ where the lag parameters $\varrho_1 = 0.05$, $\varrho_2 = 0.21$, $\varrho_3 = 0.48$, $\varrho_4 = 0.85$, $\varrho_5 = 1.33$, $\varrho_6 = 1.91$ and $\varrho_7 = 2.60$ are employed (RIBEIRO; DOWELL; BUENO, 2021). The air density is considered fixed at the sea level value 1.225 kg/m^3.

	Description in 3-DOF	Description in 4-DOF	Measure Unity
s_p	Span		m
b	Semi-chord		m
a	Non-dimensional distance* (w.r.t b) from $m.s.$ to $e.c.^w$		-
c	Non-dimensional distance (w.r.t b) from $m.s.$ to $e.c.^\beta$		-
d	-	Non-dimensional distance (w.r.t b) from $m.s.$ to $e.c.^\gamma$	-
m	Total mass (per unit span)		kg/m
I_α	Inertia moment (per unit span) of **wing-CS** around $e.c.^w$	Inertia moment (per unit span) of **wing-CS-tab** around $e.c.^w$	kgm^2 /m
I_β	Inertia moment (per unit span) of **CS** around $e.c.^\beta$	Inertia moment (per unit span) of **CS-tab** around $e.c.^\beta$	kgm^2 /m
I_γ	-	Inertia moment (per unit span) of **tab** around $e.c.^\gamma$	kgm^2 /m
S_α	Static moment (per unit span) of **wing-CS** around $e.c.^w$	Static moment (per unit span) of **wing-CS-tab** around $e.c.^w$	kgm/m
S_β	Static moment (per unit span) of **CS** around $e.c.^\beta$	Static moment (per unit span) of **CS-tab** around $e.c.^\beta$	kgm/m
S_γ	-	Static moment (per unit span) of **tab** around $e.c.^\gamma$	kgm/m
k_h	Stiffness in plunge h (per unit span)		(N/m)/m
k_α	Stiffness in pitch α (per unit span)		(Nm/rad)/m
k_β	Stiffness in β (per unit span)		(Nm/rad)/m
k_γ	-	Stiffness in γ (per unit span)	(Nm/rad)/m

*Positive and negative values to the right and to the left-hand side of middle section ($m.s.$).

Table 1 – Description of the 3-DOF and 4-DOF airfoils physical and geometric parameters.

	airfoil $\mathcal{A}_1$	airfoil $\mathcal{A}_2$	airfoil $\mathcal{A}_3$
n_{dof}	3	3	4
s_p	0.5	0.3	0.5
b	0.15	0.115	0.15
a	−0.4	−0.42609	−0.4
c	0.6	0.64783	0.5
d	–	–	0.8
m	7.5122	2.40585	7.5122
I_α	$4.7741\ 10^{-2}$	$1.38524\ 10^{-2}$	$4.7741\ 10^{-2}$
I_β	$3.6423\ 10^{-4}$	$8.06206\ 10^{-5}$	$8.4467\ 10^{-4}$
I_γ	–	–	$2.8042\ 10^{-5}$
S_α	0.276426	0.114219	0.276426
S_β	0.011187	0.003264	0.020980
S_γ	–	–	0.001681
k_h	2669.12	854.81	2669.12
k_α	188.47	26.80	188.47
k_β	2.82	1.0312	6.54
k_γ	–	–	0.36

Table 2 – Physical and geometric parameters for the airfoil configurations.

3 Time Domain Integration: the Extended Hénon's Technique

This chapter focuses on the time domain method to perform the numerical integration. The Hénon's technique used to reduce errors when considering discontinuous nonlinearities in the numerical integration process is described. This technique basically works as an event detection method, where a change in the integration variable allows one to identify the exact time at which some event happens, and this is the main reason why it is particularly useful for discontinuous nonlinearities.

This chapter introduces a mathematically compact notation to simplify the computation implementation of the method, which is suitable for any arbitrary discontinuous dynamic system. In addition, a new coordinate system is defined to rewrite the equation of motion of aeroelastic systems. The proposal defines a displacement vector with both generalized and physical variables to simplify the computational implementation of the Hénon's technique when the generalized coordinates are required.

Friction and asymmetric freeplay are considered acting on a control surface of a 3-DOF airfoil, and the Hénon's technique is extended to attend both nonlineariaties simultaneously during the time integration. The results show that the extended Hénon's technique provides more accurate LCO predictions. Additionally, this chapter discusses the influence of asymmetric freeplay and friction on the LCO of an airfoil with control surface.

Finally, the end of this chapter includes the general procedure to properly identify LCO and to generate bifurcation diagrams - important part of the results in this thesis - using the time integration method.

3.1 Methodology for the Time Domain Integration

A first order equation of an Ordinary Differential Equation in which v is the independent variable and $\mathbf{y}$ is the state vector with the dependent variables, typically is written as $\dot{\mathbf{y}} = \mathbf{g}(v, \mathbf{y})$, and conceptually it can be integrated numerically with several methods. A general equation for explicit methods, meaning that computing the solution $\mathbf{y}_{i+1}$ depends exclusively on the previous state vector $\mathbf{y}_i$, and it is given by

$$\mathbf{y}_{i+1} = \mathbf{y}_i + s_v \; F(v_i, \mathbf{y}_i) \tag{12}$$

where $s_v = v_{i+1} - v_i$ is the discrete step of the independent variable in which the integration is performed.

Each explicit numerical integration method is defined by a different function $F(v_i, \mathbf{y}_i)$ that, in general, is computed using the ODE $\mathbf{g}(v, \mathbf{y})$. For example, the conventional fourth order Runge-Kutta method is defined by $F(v_i, \mathbf{y}_i) = \frac{1}{6}(\mathbf{k}_1 + 2\mathbf{k}_2 + 2\mathbf{k}_3 + \mathbf{k}_4)$, where each $\mathbf{k}_j$ is an approximation for the first derivative at some point between $\mathbf{y}_i$ and $\mathbf{y}_{i+1}$. Check Appendix B to note that $\mathbf{k}_1$ is the first derivative $\dot{\mathbf{y}} = \mathbf{g}(v_i, \mathbf{y}_i)$ at the current value v_i; $\mathbf{k}_2$ and $\mathbf{k}_3$ are estimates of the first derivative at the middle of the interval $v_i + \frac{s_v}{2}$ and, finally, $\mathbf{k}_4$ estimates $\dot{\mathbf{y}}$ at the end of the interval, v_{i+1}.

The 3-DOF airfoil studied in this chapter has its first order equation of motion detailed in Eq. (10), where time t is the independent variable and $\mathbf{x}$ is the state vector with the dependent variables. Assuming the general notation for the displacement vector $\mathbf{u} = \{u_1 \; ... \; u_l \; ... \; u_{n_{\mathrm{dof}}}\}^T$, the nonlinear DOF is defined herein as the l-th DOF. For a clear understanding of the motivation of why using Hénon's technique, only freeplay is considered acting on u_l. Also, a lighter notation is used for the freeplay boundaries by omitting the superscript l. The issue related to freeplay regarding numerical integration is its discontinuity, where $\dot{\mathbf{x}} = \mathbf{h}(t, \mathbf{x})$ changes according to u_l (the k-th state in the state vector $\mathbf{x}$) in such a way that the set of real numbers $\mathbb{R}$ representing u_l can be divided in three different intervals $A_\delta =]-\infty, -\delta_L[$; $B_\delta = [-\delta_L, \delta_R]$; and $C_\delta =]\delta_R, +\infty[$. This division shows clearly two switching points $x_{k_\delta} = -\delta_L$ and $x_{k_\delta} = \delta_R$.

If a conventional Runge-Kutta method is used to integrate the system with freeplay in time, the issue illustrated in Fig. 4 often happens. The state x_{k_δ} is such that $x_{k_\delta} > \delta_R$ at the i-th time instant t_i and, hypothetically, integrating the equation using the time step Δt, the value $x_{k_\delta} = \delta_R$ is jumped up. Therefore, the corresponding equation is not necessarily used between the switching point and the time $t_i + \Delta t$. The possible use of the no corresponding equation is the specific motivation to use the Hénon's technique, i.e., to find the exact switching point allowing one to change the equation appropriately.

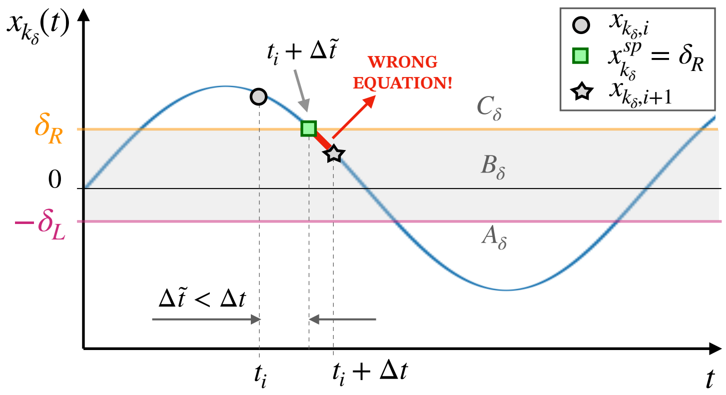

Figure 4 – Illustrative representation of the intervals and switching points for freeplay $(A_\delta, B_\delta, C_\delta)$.

The idea behind the Hénon's technique is well-established in the literature. Also, demonstrated is the improvement of numerical accuracy if time responses of aeroelastic systems with freeplay are computed using the approach (HENON, 1982; CONNER; VIRGIN; DOWELL, 1996; BUENO; GÓES; GONÇALVES, 2014; DAI *et al.*, 2015).

The Hénon's technique is a method of changing the independent variable from t (the time) to the motion, i.e., the state x_k associated with the nonlinearity at every occurrence of the event of a switching point being jumped, i.e., the equation of motion must change. It has been successfully applied to the freeplay nonlinearity and for this case, $x_k = x_{k_\delta} = u_l$, and the Hénon's approach is applied to assure that x_{k_δ} can achieve the freeplay's boundaries, i.e., $-\delta_L$ and δ_R, which allows switching to the appropriate vector $\mathbf{b}_l^\delta$ at the correct time instant during the integration process.

Coming back to the issue illustrated in Fig. 4, the solution proposed by Hénon's technique is replacing the independent variable to x_{k_δ} and integrating that i-th point using the spatial step $\Delta x_k = (\delta_R - x_{k_\delta})$. As a result of this additional iteration in a new variable, a different time step $\Delta\tilde{t} = \Delta\tilde{x}_{k_\delta}$, for $\tilde{x}_{k_\delta} \in \tilde{\mathbf{x}}$, that reaches the exact event (switching point) is computed, where $\tilde{\mathbf{x}}$ is the state vector of the system when the new independent variable is x_{k_δ}.

3.1.1 Matrix Notation for Hénon's Technique

For the aeroelastic systems studied in this work, integrating the ODE in time means that the march is performed by $\mathbf{x}_{i+1} = \mathbf{x}_i + \Delta t\ F(t_i, \mathbf{x}_i)$, i.e., $\dot{\mathbf{x}}$ is integrated in time obtaining $\mathbf{x}$, whose k-th element is the nonlinear state u_l. Every time that an event is identified (the switching point is jumped), a different iteration must be performed by

$\tilde{\mathbf{x}}^{sp} = \tilde{\mathbf{x}}_i + \Delta x_k \; F(x_{k,i}, \tilde{\mathbf{x}}_i)$, where $\tilde{\mathbf{x}}^{sp}$ is the new state vector at the switching point. The variables t and x_k are exchanged for this new iteration: the integration is performed in x_k and t is the k-th element of the new state vector $\tilde{\mathbf{x}}$. The other elements in $\tilde{\mathbf{x}}$ are the same of those in $\mathbf{x}$, as follows

$$\mathbf{x} = \{x_1, \; ..., \; x_k, \; ..., \; x_N\}^T$$
$$\tilde{\mathbf{x}} = \{x_1, \; ..., \; t, \; ..., \; x_N\}^T$$

To obtain $\tilde{\mathbf{x}}$ as the result of an integration in the described conditions, an ODE as $\tilde{\mathbf{x}}' = \tilde{\mathbf{h}}(x_k, \tilde{\mathbf{x}})$ must be derived (the prime indicates derivation with respect to x_k). Two operations are applied at the regular ODE with independent variable t

$$\dot{\mathbf{x}} = \mathbf{h}(t, \mathbf{x}) = \left\{\frac{dx_1}{dt}, \; ..., \; \frac{dx_k}{dt}, \; ..., \; \frac{dx_N}{dt}\right\}^T = \{h_1, \; ..., \; h_k, \; ..., \; h_N\}^T$$

to obtain the modified ODE with independent variable x_k (used during the Hénon's iteration). Those operations are: if $j \neq k$, the new ODE is such that $\tilde{h}_j = \frac{h_j}{h_k}$; otherwise, $\tilde{h}_k = \frac{1}{h_k}$. Note the physical interpretation of $\tilde{h}_j$, which represents how the variable h_j changes with h_k. If a more typical question when dealing with dynamic systems is 'which position the system reaches after a time Δt is passed?' when integrating $\dot{\mathbf{x}}$ with respect to time; a vector of derivatives $\tilde{\mathbf{x}}'$ is constructed for integration with respect to x_k to address a different question of 'how much time is required for the system to reach an event (e.g., the freeplay boundary)?'. This new vector is given by

$$\tilde{\mathbf{x}}' = \tilde{\mathbf{h}}(x_k, \tilde{\mathbf{x}}) = \left\{\frac{dx_1}{dx_k}, \; ..., \; \frac{dt}{dx_k}, \; ..., \; \frac{dx_N}{dx_k}\right\}^T = \left\{\tilde{h}_1, \; ..., \; \tilde{h}_k, \; ..., \; \tilde{h}_N\right\}^T$$

then, a compact matrix notation is written as a contribution of this work for the modified first order ODE to be integrated with a regular explicit numerical method during the Hénon's iteration. The equation is given by

$$\tilde{\mathbf{x}}' = \tilde{\mathbf{h}}(x_k, \tilde{\mathbf{x}}) = \frac{1}{h_k}(\mathbf{W} \; \mathbf{h}(t, \mathbf{x}) + \mathbf{v}) \tag{13}$$

where $\mathbf{v} = \{0 \; ... \; 0 \;\; 1|_k \;\; 0 \; ... \; 0\}^T$ is the $N \times 1$ vector (where $|_k$ indicates the k-th row); $h_k = \mathbf{v}^T\mathbf{h}(t, \mathbf{x}) \in \mathbb{R}$; and $\mathbf{W} = \mathbf{I}_N - \mathbf{v}\mathbf{v}^T$ is a matrix where $\mathbf{I}_N$ is a N dimensional identity matrix. Note that the elements of $\mathbf{W}$ are $W_{jj} = 1$ if $j \neq k$ $(j = 1, ..., N)$ and $W_{kk} = 0$.

In summary, every time a switching point is jumped between $\mathbf{x}_i$ and $\mathbf{x}_{i+1}$:

1. the Hénon iteration is performed with step $\Delta x_k = x_k^{sp} - x_{k,i}$ to find the jumped switching point $\tilde{\mathbf{x}}^{sp} = \tilde{\mathbf{x}}_i + \Delta x_k \; F(x_{k,i}, \tilde{\mathbf{x}}_i)$ using the equation related to sub-linear

region of before crossing the switching point. See Appendix B for details of computing $F(x_{k,i}, \tilde{\mathbf{x}}_i)$ for Runge-Kutta methods;

2. the time between $\mathbf{x}_i$ and $\tilde{\mathbf{x}}^{sp}$ is found in $\Delta\tilde{t} = [\Delta x_k \; F(x_{k,i}, \tilde{\mathbf{x}}_i)]\,|_k$;

3. a regular iteration in time with step $\Delta t - \Delta\tilde{t}$ is performed with the new equation related to the sub-linear region of after crossing the switching point using $\mathbf{x}_{i+1} = \mathbf{x}^{sp} + (\Delta t - \Delta\tilde{t}) \; F(t_i + \Delta\tilde{t}, \mathbf{x}^{sp})$.

3.1.2 Extended Hénon's Technique for Freeplay and Friction Simultaneously

The Hénon's approach is applied to the freeplay nonlinearity whenever x_{k_δ} changes from one to another interval. However, if the friction nonlinearity is simultaneously considered in the analysis, the vector $\mathbf{b}_l^C$ changes whenever $\dot{u}_l = x_{k_c} = 0$ (note that $x_{k_c} = \dot{x}_{k_\delta}$, $k_\delta = n_{\text{dof}} + l$, and $k_c = l$). In this case, two new intervals $A_c =]-\infty, 0[$ and $B_c = [0, +\infty[$ are introduced to represent x_{k_c}, and the resulting process for applying the method when freeplay and friction are present considers five intervals $i = A_\delta \cap A_c$, $ii = A_\delta \cap B_c$, $iii = B_\delta$, $iv = C_\delta \cap A_c$, and $v = C_\delta \cap B_c$, as illustrated by the schematic representation in Fig. 5.

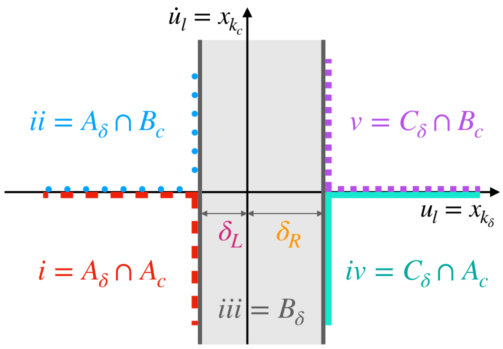

Figure 5 – Schematic representation of five intervals resulting for considering the freeplay and Coulomb friction nonlinearities simultaneously.

Switching Points of Intervals

Applying this extended Hénon's technique to the five intervals, there are four switching points. These points are x_k equal to: $x_{k_\delta} = \delta_R$, $x_{k_\delta} = -\delta_L$, $x_{k_c} = 0$ if $u_l > 0$, and $x_{k_c} = 0$ if $u_l < 0$. For a cycle of motion with only the first harmonic being significant, the computational algorithm needs to perform the Hénon's approach six times, and for four of them the independent variable is $x_k = x_{k_\delta}$ with a spatial step defined in terms of displacement ($\Delta x_k = \delta_{(.)} - x_{k_\delta}$, where $\delta_{(.)}$ is equal to δ_R or $-\delta_L$, and $x_{k_\delta} = u_l$). On the other hand, for the other two of them, which are associated to the friction (i.e., for the maximum and minimum values of u_l), the independent variable is $x_k = x_{k_c}$ and the space step is defined in terms of velocity ($\Delta x_k = 0 - x_{k_c} = -\dot{u}_l$).

3.1.3 Extended Hénon's Technique in Generalized Coordinates

Mainly for a multiple degree-of-freedom system, aeroelastic systems are commonly written in the generalized coordinate system using the matrix of undamped elastic modes $\mathbf{\Phi} = [\mathbf{\Phi}_1 \ldots \mathbf{\Phi}_{n_{\mathrm{dof}}}]$ obtained by extracting the eigenvectors from the matrix $\mathbf{M}^{-1}\mathbf{K}$, where $\mathbf{K}$ is the structural stiffness matrix for no freeplay. $\mathbf{\Phi}_j$, $j = 1, \ldots, n_{\mathrm{dof}}$ is j-th structural undamped mode. Using this coordinate system, the physical displacement vector $\mathbf{u}$ is replaced by $\mathbf{u}_\phi = \{u_1^\phi \cdots u_r^\phi \cdots \; u_{n_{\mathrm{dof}}}^\phi\}^T$, which contains generalized displacements. The generalized displacement u_r^ϕ is associated to the r-th mode such that $\mathbf{u} = \mathbf{\Phi}_1 u_1^\phi + \ldots + \mathbf{\Phi}_r u_r^\phi + \ldots + \mathbf{\Phi}_{n_{\mathrm{dof}}} u_{n_{\mathrm{dof}}}^\phi$.

The generalized coordinate system is typically used to truncate the system matrices with $n_{\mathrm{tru}} << n_{\mathrm{dof}}$ modes because n_{dof} can be thousands DOFs to describe structures like a commercial airplane. In these cases $\mathbf{\Phi}$ is a $n_{\mathrm{dof}} \times n_{\mathrm{tru}}$ rectangular matrix. Using this coordinate system the physical state x_k is not explicitly an element into the state vector. However, the physical state vector can be obtained at each time instant by computing $\mathbf{x} = (\mathbf{I}_2 \otimes \mathbf{\Phi})\mathbf{x}_\phi$, where $\mathbf{I}_2$ is an identity matrix 2×2 and $\otimes$ indicates de Kronecher product.

Let r be the mode corresponding to the l-th degree of freedom, associated to the nonlinearities action. A modified generalized coordinate system (MGCS) is introduced to ease the computational implementation of the Hénon's technique. The MGCS creates a hybrid displacement vector $\mathbf{u}_\psi = \{u_1^\phi \cdots u_l \cdots u_n^\phi\}^T$ which contains all except one generalized displacement, i.e., u_r^ϕ is replaced by u_l such that $\mathbf{u}_\psi$ contains the physical displacement u_l related to the nonlinearities, instead of the generalized displacement associated to mode of the l-th degree of freedom. In this case, the state space representation (Eq. 13) can be employed considering $k_\delta = n_{\mathrm{tru}} + r$ to the freeplay and $k_c = r$ to the friction nonlinearity to perform the numerical integration process if n_{tru} modes are used to truncate the system of equations. Note that in this case the state vector is $(n_{\mathrm{tru}}+2)n_{lag}$ if the Roger's approximation is used.

Considering ϕ_{ij} the elements of $\mathbf{\Phi}$ (i-th row and j-th column), a simple procedure can be employed to obtain the matrix $\mathbf{\Psi}$ such that $\mathbf{u} = \mathbf{\Psi}\mathbf{u}_\psi$. Note that $u_l = \sum_{j=0}^{n_{\mathrm{dof}}}[\phi_{lj} u_j^\phi]$, and as a consequence, $u_r^\phi = [u_l - \sum_{j \neq r}(\phi_{lj} u_j^\phi)]/\phi_{lr}$. Then, the matrix $\mathbf{\Psi}$ can be written using an identity matrix $\mathbf{I}_{n_{\mathrm{tru}}}$ with dimension n_{tru} and two auxiliary vectors $\mathbf{w}_l$ $n_{\mathrm{dof}} \times 1$ and $\mathbf{w}_r$

$n_{\text{tru}} \times 1$, such that $\mathbf{w}_l = \{0 \ \dots \ 0 \ \ 1|_l \ \ 0 \ \dots \ 0\}^T$ and $\mathbf{w}_r = \{0 \ \dots \ 0 \ \ 1|_r \ \ 0 \ \dots \ 0\}^T$. So, the new basis $\boldsymbol{\Psi}$ is given by

$$\boldsymbol{\Psi} = \boldsymbol{\Phi}\left[\mathbf{I}_{n_{\text{tru}}} - \frac{\mathbf{w}_r}{\mathbf{w}_l^T\boldsymbol{\Phi}\mathbf{w}_r}\left(\mathbf{w}_l^T\boldsymbol{\Phi} - \mathbf{w}_r^T\right)\right] \tag{14}$$

and note that $\mathbf{w}_l^T\boldsymbol{\Phi}\mathbf{w}_r$ is the scalar ϕ_{lr}, i.e., the element in the l-th row and r-th column of $\boldsymbol{\Phi}$.

Using the matrix $\boldsymbol{\Psi}$, the physical displacement vector in equation of motion is replaced by $\boldsymbol{\Psi}\mathbf{u}_\psi$ (and similarly to its derivatives $\dot{\mathbf{u}} = \boldsymbol{\Psi}\dot{\mathbf{u}}_\psi$ and $\ddot{\mathbf{u}} = \boldsymbol{\Psi}\ddot{\mathbf{u}}_\psi$), and both sides of that equation are pre-multiplied by $\boldsymbol{\Psi}^T$ to obtain the final equation written in this new coordinate system.

3.1.4 Particularities for the 3-DOF Airfoil with Freeplay in CS

If the extended Hénon's method is employed to study a 3-DOF airfoil as $\mathcal{A}_1$ with freeplay and Coulomb friction in the control surface, i.e., on the β degree of freedom (dof), $l = 3$ since β is the third element into the vector $\mathbf{u}$, i.e., $u_l = \beta$ and $\dot{u}_l = \dot{\beta}$. It means that the piecewise vector $\mathbf{f}_3^\delta$ depends on the control surface stiffness k_β. Considering the modal matrix $\boldsymbol{\Phi} \in \mathbb{R}^{3\times3}$ obtained from the undamped structural system without freeplay, the proposed new coordinate system for the 3 DOF airfoil is given by $\boldsymbol{\Psi} = [\boldsymbol{\Psi}_1 \ \boldsymbol{\Psi}_2 \ \boldsymbol{\Psi}_3]$, where $\boldsymbol{\Psi}_1 = \left\{\left(\phi_{11} - \frac{\phi_{31}\phi_{13}}{\phi_{33}}\right) \ \left(\phi_{21} - \frac{\phi_{31}\phi_{23}}{\phi_{33}}\right) \ 0\right\}^T$, $\boldsymbol{\Psi}_2 = \left\{\left(\phi_{12} - \frac{\phi_{32}\phi_{13}}{\phi_{33}}\right) \ \left(\phi_{22} - \frac{\phi_{32}\phi_{23}}{\phi_{33}}\right) \ 0\right\}^T$ and $\boldsymbol{\Psi}_3 = \{\frac{\phi_{13}}{\phi_{33}} \ \ \frac{\phi_{23}}{\phi_{33}} \ \ 1\}^T$. The corresponding new displacement vector contains generalized and one physical displacements such that $\mathbf{u}_\psi = \{u_1^\phi \ u_2^\phi \ \beta\}^T$, and with this approach, the extended Hénon's technique can be easily employed. Also, note that for this non-truncated system $\mathbf{w}_l = \mathbf{w}_r = \{0 \ \ 0 \ \ 1\}^T$.

3.2 Results and Discussions

Figure 6 shows two responses of the 3-DOF airfoil $\mathcal{A}_1$ comparing the effect of freeplay presence. It reveals that LCO is generated by the presence of freeplay, which is in accordance to literature, whereas for the same flight condition the solution is a decay type when there is no freeplay. Also, Fig. 7 shows the phase lag error present in the solution integrated with classical Runge-Kutta method (RK), which is corrected when the Hénon's technique is applied. A reference solution is obtained by employing the RK method with a time step much smaller than others. Therefore, the figure shows that the Hénon's technique applied with a time step $\Delta t = 1.10^{-3}$ s produces a solution as accurate as the one obtained with RK method when $\Delta t = 1.10^{-5}$ s, which causes a reduction of computational costs (see Appendix B for convergence information about the methods).

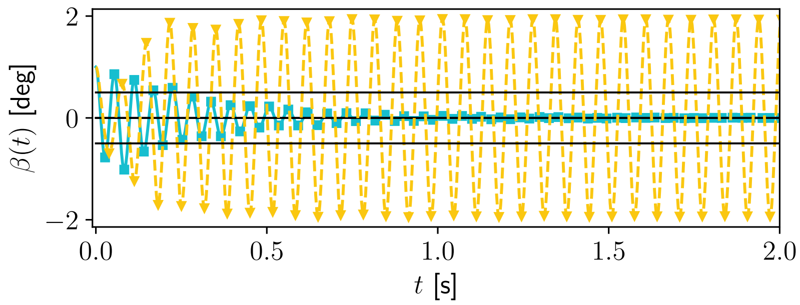

Figure 6 – Responses of airfoil $\mathcal{A}_1$ with symmetric freeplay $\delta^\beta = 0.5°$ (dashed line) and without freeplay (solid line).

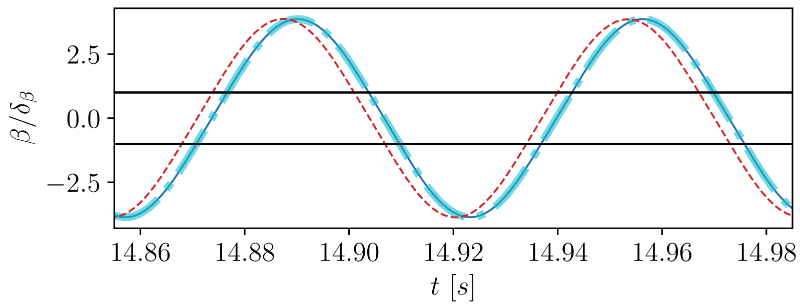

Figure 7 – Responses showing the phase lag error of classical RK method (dashed line) corrected by Hénon's technique (thin solid line) when $\Delta t = 1.10^{-3}$ s. The reference (dot-dashed line) is a classical RK method with smaller time step $\Delta t = 1.10^{-5}$ s.

3.2.1 Time Integration of the System with Freeplay and Friction

Hénon's technique has been successfully employed in literature for the freeplay nonlinearity only (BUENO; GÓES; GONÇALVES, 2014). However, if both freeplay and friction are simultaneously considered during the motion, the extended Hénon's method needs to be employed to improve the numerical accuracy.

Figure 8a shows a comparison of three different strategies used to integrate the nonlinear equations. They are obtained considering the two nonlinearities simultaneously. Each of those is compared with a reference result, which can be compute for example with the classical RK when a much smaller time step is employed. Those three cases are normalized by the error associated to this classical RK (see the unitary value in the first bar in Fig. 8a HF indicates the Hénon's strategies applied only to the freeplay, while H indicates that the approach is employed for both freeplay and friction nonlinearities. Note that this last one achieves a more accurate result. Although it is omitted here, the error is higher than the HF case if the approach is employed only for the friction nonlinearity. Finally, Fig. 8b shows the phase lag error increasing over time if the Hénon's strategy of changing the variable of integration is not employed for the system with freeplay and friction. This figure shows that this error, computed as a time delay in relation to the reference result, exhibits a cyclic behavior, increasing linearly. Note that a phase lag of 180 deg indicates an opposite phase response, whilst the 360 deg means an entire period of phase lag, where the solutions come back to be coincident (with no phase lag).

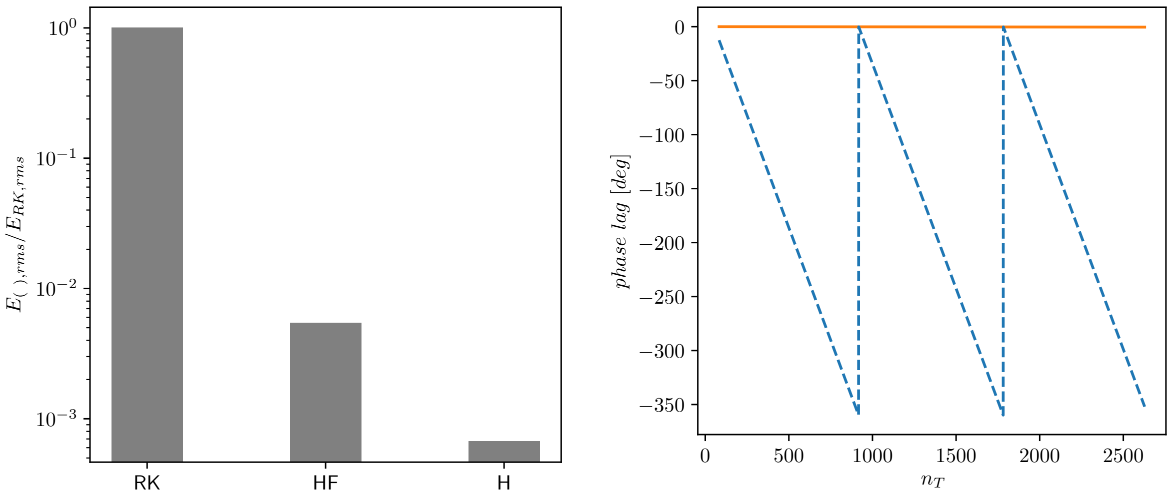

(a) (b)

Figure 8 – (a) Numerical normalized quadratic error comparing the classical RK algorithm, Hénon's technique applied to the freeplay nonlinearity only (HF), and applied to the both freeplay and friction nonlinearities (H); (b) phase lag in relation to the reference result for H (solid line) and RK (dashed line).

3.2.2 Effect of Freeplay in LCOs Amplitude

Different amplitudes of symmetric freeplay ($\delta^\beta = \delta^\beta_R = \delta^\beta_L$) are used to perform time integration of airfoil $\mathcal{A}_1$ improved with Hénon's technique for airspeed $V = 30$ m/s. Figure 9 shows the LCO amplitudes are larger for higher freeplay sizes. This behavior can also be observed in Fig. 10a, which reveals that the LCO amplitude grows linearly with the freeplay size. In this figure, each plotted symbol indicates the inversion point of CS when the steady state is established, i.e., indicates β when $\dot{\beta} = 0$. The last section of this chapter explains how those points are captured during the time integration by making use of Hénon's technique features to identify and compute an event. Also, the same kind of diagram for asymmetric freeplay is shown in Fig. 10b, where a range of the ratio $p_R = \delta^\beta_R/(\delta^\beta_R + \delta^\beta_L)$ is considered to plot the LCO amplitudes. The variables β_R and β_L are used to indicate the amplitude in module, respectively, of the positive and negative inversion points. Note that although the total freeplay gap for all cases is $1°$, the amplitude is larger in the direction of the larger freeplay boundary. For example, for the ratio $\delta^\beta_R > \delta^\beta_L$, the positive amplitude is larger than the negative ($\beta_R > \beta_L$) and vice-versa.

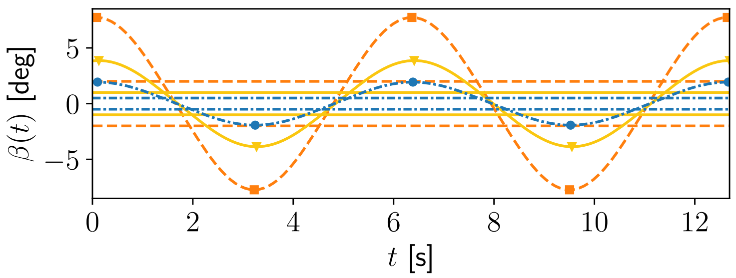

Figure 9 – LCO for different symmetric freeplay amplitudes for $V = 30$ m/s (dash-dotted line: $\delta^\beta = 0.5°$; solid line: $\delta^\beta = 1°$; dashed line: $\delta^\beta = 2°$). The horizontal lines represent the freeplay boundaries.

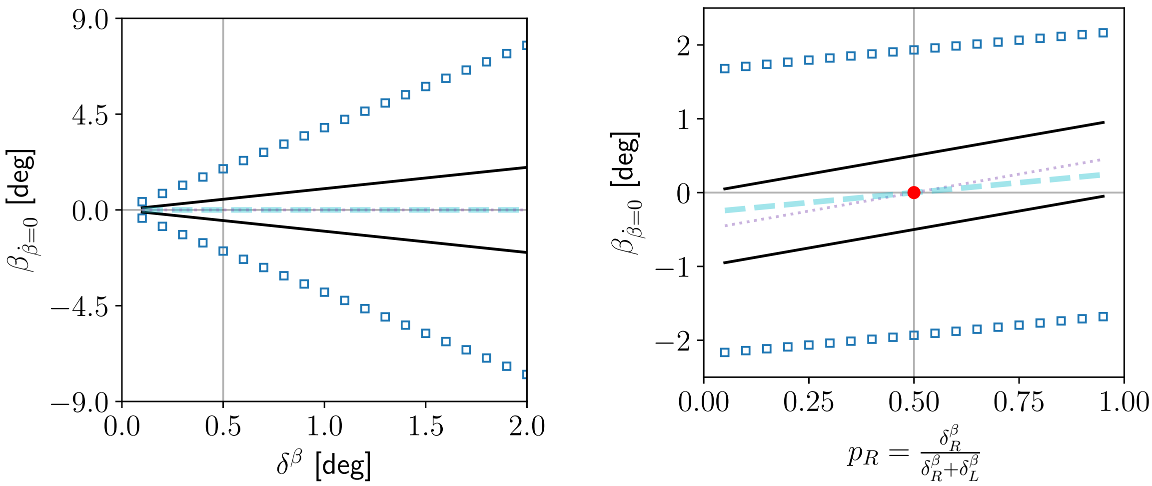

(a) (b)

Figure 10 – Diagram of LCO amplitudes for $V = 30$ m/s against (a) symmetric freeplay and (b) asymmetric freeplay with fixed total freeplay gap $\delta^\beta_R + \delta^\beta_L = 1°$. The solid black lines indicate the freeplay boundaries (δ^β_R on top, and $-\delta^\beta_L$ on bottom). The dotted line is the center of freeplay $\bar{\delta}$ and the dashed line is the middle point between the extremes $\bar{\beta}$.

Regarding the behavior of LCO when varying the parameter airspeed V, Fig. 11 shows the amplitude (left) and fundamental frequency (right) for three cases of freeplay with total gap size $1°$, two of them are opposite cases of asymmetric freeplay whilst the other is the symmetric case $\delta^\beta = \delta^\beta_R = \delta^\beta_L = 0.5°$. It is possible to see how the frequency changes with airspeed. The cases of opposite asymmetric cases have the same frequency for a particular flight condition. Also, for the most part of airspeed range, the frequency of asymmetric cases is quite similar to the symmetric case, which becomes larger for higher speeds (see detail in the right plot of Fig. 11). Regarding the amplitude, the left-hand side of the figure shows that the effect of asymmetry is smaller for higher speeds, since the LCO amplitudes of the asymmetric cases become more similar to the symmetric case.

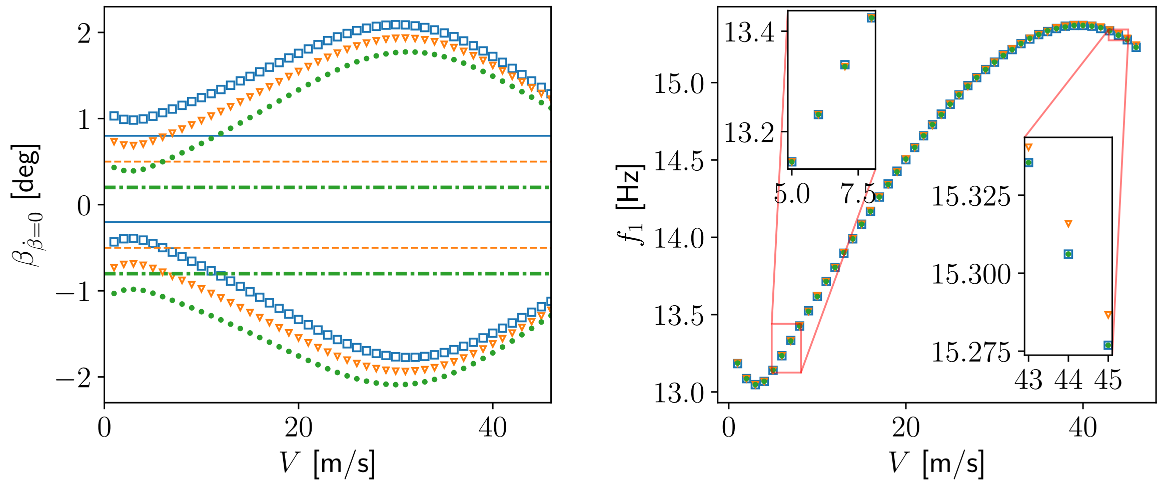

Figure 11 – Diagram of LCO amplitudes against airspeed, inversion points (left) and fundamental frequency (right) (square and solid line: $\delta^\beta_R = 0.8°, \delta^\beta_L = 0.2°$; triangle and dashed line: $\delta^\beta = \delta^\beta_R = \delta^\beta_L = 0.5°$; circle and dot-dashed: $\delta^\beta_R = 0.2°, \delta^\beta_L = 0.8°$). Horizontal lines are the freeplay boundaries.

Regarding some nondimensional parameters relating LCO amplitudes and freeplay boundaries, in both diagrams for symmetric and asymmetric freeplay of Fig. 10, the dotted line indicates the geometric center of freeplay $\bar{\delta} = [\delta^\beta_R + (-\delta^\beta_L)]/2$ and the dashed line is the middle position between inversion points $\bar{\beta} = [\beta_R + (-\beta_L)]/2$. For symmetric freeplay, these two values are coincident, both at $\beta = 0°$ (note the red point for $p_R = 0.5$ in Fig. 10b). On the other hand, although the values are different for asymmetric freeplay, the ratio between these central values $\bar{\beta}/\bar{\delta}$ has a small variation with p_R. For example, Fig. 12b shows that $\bar{\beta}/\bar{\delta} \approx 0.27$ for $V = 46$ m/s whilst is $\bar{\beta}/\bar{\delta} \approx 0.54$ for $V = 30$ m/s. The detail of this figure shows a curve with shape close to a second order polynomial which indicates that this ratio is the same for opposite asymmetric freeplays (i.e., when the sum of their p_R is 1). Besides confirming this behavior, Fig. 10a also shows the dependency of this ratio with the flight condition, revealing that the center point of amplitude decreases to the direction of zero when the airspeed increases.

Another nondimensional is the ratio of the total LCO amplitude $\beta_{\text{tot}} = \beta_R + \beta_L$ with respect to the total freeplay gap $\delta_{\text{tot}} = \delta^\beta_R + \delta^\beta_L$. This ratio also has a small variation with p_R for a particular flight condition (see Fig. 13b where the total variation occurs in the first decimal). This subfigure also confirms that opposite cases of asymmetric freeplay presents the same ratio, which has its larger value for the symmetric freeplay ($p_R = 0.5$). Figure 13a shows how the ratio varies with the airspeed. One can notice that although the ratio is more different between the symetric and asymmetric cases for higher speeds, the ratio is still quite similar regardless the freeplay boundaries.

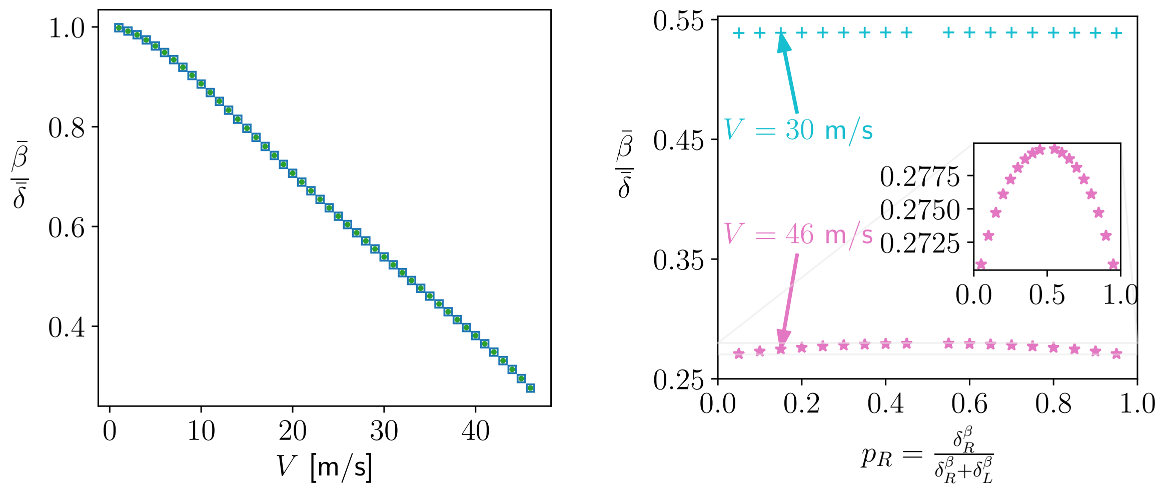

(a) (b)

Figure 12 – Diagram showing the ratio between central values (a) against airspeed (square: $p_R = 0.8$; circle: $p_R = 0.2$) and (b) against asymmetric freeplay with total gap 1°.

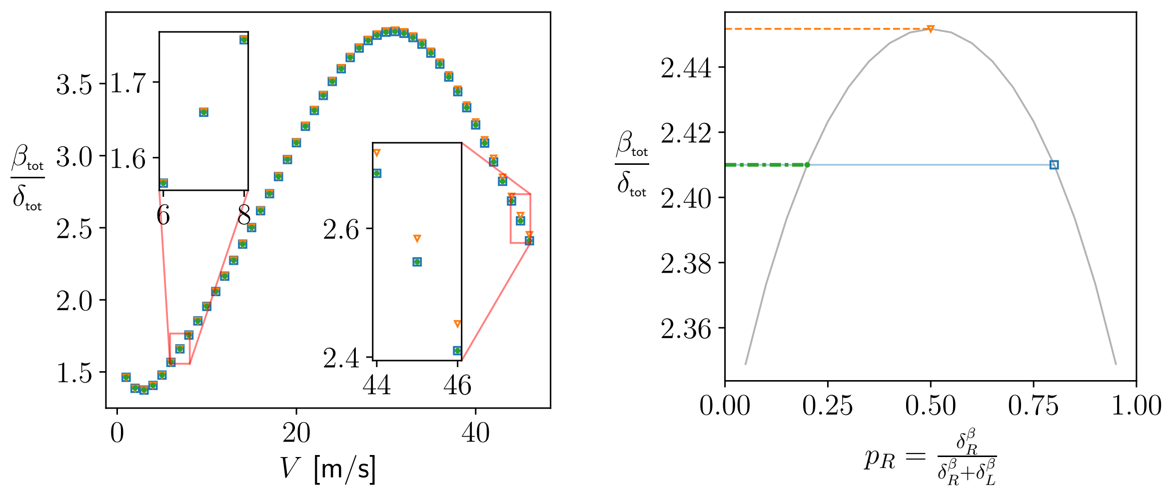

(a) (b)

Figure 13 – Diagram showing the ratio between total values against (a) airspeed, (square: $p_R = 0.8$; triangle: $p_R = 0.5$; circle: $p_R = 0.2$) and (b) against asymmetric freeplay with total gap 1° ($V = 46$ m/s).

3.2.3 Influence of Friction on the LCOs

The typical section $\mathcal{A}_1$ is considered with a symmetric freeplay $\delta^\beta = \delta_L = \delta_R = 0.5°$ and friction in the control surface rotation (β). Figure 14 shows the diagram of the LCO inversion points against airspeed, with square indicating the no friction case and the others representing four different levels of friction. For the most range of airspeed, this particular system presents mainly the fundamental harmonic, see for example the left column of plots in Fig. 15 where the time response, phase portrait and spectral content for $V = 20$ m/s are shown. Regarding LCO amplitudes, the general behavior indicated by the diagram in Fig. 14 is that the effect of friction is conventional: higher levels of friction imply smaller LCO amplitudes and frequencies with similar spectral content. On the other hand, for a large velocity $V = 46$ m/s, the two highest friction levels show a different spectrum content of LCO where high order harmonics appear - see Fig. 15 (right-hand side). The frequency axis is normalized by the fundamental frequency f_1 of each LCO in a way that the solution for $C = 5.00\ 10^{-3}$ Nm /m includes the third harmonic, and the solution for $C = 3.75\ 10^{-3}$ Nm /m includes the second, fifth and sixth harmonics.

The right-hand side diagram in Fig. 16 considers the friction coefficient as the parameter, and it confirms the effect of friction on the LCO amplitudes (right-hand side). Regarding the effect on the LCO frequency, both right-hand sides of diagrams against airspeed and against friction level, respectively, in Fig. 14 and 16, show that increasing the friction level, the LCO frequencies present a small decreasing, similarly to the effect of a structural damping $\hat{d}_\beta$ acting on the resonance frequency. In this sense, it is possible to write the friction coefficient C in terms of an equivalent damping ratio $\xi_{eq} = \hat{d}_\beta/(4I_\beta\pi f_1)$ to evaluate its magnitude. This equivalent structural damping $\hat{d}_\beta$ is introduced in chapter 4 including the friction and the freeplay effect (note Eq. (20) to see the dependence on frition level, LCO frequency and amplitude). Figure 17 shows that the magnitude of ξ_{eq} is higher for higher levels of friction. The results show that $C = 5\ 10^{-3}$ [Nm/m] represents an energy dissipation equivalent to less than 1.5% of an linear equivalent damping ratio if $V = 10$ m/s. On the other hand, this friction amount indicates higher linear equivalent damping ratio if $V = 20$ m/s.

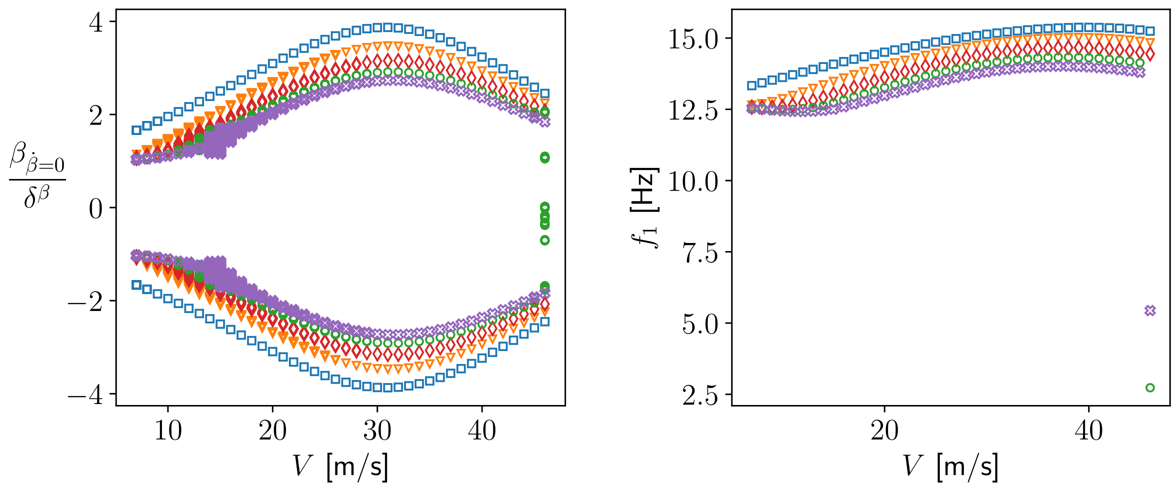

Figure 14 – Diagram of LCO amplitudes against airspeed, inversion points (left) and fundamental frequency (right) for different values of friction No friction (□); C = 1.25 10^{-3} Nm /m (▽); C = 2.50 10^{-3} Nm /m (◊); C = 3.75 10^{-3} Nm /m (○); C = 5.00 10^{-3} Nm /m (✖).

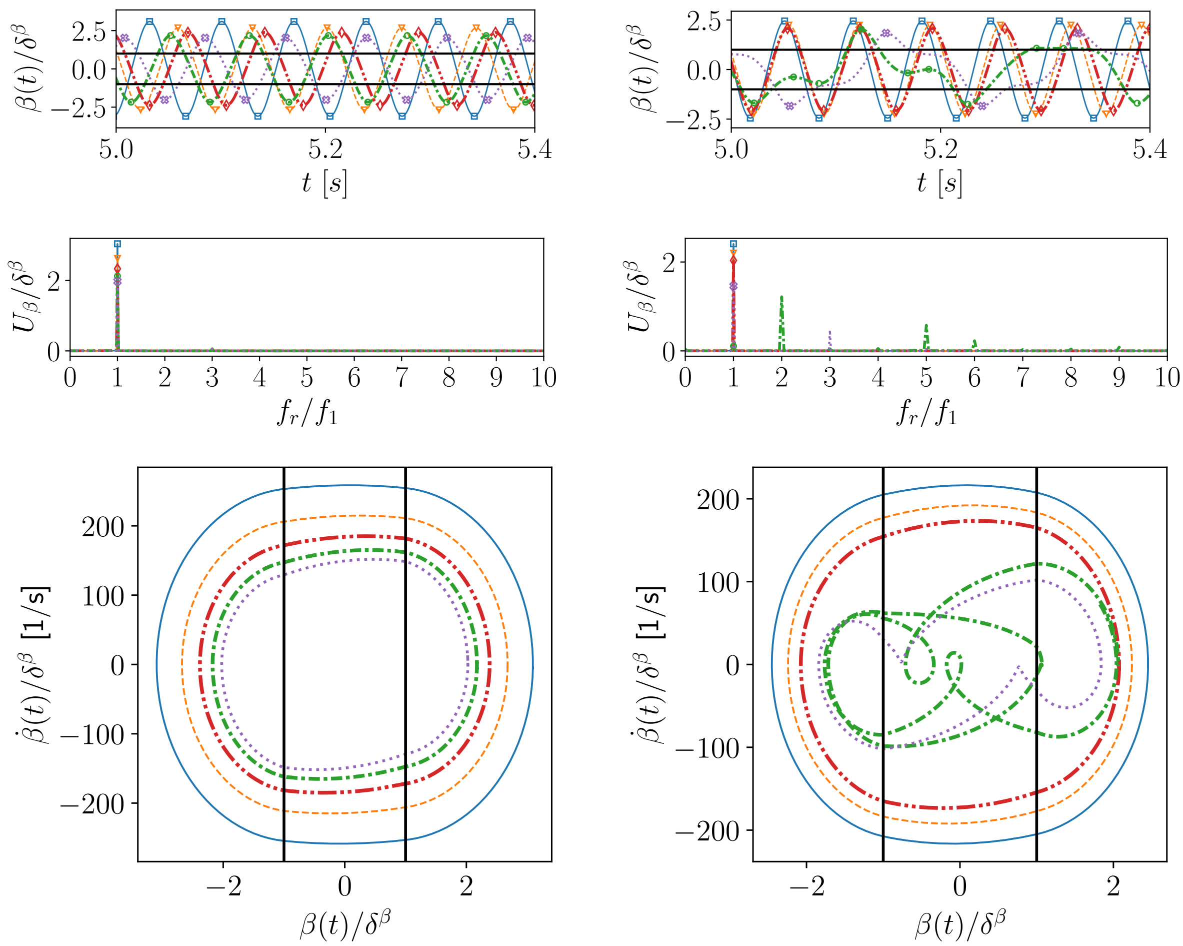

Figure 15 – Time response, portrait and spectrum for V = 20 m/s (left) and V = 46 m/s (right). No friction (□, ——); C = 1.25 10^{-3} Nm /m (▽, - - -); C = 2.50 10^{-3} Nm /m (◊, -··-); C = 3.75 10^{-3} Nm /m (○, -·-·); C = 5.00 10^{-3} Nm /m (✖, ·····) .

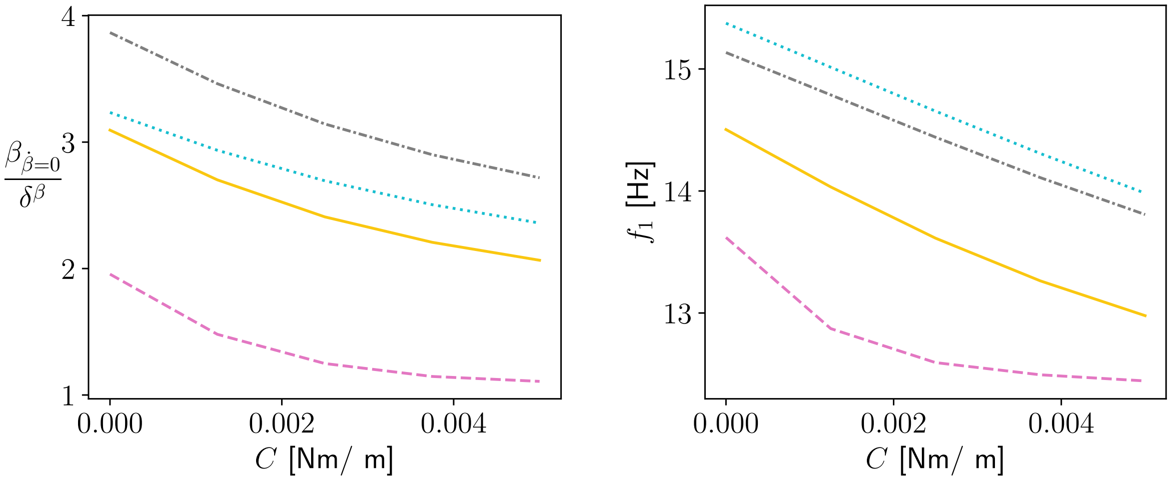

Figure 16 – Diagram of LCO amplitudes against friction force, inversion points (left) and fundamental frequency (right) for different values of airspeed. V = 10 m/s (dashed); V = 20 m/s (solid); V = 30 m/s (dash-dot); V = 40 m/s (dotted).

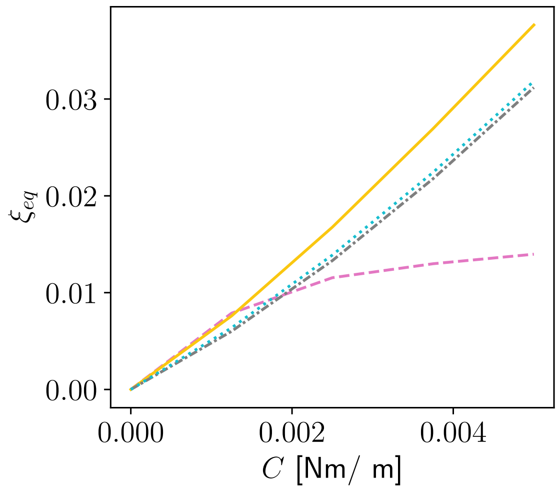

Figure 17 – Fiction coefficient described in terms of an equivalent linear damping ratio ξ_{eq}. V = 10 m/s (dashed); V = 20 m/s (solid); V = 30 m/s (dash-dot); V = 40 m/s (dotted).

3.3 General Procedure to Identify LCO and Generate Bifurcation Diagrams

A limit cycle oscillation can be described as a closed trajectory in phase space, however, with no other closed trajectories in its neighborhood. It means that around a limit cycle, a trajectory spirals either towards (stable) or away from the limit cycle (unstable) (NAYFEH; MOOK, 1979). Being a closed trajectory, a limit cycle is periodic. Therefore, a time long enough of the numerical integration needs to be considered to assure that the transient response is left behind and the LCO is reached. However, when several flight conditions and different values of nonlinearity coefficients are of interest, the solution can become a long process. In this context, Arévalo, Garía-Fogeda and Climent (2010) present the idea of motion detector to be used during the time integration, avoiding wasting time when integrating a decay or flutter solution, or even a clearly identified LCO. Basically, the Hénon's technique is employed as an event location method to compute the state vector at every time the nonlinear DOF has its motion inverted, i.e., reaches an extreme $\dot{u}_l = 0$. These extremes can be used to identify periodic motion and when a certain amount of repetition is reached, the LCO is identified.

Hénon's Technique to Locate Extremes

For aeroelastic systems with freeplay, the literature shows the Hénon's technique successfully used to properly compute the state vector in the switching points of freeplay, i.e, locate the points when $u_l = \delta_R$ and $u_l - \delta_L$. In this case, the motivation for locating these points is to change the equation of motion in a proper time since the freeplay is a discontinuous nonlinearity. Following this motivation, this technique is successfully applied for the nonlinearity Coulomb friction, for which the discontinuity occurs at $\dot{u}_l = 0$. However, the essence of the Hénon's technique is to compute the state vector in a pre-defined event. In practice, defining a value of interest for a particular state to reach (the event), this technique can be employed to compute the state vector when the event happens. In this sense, this work proposes to use the Hénon's technique as an event locator of extremes of the state u_l, i.e., the event to be located is $\dot{u}_l = 0$ ($x_k = 0$). In practice, the application in the algorithm is similar to that procedure performed for friction, since the event to be detected is the same. However, in this case there is no need to change any equation.

LCO Detection

Using of the Hénon's technique to compute the extremes of the degree of freedom with freeplay, every extreme of u_l is kept in a vector during the integration (including all local maximum and minimum). Regarding computational algorithms, Arévalo, Garía-Fogeda and Climent (2010) propose creating a vector package E_j with 50 consecutive extremes of u_l. When the vector E_j is full, a new vector package E_{j+1} is constructed with the next 50 consecutive extremes. The LCO detector D_{LCO} can be defined as

$$D_{LCO} = \sum_{i=1}^{50} \sqrt{(E_j^{(i)} - E_{j+1}^{(i)})^2}$$
$$\textbf{Identical packages } E_j^{(i)} \textbf{ and } E_{j+1}^{(i)}\textbf{:}\ D_{LCO} < \epsilon_{LCO} \tag{15}$$

where $E_j^{(i)}$ is the i-th element of the j-th package. ϵ_{LCO} is a user-defined tolerance to indicate the condition for two consecutive packages to be identical[I]. Finally, if 4 consecutive identical packages are identified, then the LCO is considered reached and the time integration can be interrupted.

Note that Arévalo, Garía-Fogeda and Climent (2010) suggest that each package E_j needs to have 50 points, although it is valid to highlight that this number actually has to be a multiple of the number of extremes present in a single period, otherwise, Eq. (15) does not result in two identical packages when comparing E_j and E_{j+1}.

Bifurcation Diagrams Construction with Time Domain Simulations

According to Dimitriadis (2017b), bifurcation analysis is the study of how the nature of a system solution changes when a parameter is varied. In practice, a parameter of interest is changed and for each value the solution of the system can be compute and several information can be extracted to be plotted against that parameter. In a more rigorous definition from nonlinear dynamics, a bifurcation point is the particular value of the parameter where the change of solution nature occurs, for example changing from quasi-periodic solutions, to LCO, or even to chaos (KUZNETSOV, 1998). In aeroelastic problems, the flight condition is typically varied in terms of air density or airspeed and this work presents several bifurcation diagrams where the airspeed is changed. In this chapter, for example, besides varying the airspeed, information as extremes of the nonlinear DOF and its fundamental frequency are plotted also against the freeplay parameter.

A range of a chosen parameter is defined to construct a bifurcation diagram, for example the airspeed $V_{min} < V < V_{max}$, and it is discretized in a limited number of points such that the $(i+1)$-th point is obtained in terms of the i-th and the step $\Delta V = V_{i+1} - V_i$. The solution for each point can be obtained by varying the parameter increasing $(V_{i+1} > V_i)$ or decreasing $(V_{i+1} < V_i)$. Supposing the current parameter V_i, the time marching solution can start with an user-defined initial condition $\mathbf{x}_i^0$ and a time long enough is defined to be the maximum. However, if the LCO detector in Eq. 15 identify a reached LCO, the time simulation for this parameter V_i is interrupted and the last state obtained $\mathbf{x}_i^{end}$ is part of

[I] Arévalo, Garía-Fogeda and Climent (2010) define $\epsilon_{LCO} = 1.10^{-10}$.

this steady reached solution. The time marching for the next parameter V_{i+1} starts with initial condition defined by the last state of the previous parameter, i.e., $\mathbf{x}_{i+1}^{0} = \mathbf{x}_{i}^{end}$. This approach to define the initial condition usually makes the convergence to the LCO faster than coming from an arbitrary initial condition. Also, if more than one LCO exist for the same parameter, the initial condition is determinant to define which LCO is reached. In this way, this strategy also offers the advantage that if it is achieved for V_i, the same type of LCO is also achieved for V_{i+1} (if it exists). Therefore, note that if a different way of varying the chosen parameter (increasing or decreasing it) results in different branches, then there is hysteresis.

3.4 Final Remarks

Time simulations confirm that limit cycle oscillations in aeroelastic systems can occur due to freeplay nonlinearities. The Hénon's technique is employed for both nonlinearities freeplay and friction. This approach is a classical strategy of changing the independent variable from the time to the displacement mainly when considering freeplay. On the other hand, the approach is extended and applied to the discontinuous friction, i.e., the independent variable is the control surface velocity to consider the friction effect. If it is applied only to the freeplay, and the friction force is also considered during the integration process, the level of numerical errors is higher than those levels obtained if the method is employed for both nonlinearities. Similarly, the errors do not achieve the smallest level if this method is applied only to the friction while freeplay is also considered. This behavior can also be demonstrated for a one-degree-of-freedom spring mass system, comparing with its exact analytic solution, although it is omitted from this thesis.

Different works in the literature have considered the Hénon's method. However, the present work introduced a simpler mathematical notation for describing it. A general and compact notation was introduced to simplify the computational implementation focused on discontinuous nonlinearities. In addition, a very convenient new coordinate system is employed if the generalized coordinate system is required. Using this new coordinate the displacement vector contains the generalized coordinates and the physical displacement related to the nonlinear efforts. This strategy provides a practical and useful state space equation of motion.

The results presented herein show that a Coulomb friction force can reduce the frequency of LCO, but with slight differences in relation to the no friction condition. Also, describing the friction level as a typical linear damping ratio (until ~ 4%), this force is not enough to suppress the limit cycle, although its dissipative nature. On the other hand, the level of friction may modify the spectrum of the system response, introducing different harmonics. Also, the results show that the amplitude of a LCO can be changed depending on the level of the freeplay asymmetry. This is an important aspect to be considered because a freeplay amplitude can change during the aircraft operation.

Finally, the Hénon's technique is proposed herein to be used as an event locator allowing one to compute the extremes of a degree of freedom, which is useful to properly detect a reached LCO usually faster than simply running the time marching for a time long enough.

4 A new look at the Equivalent Linearization Technique: new Describing Functions

Several methods have been proposed to predict LCO, such as Harmonic Balance-based methods (HB). Describing function (DF) is the HB with a single harmonic motion assumed, and the approach can be combined with a classic eigenvalue stability analysis via the Equivalent Linearization Technique (ELT). On the other hand, High-Order Harmonic Balance (HOHB) methods consider higher number of harmonics, but they commonly lead to a more complex nonlinear algebraic system of equations. This chapter introduces a new look at the ELT combining both eigenvalue analysis and describing functions involving two complementary applications.

The first application employs a new describing function to predict limit cycle oscillations considering the first and third harmonics of motion. The proposal replaces the solution of a classic describing function by a nonlinear system of equations involving four unknown parameters. The second application considers a new iterative approach involving the ELT to predict amplitude and frequency of LCO in aeroelastic systems with both freeplay and friction acting simultaneously. The method uses a new describing function, representing the effect of friction force proportional to the velocity, and written in terms of a linear equivalent viscous damping. Time domain simulations improved with the Hénon's technique as described in chapter 3 are considered as reference results to demonstrate the approaches proposed herein.

4.1 Harmonic Balance Fundamentals

The main idea of the Harmonic Balance method is employed when using either DF or HOHB. The main difference between them is the procedure performed after the harmonic balance, as described in sections 4.1.1 and 4.1.2. For the freeplay case, the central premise assumed by the harmonic balance is to write a linear equivalent torque $\hat{f}_l^{\delta} = \hat{k}_{u_l}\hat{u}_l(t)$

to describe its corresponding nonlinear, where $\hat{(.)}$ indicates the linear equivalent term associated to the exact $(.)$. Figure 18 shows the steps considered to address this premise: *i.* choose a mathematical expression $\hat{u}_l$ composed by harmonic functions (sine and/or cosine) to properly describe the system response, i.e., the expected LCO (right-hand side of the upper equation in Fig. 18); *ii.* choose which harmonics are used to compose $\hat{f}_l^\delta$ by using the Fourier series $(\frac{F_0}{2} + \sum F_{c_n} \cos n\theta + F_{s_n} \sin n\theta)$ to express the nonlinear effort f_l^δ (left-hand side of the upper equation in Fig. 18).

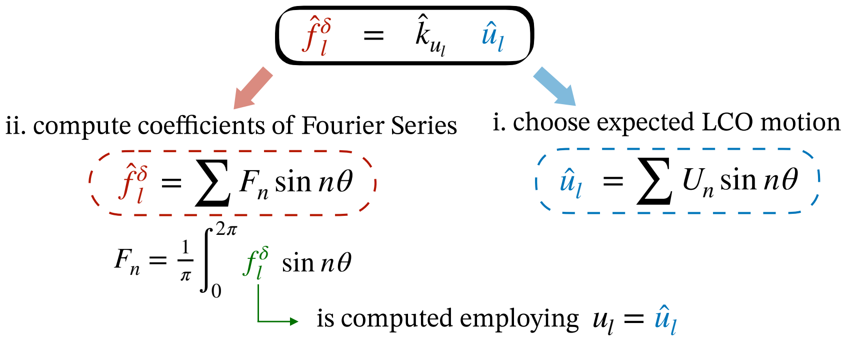

Figure 18 – Central premise with the two steps (*i.* and *ii.*) required to derive the linear equivalent stiffness $\hat{k}_{u_l}$, for f_l^δ presented in Eq. (1).

Due to the discontinuous behavior of the freeplay representation, the integral limits need to be defined to compute the coefficients $F_n \equiv F_{s_n}$ of the Fourier series ($F_0 = F_{c_n} = 0$ for all $n \geq 1$, because this nonlinear effort is an odd function) - see the lower equation in Fig. 18. These limits are well-known in terms of u_l, as shown in Eq. (1) (i.e., $u_l = \pm\delta$). However, they must be known in terms of the reduced time $\theta = \omega_{u_l} t$ over a complete period of oscillation, where ω_{u_l} is the LCO frequency of the first (fundamental) harmonic. Then, the unknown parameters θ_δ are introduced, and they represent the values of θ for which there are transitions among the locally linear models (since this nonlinear effort is piecewise linear). In practice, these limits correspond to $\hat{u}_l = \delta$. Note that the number of unknown parameters θ_δ depends on the type of motion assumed for $\hat{u}_l$ since it is directly related to the number of transitions through the freeplay boundaries in a single cycle.

4.1.1 Considerations on the HOHB Methods in the Context of Describing Functions

HOHB methods allow one to define which harmonics are present on motion $\hat{u}_l$ considering LCO with multiple harmonics. They also provide the amplitude of motion for all degrees of freedom (DOF), instead of computing it for the nonlinear DOF only, because they consider harmonic motions in the form such as $\hat{\mathbf{q}} = \frac{\mathbf{q}_0}{2} + \sum \mathbf{q}_{c_n} \cos n\theta + \mathbf{q}_{s_n} \sin n\theta$, such that $\mathbf{q}_{c_n}$ and $\mathbf{q}_{s_n}$ are amplitude vectors containing all the degrees of freedom, including the aerodynamic ones (see Liu and Dowell (2005) for details). The general procedure of HOHB methods does not consider the equivalent stiffness and the bottom line is that all assumed displacements ($\hat{\mathbf{q}} = \{\hat{h},\ \hat{\alpha}...\}^T$) are directly included in the system of ordinary differential equations. Similar procedure is used for the velocities, accelerations and the linear equivalent force $\hat{f}_l^\delta$ computed as Fourier series. In particular for the typical section with control surface freeplay, one of these equations is $S_\beta\ddot{\hat{h}}+[I_\beta+b(c-a)S_\beta]\ddot{\hat{\alpha}}+I_\beta\ddot{\hat{\beta}}+\hat{f}_\beta^\delta = M_\beta$. Hence, a typically nonlinear algebraic system of equations is obtained with a large number of unknown parameters, i.e., the coefficients assumed for the motions of all DOFs, the unknown parameters θ_δ, and also the LCO frequency ω_{u_l} of the first harmonic. Note that the main advantages of a HOHB method is to admit multiple harmonics, but they can involve much more complex solutions for the system of equations in comparison with a describing function (DIMITRIADIS, 2008b).

4.1.2 Conventional Describing Function (DF) for freeplay

The conventional Describing Function (DF) is a particular case of the idea presented about the harmonic balance fundamentals, and it is derived by assuming a LCO with a single harmonic (i.e., $\hat{u}_l = U_1 \sin\theta$) and also truncating the Fourier series with only one harmonic (i.e., $\hat{f}_l^\delta = F_1 \sin\theta$). Applying the harmonic balance, $\hat{k}_{u_l} = F_1/U_1$ can be obtained, where U_1 is the LCO amplitude (see the appendix C for the computation of $F_1 \equiv F_{s_1}$). The final DF relates the linear equivalent stiffness and the LCO amplitude, and its expression is given by (KHOLODAR; DICKINSON, 2010)

$$\hat{k}_{u_l} = \frac{k_{u_l}}{\pi}\left[\pi - 2\theta_\delta - \sin(2\theta_\delta)\right] \tag{16}$$

where $\theta_\delta = \arcsin(\delta/U_1)$.

The special feature of this approach in comparison with a HOHB is that a classic stability analysis (i.e., eigenvalue extractions) is performed to identify each value of stiffness (in the range $0 < \hat{k}_{u_l} < k_{u_l}$) that implies to eigenvalues with null real parts (marginally stable conditions). Each corresponding stiffness is associated with an equivalent linear system represented by the matrix $\hat{\mathbf{A}}$ (see Appendix A), and the possible LCO has its amplitude given by DF, whereas the frequency is determined from the imaginary part of the eigenvalue presenting zero real part. This procedure where a linear equivalent system is created corresponds to the Equivalent Linearization Technique (ELT). The main advantages of this approach are to obtain the LCO frequency from a classic eigenvalue analysis (Fig. 19a) and to compute the LCO amplitude by using a scalar describing function (Fig. 19b). Note that the shape of the curve shown in Fig. 19b is the same for any system because it is presented in the non-dimensional range $0 < p < 1$ for $p = \hat{k}_{u_l}/k_{u_l}$ and $\bar{U}_1 = U_1/\delta$. Figure 19a illustrates that for each discrete value of equivalent stiffness pre-assumed from such range, the eigenvalues λ of matrix $\hat{\mathbf{A}}(V, \hat{k}_{u_l})$ are extracted for the airspeed range of interest, and the marginally stable conditions indicated by the circles are kept as possible LCO conditions for such particular equivalent stiffness. Each corresponding point for $\mathrm{g} = 0$ is identified by using the mode tracking, which allows one to more accurately predict the marginally stable condition. Note that it can be done through the modal assurance criteria considered by Bueno and Dowell (2021).

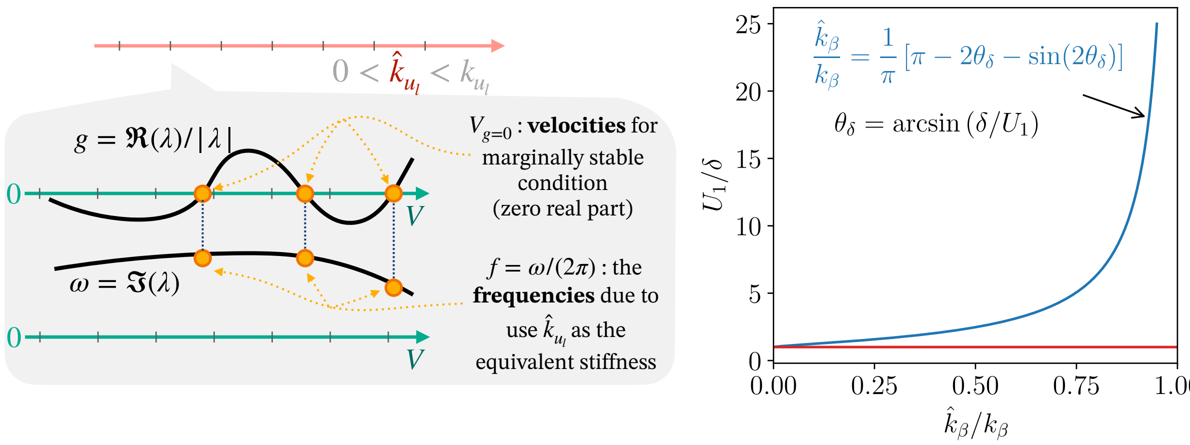

(a) (b)

Figure 19 – Scheme of the complete procedure of Describing Function method: a) classic eigenvalue analysis for a particular linear system (hypothetical behaviors are shown for g and ω versus V to illustrate the procedure); b) scalar expression for the freeplay DF and the curve shape relating the linear stiffness and the LCO amplitude. The red horizontal line is in $U_1/\delta = 1$.

An important note about the DF expression refers to the limits of the linear equivalent stiffness range $0 < p < 1$ for $p = \hat{k}_{u_l}/k_{u_l}$. The lower limit $\hat{k}_{u_l} = 0$ refers to the actual linear system inside the freeplay, and corresponds to motion amplitudes precisely at the freeplay boundary, specifically $U_1 = \delta$ (check Eq. 16), which is the minimum amplitude for which the expression is mathematically valid (red horizontal line in Fig. 19b). Consequently, when the airspeed falls below the threshold of the first marginally stable condition for the system inside the freeplay, any motion starting from an initial condition inside the freeplay gradually decays over time. When the airspeed precisely matches this particular value, the oscillations are purely linear and maintain a constant amplitude exactly at the freeplay boundary. Moving beyond this point to a slightly higher airspeed, usually an unstable LCO with amplitude close to the freeplay boundary coexists with a stable

LCO with a larger amplitude. On the other hand, the upper limit $\hat{k}_{u_l} = k_{u_l}$ refers to the actual linear system outside the freeplay, i.e., the system without freeplay ($\delta \rightarrow 0$). In this scenario, the first marginally stable condition corresponds to the flutter airspeed (V_F) of the linear system, beyond which the oscillations no longer fall under the category of LCOs but instead exhibit growing amplitudes, signifying the onset of flutter instability.

The airfoil $\mathcal{A}_1$ presenting only a single dominant harmonic is used to show an application of the DF method (see the Table 2 in chapter 2 for the parameters). Figure 20 presents the results obtained from the eigenvalue analysis, according to the scheme of Fig. 19a, where the V-g-f diagrams for $\hat{k}_\beta = 0$ (bottom) and $\hat{k}_\beta = k_\beta$ (top) are highlighted. Based on these diagrams, the airspeed and LCO frequency can be related to the LCO amplitude provided by DF (Fig. 19b) for each linear equivalent stiffness, and the LCO is characterized. Figure 21 shows the classic results from the literature in which the DF method provides LCO predictions in good agreement with the time simulations - which use the Hénon technique as presented in chapter 3.

The LCO amplitude and the equivalent stiffness define a pair for which each solution is computed. Then, an additional computational effort is required in comparison with a nominal flutter analysis. Although repetitive, it is equivalent to a typical parametric analysis in terms of stiffness - see Bueno, Góes and Gonçalves (2015) for complementary information. Also, note that this approach can be employed to investigate multiple DOF aeroelastic systems, such as previously demonstrated for other DF-based methods in the literature - see Kholodar and Dickinson (2010), and Anderson and Mortara (2007), respectively.

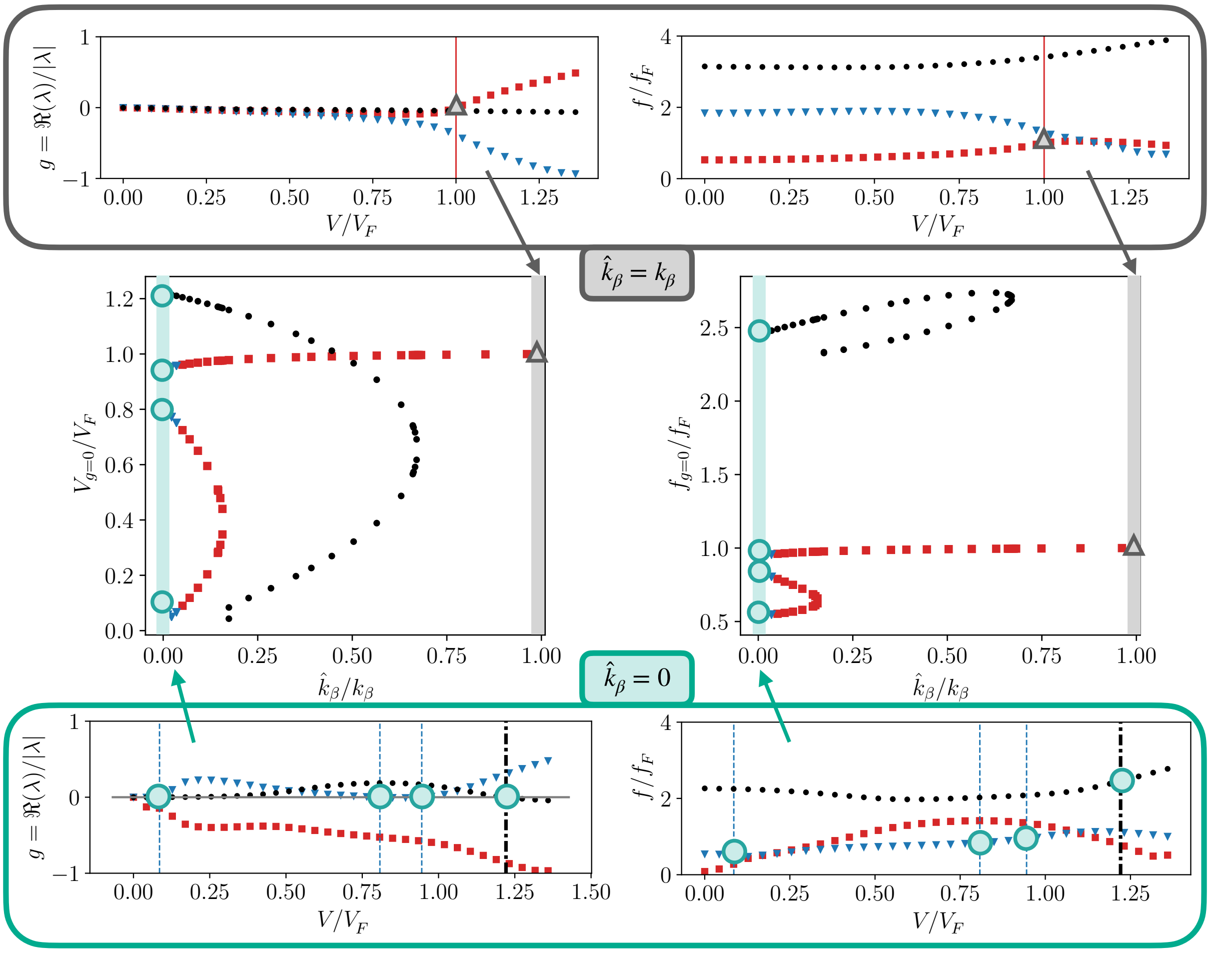

Figure 20 – Results of the ELT for the complete range of $0 < p < 1$ for $p = \hat{k}_\beta/k_\beta$, highlighting the V-g-f diagrams for $\hat{k}_\beta = 0$ (bottom) and $\hat{k}_\beta = k_\beta$ (top). System $\mathcal{A}_1$: $V_F = 47.09$ m/s and $f_F = 5.62$ Hz.

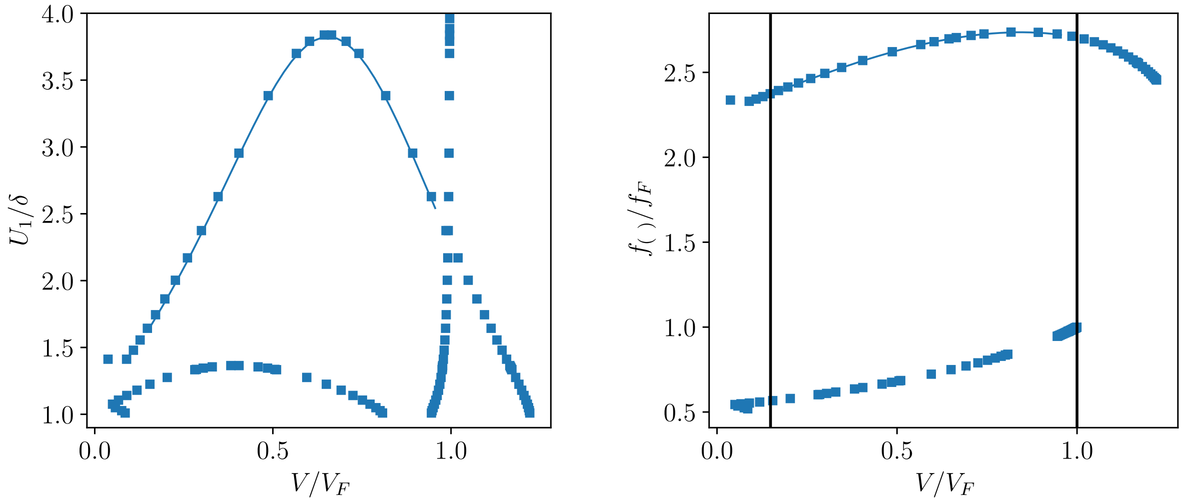

Figure 21 – Prediction of amplitude U_1 and frequency of all possible LCO conditions via DF, for $\mathcal{A}_1$. Symbols for DF (▪) and solid line for time integration (Runge-Kutta with Hénon's Technique) as reference.

4.2 New Describing Functions for ELT

The main focus of a typical LCO prediction is to determine both LCO amplitude and frequency for each flight condition in which the phenomenon occurs. The classic linear stability analysis involving an eigenvalue problem consists in extracting the eigenvalues λ of the dynamic matrix $\mathbf{A}$ for each i-th flight condition ($V_i = V_{sea}\sqrt{\rho_i/\rho_{sea}}$, $i = 1, ...$) and evaluate the sign of their real part $\Re(\lambda)/|\lambda| \equiv g$, where (V_{sea}, ρ_{sea}) are the airspeed and air density at sea level. Section 4.1.2 introduces how the conventional DF method employs the ELT by creating a linear equivalent stiffness that allows the classic linear stability analysis to be used.

In the context of LCO prediction, fundamentals of the ELT are applied in the sense that a linear equivalent system is considered and it is related to the velocity and frequency pairs corresponding to null real parts of eigenvalues obtained via classic linear stability analysis (association $I.$). On the other hand, the equivalent linear system is also related to the LCO amplitude (association $II.$). By changing some of these associations it is possible to introduce a new way of looking at ELT. Table 3 shows a schematic illustration of the methods employed in the conventional DF method, and the approach for two new introduced applications. The first application considers the first and third harmonics for system with freeplay and it corresponds to changing the association $II.$ by introducing a new type of DF. The second application considers both freeplay and friction nonlinearities to predict LCO with the first harmonic only and it corresponds to modifying the procedure involving the eigenvalue analysis, i.e., by changing the association $I.$

Method	Velocity frequency $\xleftarrow{I.}$ $\boxed{\hat{k}_{u_l}}$	$\xrightarrow{II.}$ Amplitude
classic DF	classic eigenvalue analysis (Fig. 19a	freeplay DF expression (Fig. 19b and Eq. 16)
HB3-ELT	classic eigenvalue analysis (Fig. 19a	▸ algebraic system to be solved for the assumed amplitudes U_1, U_3 (Eq. 17) ◂
Iterative-ELT	▸ iterative eigenvalue analysis (Fig. 25) using friction DF expression (Eq. 20) ◂	freeplay DF expression (Fig. 19b and Eq. 16)

Table 3 – ELT-based approaches to relate the linear equivalent system (by means of the linear equivalent stiffness $\hat{k}_{u_l}$) to the velocity and frequency pairs of the marginally stable conditions (association $I.$) and also to the LCO amplitude (association $II.$). The symbols ▸(.)◂ indicate new procedures proposed in this work.

4.2.1 Application I: Predict LCO with higher harmonics in systems with freeplay

The HOHB typically employed in the literature is based on the HB method instead of using the ELT, and it involves a nonlinear algebraic system of equations instead of an eigenvalue problem. This characteristic can require a complex algorithm to solve the resulting system, since the LCO frequency is one of the unknown parameters in the trigonometric functions (LIU; DOWELL, 2005). Thus, this section introduces an alternative approach which combines the main features from the classic DF and the ELT methods with eigenvalue analysis. The new approach is named HB3-ELT because the harmonic balance considers the third harmonic in the LCO using a novel Equivalent Linearization Technique. The central idea is to employ the eigenvalue analysis combined with a system of equations obtained after considering two terms of the Fourier series to represent the aeroelastic response of the system with freeplay.

The approach modifies the association $II.$ in Tab. 3 by assuming a LCO with both the first and third harmonics, i.e., defining oscillations such as illustrated in Fig. 22 ($\hat{u}_l = U_1 \sin\theta + U_3 \sin 3\theta$). Based on the harmonic balance premise presented in Fig. 18, the following linear system $\mathbf{F}(\mathbf{z}) = \mathbf{0}$ is written, such that

$$\left\{ \begin{array}{c} U_1\hat{k}_{u_l} - F_1 \\ U_3\hat{k}_{u_l} - F_3 \end{array} \right\} = \mathbf{0} \xrightarrow{\div(k_{u_l}\delta)} \mathbf{F}(\mathbf{z}) = \left\{ \begin{array}{c} \bar{U}_1 p - \bar{F}_1 \\ \bar{U}_3 p - \bar{F}_3 \end{array} \right\} \tag{17}$$

where the vector of unknown parameters is given by $\mathbf{z} = \{\bar{U}_1 \ \ \bar{U}_3\}^T$, for $\bar{U}_n = U_n/\delta$.

Note that the non-dimensional Fourier series coefficients $\bar{F}_1$ and $\bar{F}_3$ depend on $\bar{U}_1$, $\bar{U}_3$, $\theta_{\delta 1}$ and $\theta_{\delta 2}$ (see appendix C, Eqs. 47 and 48) and in this algebraic system, p is a parameter that assumes known discrete values in the pre-defined range $0 \leq p \leq 1$. In addition, note that the curve shape of the assumed LCO has direct influence on the integration limits to compute the Fourier coefficients F_n (see Tab. 8), and therefore it directly affects the final algebraic system. This particular shape is identified as a typical behavior according to the previous study which investigated this nonlinearity by solving the nonlinear system in the time domain (WAYHS-LOPES; DOWELL; BUENO, 2020).

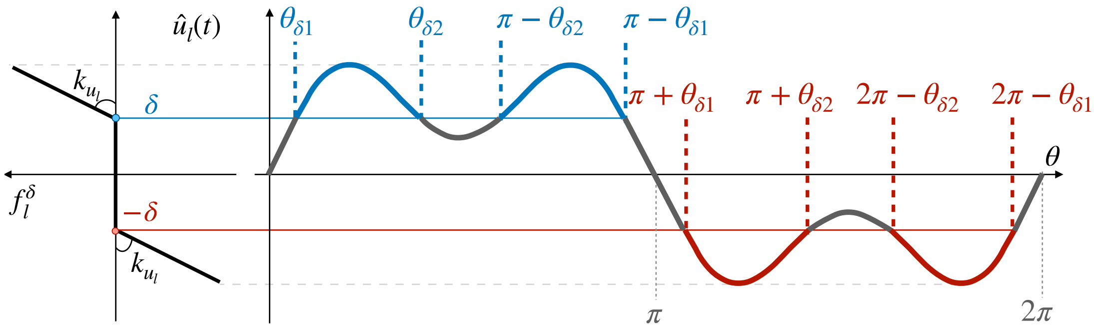

Figure 22 – Schematic illustration of one cycle of LCO assuming $\hat{u}_l = U_1 \sin\theta + U_3 \sin 3\theta$ for freeplay nonlinearity.

The non-dimensional linear equivalent stiffness $p = \hat{k}_{u_l}/k_{u_l}$, $0 \leq p \leq 1$, is used in the ELT when extracting the eigenvalues through a procedure similar to that one performed when using classic DF (association *I.*). However, it is assumed that $\hat{u}_l = U_1 \sin\theta + U_3 \sin 3\theta$, instead of $U_1 \sin\theta$. Hence, it is convenient to assume only two terms to represent f_l^δ by the Fourier series ($f_l^\delta = F_1 \sin\theta + F_3 \sin 3\theta$), otherwise, it is not possible to directly compare the coefficients of the corresponding harmonics to define the algebraic system of equations (following the harmonic balance of Fig. 18). On the other hand, this consideration imposes the spectral content of the nonlinear restoring torque to be equivalent to that of the LCO, which may not be necessarily physically consistent for all practical applications. However, this approach provides good estimates of the third harmonic LCO amplitude without requiring a more complex solution typically involved in HOHB methods.

Solution procedure of the algebraic system

Note that the values of θ_{δ_1} and θ_{δ_2} are also unknown, but they can be computed given the values of $\bar{U}_1$ and $\bar{U}_3$. They represent the values of a non-dimensional time when freeplay boundary is crossed, then the equations to be solved are

$$\begin{cases} -1 + \bar{U}_1 \sin\theta_{\delta_1} + \bar{U}_3 \sin 3\theta_{\delta_1} = 0 \\ -1 + \bar{U}_1 \sin\theta_{\delta_2} + \bar{U}_3 \sin 3\theta_{\delta_2} = 0 \end{cases} \tag{18}$$

Note that the Newton-Raphson method for scalar equations can be applied, and it provides a good solution mainly if a good initial guess is chosen. The left-hand side of these equations can be evaluated employing a range of θ from 0 to 2π. Then, the value of θ resulting in the minimum difference compared to the right-hand side (i.e., 0) is a guess good enough to guarantee the convergence of Newton-Raphson.

The system in Eq. (17) is solved here with the simplest Numerical Continuation (DIMITRIADIS, 2017a) for the parameter p, where the solver used is the Newton-Raphson. The subscript j is used to refer to the j-th value of p in a predefined range $0 < p < 1$. The subscript k indicates the k-th iteration of $\mathbf{z}$ during the Newton-Raphson convergence procedure for each particular p_j. A first guess ($k = 0$) needs to be chosen for the first value of p ($j = 0$), i.e., $\mathbf{z}_{0,0}$ is employed in the Newton-Raphson procedure in Eq. (19) until the convergence to the solution $\mathbf{z}_0$ referring to the parameter p_0. After that, the first guess of the next value of p is the converged one for the previous point, i.e., $\mathbf{z}_{j,0} = \mathbf{z}_{j-1}$.

$$\begin{aligned} \mathbf{z}_{j,k+1} &= \mathbf{z}_{j,k} + \delta\mathbf{z} \\ \delta\mathbf{z} &= -\left[\left.\frac{\partial \mathbf{F}}{\partial \mathbf{z}}\right|_{\mathbf{z}_{j,k},p_j} \right]^{-1} \mathbf{F}(\mathbf{z}_{j,k}, p_j) \end{aligned} \tag{19}$$

it stops when $\sqrt{\delta\mathbf{z}^T\delta\mathbf{z}} < \varepsilon$, for certain chosen tolerance ε (this work uses $\varepsilon = 10^{-10}$).

4.2.2 Application 2: Predict LCO in systems with freeplay and friction - an iterative approach

The Coulomb friction typically appears in hinge connections acting simultaneously with freeplay, and therefore it is another issue considered in this work. The friction force is also a non-smooth effect, as shown in illustrative representation in top-left in Fig. 23.This is the main reason to propose similar procedure of linearization employed to freeplay. Instead of a linear equivalent stiffness, the effect of nonlinear friction force f_l^C

(Eq. 2) is represented with an equivalent force proportional to the velocity of the control surface rotation, and it is done by creating a linear equivalent viscous damping such that $\hat{f}_l^C = \hat{d}_{u_l}\dot{\hat{u}}_l(t)$.

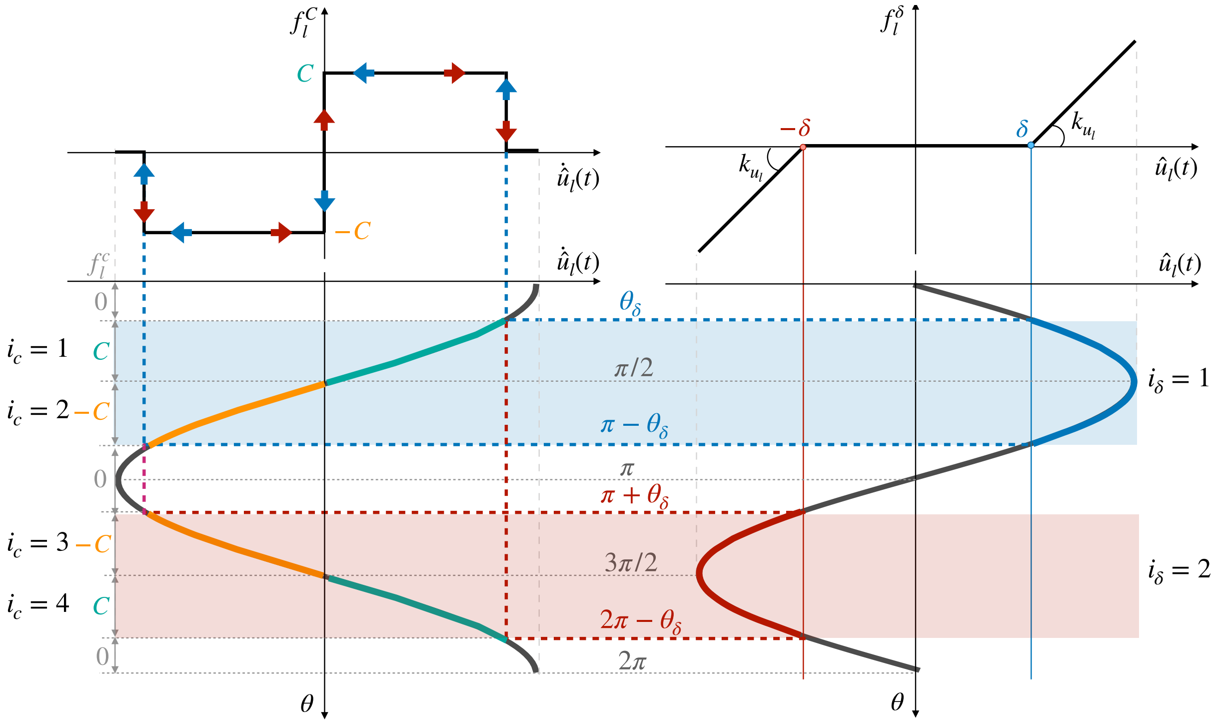

Figure 23 – Representation of non-smooth forces due to Coulomb friction (top-left) and freeplay (top-right) and schematic illustration of one cycle of LCO assuming $\hat{u}_l = U_1 \sin\theta$.

The friction torque is considered acting on the control surface and is included using an analogous procedure employed to the freeplay problem (see Fig. 18), considering Eq. (2) to be approximated by the Fourier series. In this work, a motion with a single harmonic is assumed ($\dot{\hat{u}}_l = \omega_{u_l} U_1 \cos\theta$) and, therefore, a Fourier series of first order is computed ($\hat{f}_l^C = F_{c_1}^C \cos\theta$). Solving for $\hat{d}_{u_l}$ by comparing the amplitudes of the first harmonic coefficients (i.e., performing the harmonic balance), it is obtained the equivalent linear viscous damping by $\hat{d}_{u_l} = F_{c_1}^C/(\omega_{u_l} U_1)$. This procedure is properly detailed in appendix C and it allows one to obtain the describing function equation, as shown in Eq. (20). Note that the friction DF shows the combined effect of both friction and freeplay, since the nonlinear torque due to friction is affected by the freeplay (there is no friction inner the freeplay region).

$$\hat{d}_{u_l} = \frac{4C}{\pi U_1 \omega_{u_l}}\left[1 - \frac{\delta}{U_1}\right] \tag{20}$$

There is an important challenge for applying the procedure of the ELT if freeplay and friction are simultaneously considered. Note that the DF for friction (see Eq. 20) to compute the equivalent damping depends on the oscillation frequency ω_{u_l}. On the other hand, the classic eigenvalue analysis employed in the ELT for that classic DF method considers the LCO frequency as an output once it is obtained from the eigenvalues of the dynamic matrix. The bottom of Fig. 24 illustrates this part of the procedure, in which hypothetical curves of g and ω are obtained from one eigenvalue extracted for each flight condition. Small circles are used to indicate the airspeeds for which the respective eigenvalue has zero real part ($g = 0$) and its associated imaginary part corresponds to the LCO frequency ω_{u_l}. The top-right corner of the Fig. 24 shows the equivalent matrix $\hat{\mathbf{A}}$ (represented by the larger square) and its associated equivalent damping $\hat{d}_{u_l}$. Different fillings are employed to indicate the submatrices influenced by each parameter (V, $\hat{k}_{u_l}$, $\hat{d}_{u_l}$) into the matrix. Finally, the top-left corner of Fig. 24 shows that the equivalent damping computation depends on LCO frequency ω_{u_l}. This schematic drawing presented in Fig. 24 illustrates the dependency cycle arisen among those three variables indicated in the figure, i.e., the frequency ω_{u_l} required to compute the equivalent damping $\hat{d}_{u_l}$ necessary to define the matrix $\hat{\mathbf{A}}$, from which the eigenvalue indicating the LCO frequency is extracted. This parameter-dependent problem is solved in the present article through the iterative method involving the eigenvalue analysis (changing the association I. in Tab. 3), as illustrated in Fig. 25.

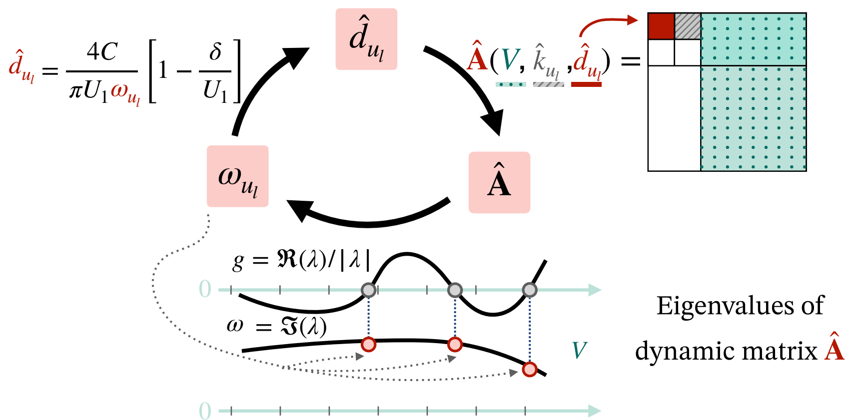

Figure 24 – Dependency cycle between equivalent damping, LCO frequency and equivalent dynamic matrix.

The proposed iterative approach requires that the airspeed range of interest to predict the LCO be defined. The range definition, such that $V_{sta} < V < V_{sto}$, includes choosing V_{sta}, V_{sto} and the incremental step ΔV, where the subscript $(\ )_{sta}$ indicates the airspeed to start the procedure and $(\ )_{sto}$ represents the maximum value to be assumed by an arbitrary V. In practice, for a pair of freeplay δ and friction C nonlinearities, for each j-th equivalent stiffness in the range $0 < \hat{k}_{u_l} < k_{u_l}$, the following sequence is employed:

1. Use δ, the current $\hat{k}_{u_l}$ and k_{u_l} to compute U_1 via the freeplay DF (Eq. 16);
2. Set $V_0 = V_{sta}$;
3. Choose an initial guess ω^0 for the frequency in rad/s. A good guess is the frequency obtained for the ELT for the system with a close value of friction or with only freeplay for the current equivalent stiffness $\hat{k}_{u_l}$;
4. Set $\omega_{u_l} = \omega^0$;
5. Use δ, C, U_1 (from step 1) and ω_{u_l} to compute $\hat{d}_{u_l}$ via Eq. (20);
6. Start the loop in airspeed with V_i, by setting $i = 0$ to run the linear stability analysis for a speed range starting in V_0;
7. Use the current $\hat{k}_{u_l}$, $\hat{d}_{u_l}$ from step 5, and V_i to compute the linear equivalent dynamic matrix $\hat{\mathbf{A}}$ (see Appendix A) and extract their eigenvalues.
8. Check if the real part of any eigenvalue crosses the zero axis, i.e., check if $g_{i-1}g_i < 0$ is satisfied.
   - if yes: properly locate $V_{g=0}$ and $f_{g=0}$, and the airspeed loop is suspended in the i-th airspeed. Go to step 9.
   - if not: increment i to increase V in an amount ΔV. Check if the new $V_i > V_{sto}$.
     - if yes: increment $\hat{k}_{u_l}$, and go back to step 1. It means that all the speed range from V_{sta} to V_{sto} is already covered for the current $\hat{k}_{u_l}$;
     - if no: go step 7.
9. Check whether the stop criterion $|2\pi f_{g=0} - \omega_{u_l}| < \epsilon$ is achieved, for tolerance ϵ.
   - if not: update the frequency to $\omega_{u_l} = 2\pi f_{g=0}$, and update the first velocity of range to $V_0 = V_i - 2\Delta V$. Go to step 5.
   - if yes: the iterative loop to converge this specific pair $(V_{g=0},\ f_{g=0})$ for the current $\hat{k}_{u_l}$ is complete and the pair must be kept as a possible LCO condition, associated with the U_1 computed in step 1. Set $V_0 = V_i$ and go to step 4. It means that the process is continued through the speed range until all pairs $(V_{g=0},\ f_{g=0})$ for this $\hat{k}_{u_l}$, where $V_{g=0} < V_{sto}$, have been found and converged satisfying the given tolerance.

The procedure presented above is illustrated in Fig. 25, in which the variables in squares on the left-hand side are inputs. Note that both typical freeplay DF and the new one for friction are used. The central hatched region indicates the iterative procedure proposed to solve the dependency problem involving frequency/damping values. Note that if the frequency is updated after the negative answer in step 9, the value of airspeed to start the eigenvalue analysis is set close enough to the current $V_{g=0}$, i.e., it starts from $(V_i - 2\Delta V)$ instead of the initial value V_{sta} of the original range. This is an useful strategy to reduce the computational cost by reducing the computational time. In addition, after achieving the numerical convergence, the parameters $(U_1, V_{g=0}, f_{g=0})$ in the circles on the right-hand side of the Fig. 25 correspond to the outputs associated to the possible LCO, and they indicate the amplitude (U_1) and frequency $(f_{g=0})$ occurring in the converged airspeed $(V_{g=0})$. The analysis of the original airspeed range can be continued starting from the velocity right after the converged $V_{g=0}$, using ω^0. The procedure is performed until V_i achieves V_{sto}, when the whole process can be repeated for the next equivalent stiffness in the considered range.

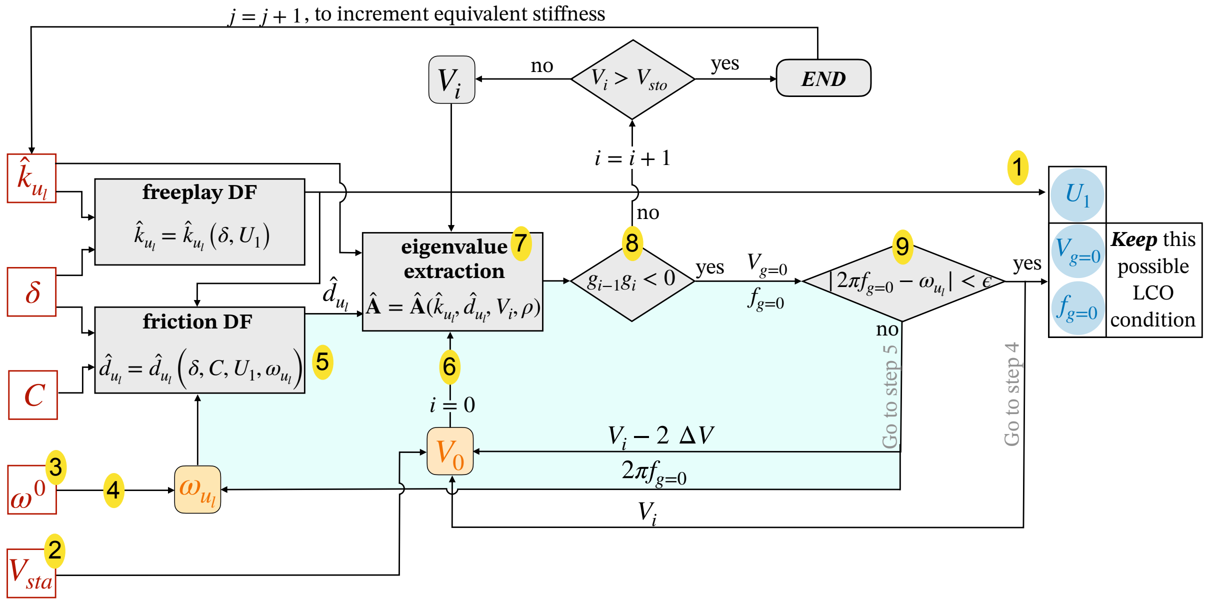

Figure 25 – Iterative process to apply the Equivalent Linearization Technique combined with a describing function if freeplay and friction are considered to predict LCOs.

The iterative solution in terms of the frequency (i.e., the eigenvalue imaginary part) employees a computational procedure conceptually similar to that proposed by Rodrigues, Dowell and Bueno (2020). Their method is computed to achieve convergence between the oscillating frequency of magnetorheological damper equivalent properties (connected to the aeroelastic system) and the corresponding reduced frequency when solving a modified p-k method. Then, the iterative-ELT proposed herein is suitable for multiple DOF aeroelastic systems, such as a real aircraft model described in the generalized system coordinates and commonly obtained through commercial software such as NASTRAN Yuan, Zhang and Poirel (Aug. 2021).

4.3 Results and Discussion

This section presents numerical results to demonstrate both applications involving the ELT. The methodology is applied in the 3-DOF typical section (detailed in chapter 2) for which the control surface rotation presents freeplay such that $\beta \equiv u_l$, the restoring torque is $f_\beta^\delta \equiv f_l^\delta$ and $k_\beta \equiv k_{u_l}$. Two different configurations of the 3-DOF typical section are considered: the airfoils $\mathcal{A}_1$ and $\mathcal{A}_2$ (see Table 2). These two configurations are investigated by considering time domain simulations to confirm the presence of harmonics in the aeroelastic response with freeplay (for the first application) and to confirm a single harmonic response when considering both friction and freeplay as proposed in the second application.

Results for HB3-ELT method - systems with freeplay

The airfoil $\mathcal{A}_2$ is considered with freeplay acting on the control surface rotation. Numerical simulations employing the Hénon's technique for this kind of system are presented in the time domain by Wayhs-Lopes, Dowell and Bueno (2020). The eigenvalue analysis of the nominal linear system (i.e., without freeplay) reveals that flutter occurs at velocity and frequency $V_F = 18.70$ m/s and $f_F = 4.99$ Hz, respectively. Including freeplay $\delta = 0.5^o$ at $V = 0.44V_F$, both spectral content of control surface displacement and restoring torque obtained by time integration are shown in Fig. 26. Note that these spectra are different from each other. In addition, when the fifth harmonic is compared with the third harmonic, for example, the force and displacement amplitude ratio (i.e., F_n/U_n) is not a constant value of equivalent stiffness $\hat{k}_\beta$, such as previously assumed in Eq. (17).

Figure 27 (top) presents the LCO spectrum computed by Fourier transform of the time domain response, for the same particular velocity. The LCO amplitude (U_1) computed using the classic DF is highlighted by the circle symbol, and it is in good agreement to the value computed from the time domain solution. This figure also shows both first and third harmonic amplitudes computed by the proposed approach, the HB3-ELT. Note that the first harmonic is (slightly) better predicted by DF. On the other hand, the prediction of the third harmonic amplitude by this new approach can provide interesting additional

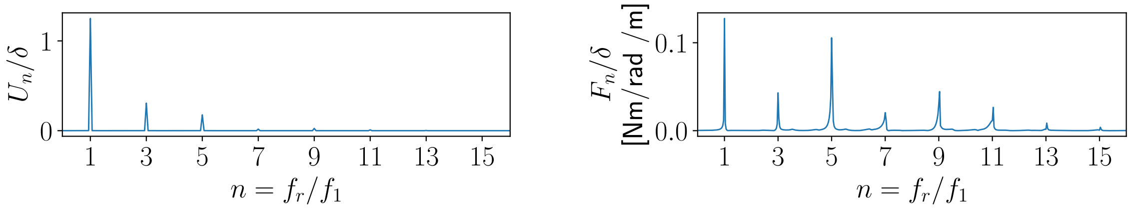

Figure 26 – Content of nonlinear displacement (U_n) and nonlinear force (F_n) spectrum computed at airspeed V/V_F = 0.44 and for an equivalent stiffness $\hat{k}_\beta$ = 0.097584 Nm/rad /m (f_1 = 3.50 Hz).

information for this type of motion. Figure 27 (bottom) shows the motion in time domain. Note that the exact curve integrated by numerical integration has a similar shape to that assumed in methodology (see Fig. 22). Also, the dotted and dashed lines correspond to the curves ($U_1 \sin\theta$) and ($U_1 \sin\theta + U_3 3\sin\theta$) evaluated using the coefficients U_n computed via DF and HB3-ELT, respectively. The curves show that the frequency predicted by the eigenvalue analysis is consistent with the time solution, even for this type of motion with multiple harmonics.

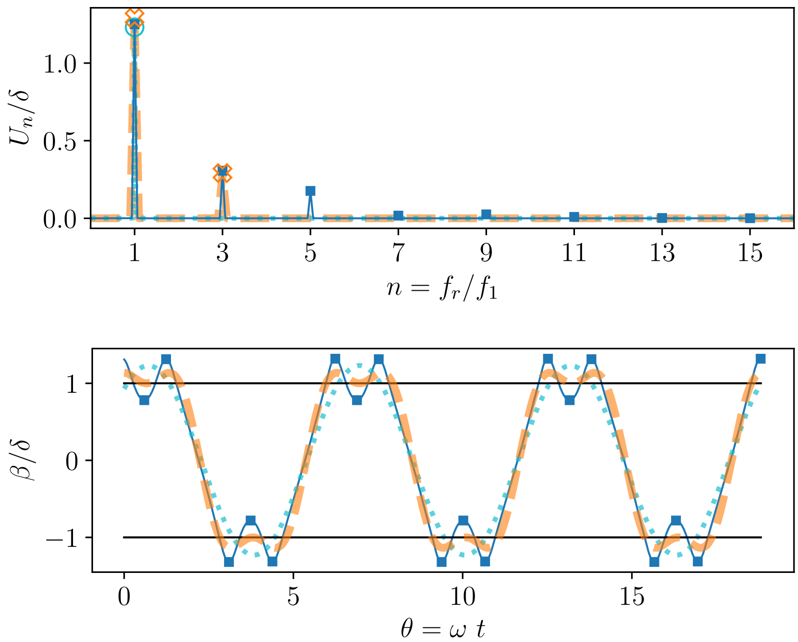

Figure 27 – LCO in the time domain: computed from the time integration (solid line and square ■); proposed approach HB3-ELT (dashed line and ⯐); $\hat{\beta} = U_1 \sin\theta$, DF (dotted line and circle ○). The airspeed V/V_F = 0.44 and equivalent stiffness $\hat{k}_\beta$ = 0.097584 Nm/rad /m (f_1 = 3.50 Hz). The horizontal lines indicate the freeplay boundaries.

The LCO prediction for the $\mathcal{A}_2$ is performed based on a range of $0 < p < 1$. The results of step I. are obtained from the classic eigenvalue analysis (see Fig. 28). In addition, Fig. 29 shows the results of step $II.$. The dotted curve indicates the classic DF, such as presented in Fig. 19b, and the dashed curves show the results of $\bar{U}_1$ and $\bar{U}_3$ converged as solution of the algebraic system (Eq. 17) employing the Numerical Continuation method. Both methods predict different behavior for the first harmonic, but note that the amplitude is larger than the freeplay boundary ($U_1/\delta > 1$). Also, the new approach provides information about the third harmonic. The results from step $II.$ indicate the existence of a general non-dimensional solution for the algebraic system that does not depend on the typical section physical and geometric parameters. Note that the algebraic system in Eq. (17) depends on the non-dimensional harmonic coefficients $\bar{U}_1$ and $\bar{U}_3$ and the cross non-dimensional time $\theta_{\delta i}$. This characteristic is similar to the classic DF: it is independent of the typical section parameters. The particular result for each studied typical section is attributed only to the eigenvalue analysis (step $I.$, the ELT).

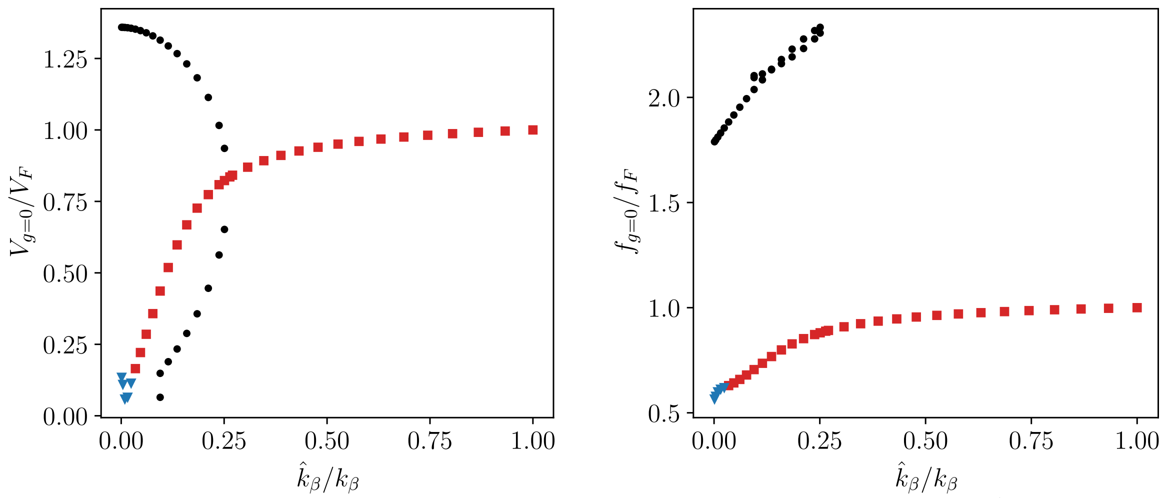

Figure 28 – Results of the ELT for the complete range of $0 < p < 1$ for $p = \hat{k}_\beta/k_\beta$. System $\mathcal{A}_2$: $V_F = 18.70$ m/s and $f_F = 4.99$ Hz.

Figure 30 shows the combined results previously shown in Fig. 28 and 29, corresponding to the amplitude (left-hand side) and frequency (right-hand side) predictions by this proposed approach. Solid lines indicate the results from the time domain simulations, whereas circle symbols show amplitude and frequency for the first harmonic predicted by the classic DF. On the other hand, cross symbols (⮿) show that the predicted amplitudes for the third harmonic (U_3), although not exact, provide interesting information for a wide range of airspeed ($V/V_F > 0.35$). However, at low airspeed (i.e., $V/V_F < 0.35$) both DF and this new approach predict LCOs that are not confirmed by time domain solutions. This characteristic has previously been reported in the literature for DF, as shown by Kholodar and Dickinson (2010) and Bueno, Góes and Gonçalves (2014) for example. See Fig. 31

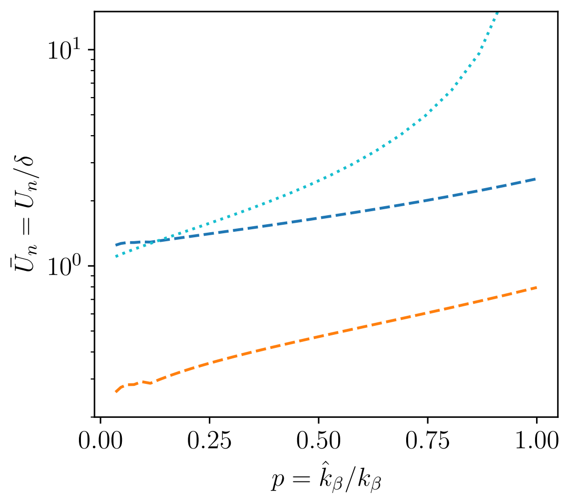

Figure 29 – Results of step II. for $0 < p < 1$. Dotted line: classic DF (see Fig. 19b; dashed lines: solution of Eq. (17), $\bar{U}_1$ (top) and $\bar{U}_3$ (bottom) converged employing the Numerical Continuation.

showing the time solution for $V/V_F = 0.16$, at which no LCO is identified.

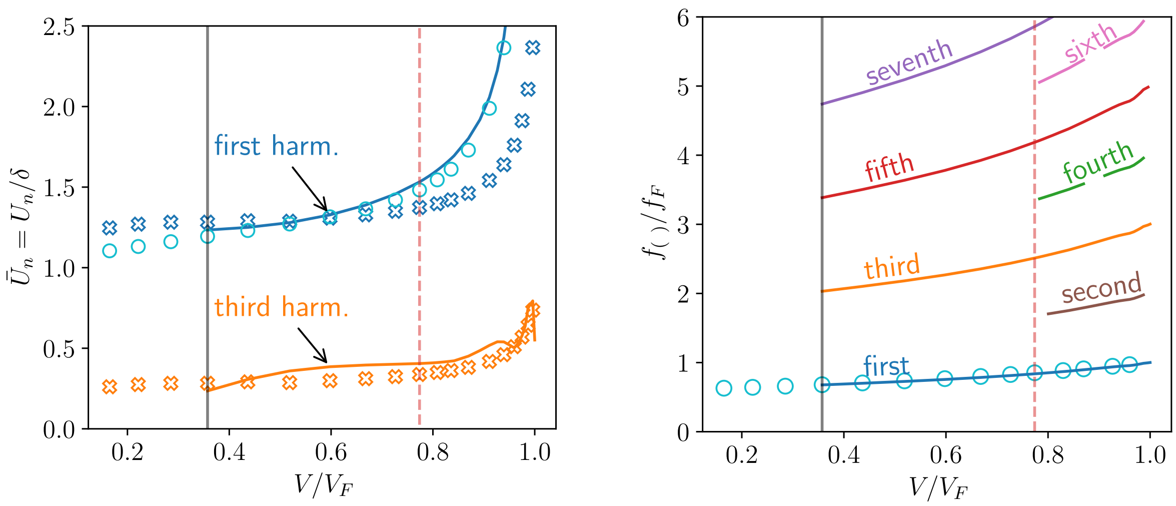

Figure 30 – LCO amplitudes (left-hand side) for the first (U_1, top) and third (U_3, bottom) harmonics: results from the time domain simulations (solid line); DF (circle ○); proposed approach HB3-ELT (cross symbol ✕). LCO frequencies (right-hand side) for f_1, f_2, ..., f_7 from time simulations (solid line) and for the fundamental harmonic $f_{g=0}$ from DF (circle ○). Solid vertical line: $V/V_F = 0.35$ (where time LCO starts); dashed vertical line: $V/V_F = 0.77$ (even harmonics appear).

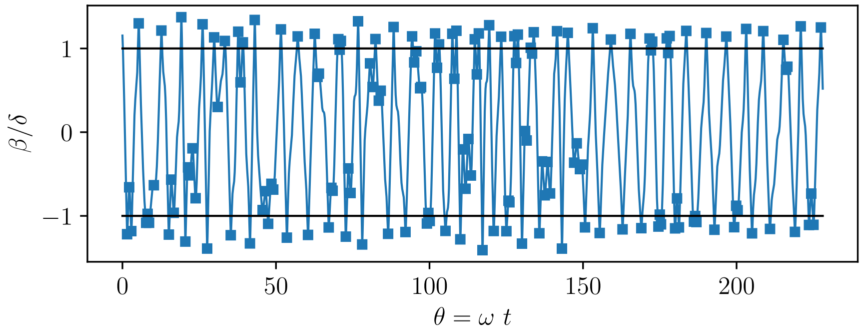

Figure 31 – Time response computed from the time integration for $V/V_F = 0.16$. No LCO identified.

Regarding the amplitude, the results show that the first harmonic is more accurately predicted by classic DF, especially for the range $V/V_F > 0.77$. This velocity $V = 0.77V_F$ is near the airspeed at which the even harmonics (mainly the fourth) start to appear, as highlighted by the vertical dashed line in Fig. 30b. Also, although the $\mathcal{A}_2$ presents LCO with multiple harmonics (see Fig. 32), note that Fig. 30a shows the amplitudes of the first and third harmonics to keep the information visually clear. Finally, note that the eigenvalue analysis provides two different branches of LCO (see Fig. 28), and the final LCO prediction shows only the red branch. The results additionally show that the frequency prediction from the classic linear stability analysis for a range of equivalent stiffness is still a good choice to determine the first harmonic, even with high order harmonics present in the motion.

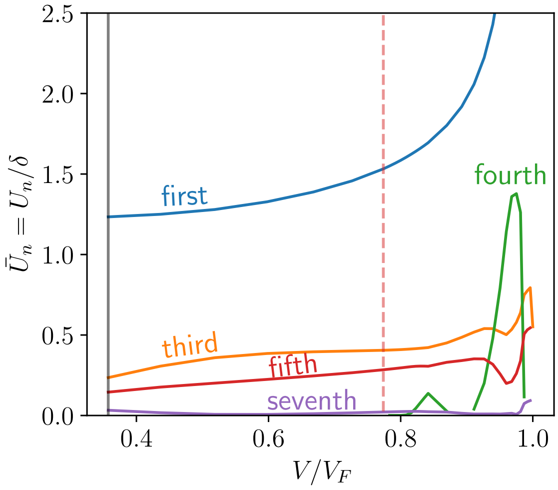

Figure 32 – LCO amplitudes from the time domain simulations highlighting the high order harmonics. Solid vertical line: $V/V_F = 0.35$ (where time LCO starts); dashed vertical line: $V/V_F = 0.77$ (even harmonics appear).

Results for iterative ELT - system with freeplay and friction

The LCO prediction for the $\mathcal{A}_1$ with freeplay is presented in Fig. 21. This result refers to the classic DF method (first row in Tab. 3). In this section, both freeplay and friction are considered, and the range of equivalent stiffness previously assumed is used to employ the required iterative ELT (third row in Tab. 3). Note that the step to relate the equivalent stiffness to the LCO amplitude is exactly the same obtained for the system with no friction (via the freeplay describing function shown in Fig. 19b). The main difference occurs in the stage related to the correlation of the equivalent stiffness with each pair ($V_{g=0}$, $f_{g=0}$), once the iterative procedure is required to adjust a valid equivalent damping $\hat{d}_\beta$. The equivalent stiffness range is covered to perform the iterative ELT for two cases of friction (C = 1.25 10^{-3} and C = 3.75 10^{-3} Nm /m). Figure 33 shows the results of this procedure. Note that a single value of equivalent stiffness may present multiple marginally stable conditions and, because of the iterative procedure, each pair ($V_{g=0}$, $f_{g=0}$) is related to a particular equivalent damping $\hat{d}_\beta$, as presented in Fig. 34 (left).

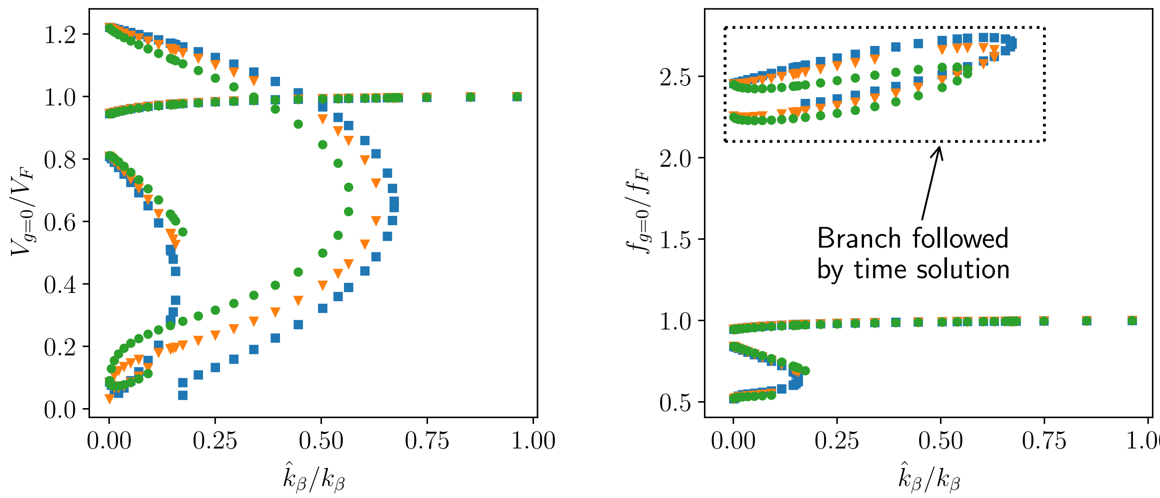

Figure 33 – Marginally stable conditions ($V_{g=0}, f_{g=0}$) obtained via ELT (with iterative procedure in the cases with friction) in terms of the equivalent stiffness $\hat{k}_\beta$. No friction (■); C = 1.25 10^{-3} Nm /m (▼); C = 3.75 10^{-3} Nm /m (●).

Figure 34 shows the branch highlighted by the dotted rectangle in Fig. 33 (right), which is the branch of LCO identified by time domain simulations. Comparing the two curves on the left-hand side plot, different levels of $\hat{d}_\beta$ are observed for a particular value of p due to the influence of C and $f_{g=0}$. On the other hand, when a linear equivalent damping ratio is defined as $\xi_{eq} = \hat{d}_\beta/(4\pi I_\beta f_{g=0})$ and plotted against the airspeed, it is possible for the two curves to exhibit similar levels of ξ_{eq}. This similarity arises due to the potential occurrence of multiple pairs ($V_{g=0}$, $f_{g=0}$) for a single p, as revealed in Fig. 34 (right) for the range $V/V_F < 0.15$.

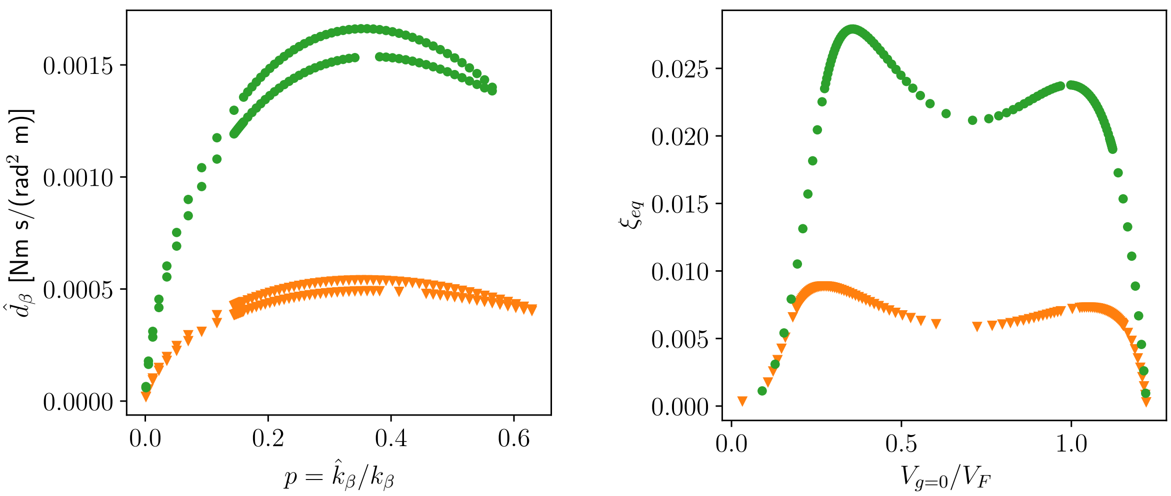

Figure 34 – Converged values of equivalent damping and $V_{g=0}$ by Iterative-ELT for the range $0 < p < 1$. Equivalent damping ratio: $\xi_{eq} = \hat{d}_\beta/(4\pi I_\beta f_{g=0})$. Legend: $C = 1.25\ 10^{-3}$ Nm /m (▼); $C = 3.75\ 10^{-3}$ Nm /m (●).

Relating the ELT results in Fig. 33 to the LCO amplitude U_1 (Fig. 19b), the LCO prediction shown in Fig. 35 reveals the branch identified by the time domain solutions. The results show that this proposed method is suitable to predict LCO for systems with both freeplay and friction acting on the same DOF. They demonstrate that it is important to consider friction to predict the LCO, otherwise, if the classic DF is considered (with no iterative procedure) inaccurate results are obtained.

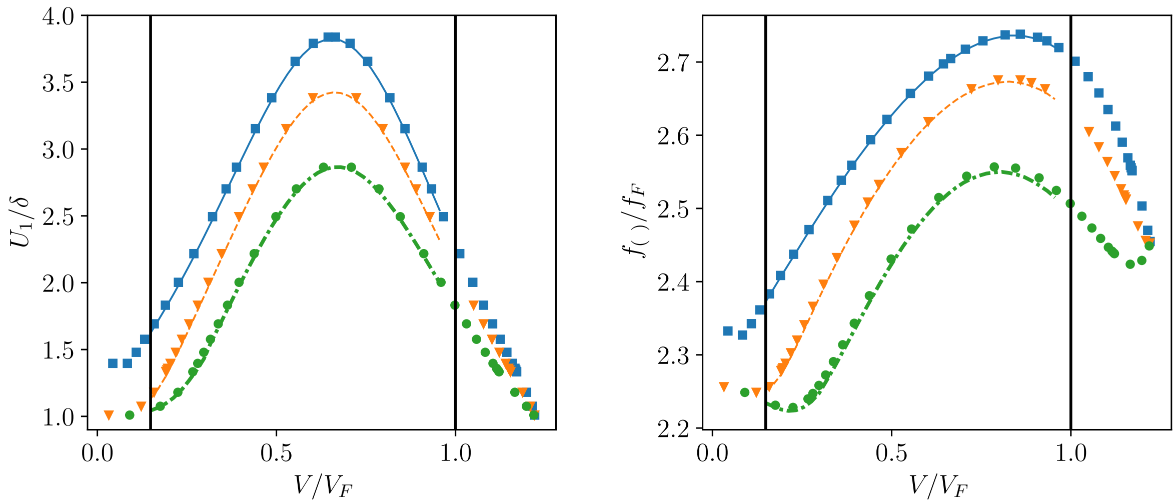

Figure 35 – Prediction of amplitude and frequency of the possible LCO conditions via ELT employing iterative procedure, for the system with simultaneous freeplay (δ = 0.5 deg) and friction. Legend: symbols for ELT ($f_{g=0}$) and lines (f_1) for time integration as referece (H). No friction (■, solid line); $C = 1.25\ 10^{-3}$ Nm /m (▼, dashed line); $C = 3.75\ 10^{-3}$ Nm /m (●, dash-dotted line).

In terms of a conceptual point of view, and based on this general formulation, the present approach can be used to investigate different nonlinearities. However, in practice, a describing function must be developed for each particular case. In this sense, note that Padmanabhan, Dowell and Pasiliao (2018) present describing functions for several types of nonlinearities, including the polynomial ones, and their results can be considered to evaluate this proposed method. Regarding the HB3-ELT method, its formulation is presented to include additional harmonics. However, their consideration needs to be investigated in further studies. On the other hand, note that higher harmonics are associated with smaller amplitudes, and the inclusion of both first and third harmonics can provide representative results in comparison with experimental responses. Furthermore, in cases where the third harmonic has a considerable magnitude, it may significantly affect fatigue life, and considering it is crucial for more accurate predictions. Finally, the inclusion of the third harmonic (in addition to the first one) when considering freeplay and friction introduces additional parameters for solving the iterative approach, and the method feasibility and accuracy need to be investigated.

4.4 Concluding Remarks

This chapter is focused on presenting an approach to predict LCO in aeroelastic systems with discontinuous nonlinearities. The Equivalent Linearization Technique (ELT) is the basis of the technique proposed herein due to its relatively reduced computational cost. The main idea is to extend the use of the ELT by a combination of classic linear eigenvalue analysis with describing functions obtained via Harmonic Balance to obtain the LCO frequency and amplitude. In this sense, the classic Describing Function method formulation to consider freeplay is a particular application in which the eigenvalue analysis and the well known freeplay describing function are employed.

Two applications are described and proposed. They comprise a new DF in the matrix form to consider both first and third harmonics in systems with freeplay (HB3-ELT); and an iterative-ELT with a particular DF used with the classic DF to predict the first harmonic in systems with feeplay and friction acting on a single DOF. Numerical simulations were performed for a 3-DOF typical section airfoil with these control surface nonlinearities. The approaches can be employed to investigate multiple degrees of freedom aeroelastic systems without substantially increasing the computational effort required for a regular linear flutter analysis.

The results showed that if freeplay is considered, the classic DF is accurate to predict the LCO first harmonic amplitude and frequency, even when the response actually presents higher order harmonics. On the other hand, the classic DF provides information on the first harmonic, whereas the proposed approach provides additional information on the third harmonic amplitude.

The results for the second application were obtained by considering both freeplay and friction nonlinearities acting on the control surface degree of freedom. The proposed ELT-iterative method has shown accurate results to predict LCO if both nonlinearities act on the system. Although friction is an amplitude reducer, it is important to consider its effect on the system response to achieve a more accurate prediction of limit cycle oscillations in aeroelastic systems, and further investigations can be carried out to consider these nonlinearities if the first and third harmonics are present in the system responses.

5 Freeplay in Multiple DOFs

Single control surface (CS) freeplay has been extensively investigated in the aeroelastic literature and several studies describe its effect on the limit cycle oscillations. Airworthiness regulations establish that this discontinuous nonlinearity needs to be considered in both CS and trailing-edge tab, if the latter one exists. In this context, this chapter investigates the effects of freeplay from both CS and tab on the LCO. The four degree-of-freedom typical section is considered, highlighting the main differences when compared with the freeplay of a single trailing-edge surface.

Time marching solutions with the Hénon's technique is employed to capture the freeplay effect in the LCO comparing the case where the nonlinearity acts on both elements with the typical case of a single CS freeplay. Bifurcation diagrams are presented and phase portraits are shown to highlight the different LCOs for each freeplay configuration case. The results show that higher amplitudes can be identified for this configuration when compared to the classical case.

5.1 Freeplay Scenarios

The 4-DOF airfoil $\mathcal{A}_3$ is modeled such that plunge (h) and pitch of wing (α) are linear DOFs while the CS (β) and the tab (γ) rotations are considered in three different scenarios regarding the symmetric freeplay inclusion: *i*. CS only, *ii*. tab only, and *iii*. both CS and tab. In this sense, the particularities of each scenario in terms of the parameters present in the discontinuous torque of Eq. (1) include placing the nonlinear DOF u_l at row $l = 3$ ($u_l = \beta$) for scenario *i*., at row $l = 4$ ($u_l = \gamma$) for scenario *ii*. and in both rows 3 and 4 for scenario *iii*.. Fixed values of freeplay amplitude are considered, such that $\delta^\beta = 0.2°$ and $\delta^\gamma = 0.4°$ for the control surface and for the tab, respectively.

The stiffness matrix of the overlying system $\mathbf{K}$ has the nominal stiffness k_β placed on the 3rd row and 3rd column, and k_γ placed on the 4th row and 4th column. Then, the general equation of motion (Eq. 10) is explicitly written for the three freeplay scenarios in terms of the modified matrix $\mathbf{K}_l$, which is employed in Eq. (10) instead of $\mathbf{K}$ when computing the modified aeroelastic matrix $\mathbf{A}_l$,

$$\begin{array}{c|c|c}
\textbf{Scenario } \boldsymbol{i.}\ (l=3) & \textbf{Scenario } \boldsymbol{ii.}\ (l=4) & \textbf{Scenario } \boldsymbol{iii.}\ (l=3,4) \\
\text{freeplay in CS only} & \text{freeplay in tab only} & \text{freeplay in both CS and tab} \\
 & & \\
\dot{\mathbf{x}} = \mathbf{A}_3\mathbf{x} - \mathbf{b}_3^\delta & \dot{\mathbf{x}} = \mathbf{A}_4\mathbf{x} - \mathbf{b}_4^\delta & \dot{\mathbf{x}} = \mathbf{A}_{3,4}\mathbf{x} - \mathbf{b}_3^\delta - \mathbf{b}_4^\delta
\end{array} \quad (21)$$

where $\mathbf{A}_3$ is computed with the stiffness matrix $\mathbf{K}_3 = \text{diag}(k_h,\ k_\alpha,\ 0,\ k_\gamma)$; $\mathbf{A}_4$ is computed with $\mathbf{K}_4 = \text{diag}(k_h,\ k_\alpha,\ k_\beta,\ 0)$; and $\mathbf{A}_{3,4}$ is computed with $\mathbf{K}_{3,4} = \text{diag}(k_h,\ k_\alpha,\ 0,\ 0)$. The vectors $\mathbf{b}_l^\delta$ are described in Eq. (11).

5.2 Stability Analysis of the Sub-linear Systems

Based on Eq. (1), the symmetric freeplay included at the l-th DOF provides two different sub-linear systems: outside of the freeplay $u_l > |\delta^l|$ and inside of the freeplay $u_l < |\delta^l|$. The state space equations in Eq. (21) show that the discontinuity effect is carried only in the vectors $\mathbf{b}_l^\delta$, whilst the modified dynamic matrix $\mathbf{A}_l$ is kept constant. However, note that the modified vector $\mathbf{b}_l^\delta$ contains a parcel dependent on the state u_l, and therefore, if the typical linear stability analysis needs to be performed by extracting the eigenvalues from the dynamic matrix, all terms related to the system state must be included in this matrix. Therefore, a different way of writing the equation of motion makes use of the vector $\bar{\mathbf{b}}_l^\delta$, which contains the parcels of Eq. (1) not involving any state; and the actual dynamic matrix $\bar{\mathbf{A}}_l$. The practical effect for a single freeplay is that both $\bar{\mathbf{b}}_l^\delta$ and $\bar{\mathbf{A}}_l$ are discontinuous in the following way:

Inside of freeplay: there is no need of $\bar{\mathbf{b}}_l^{\delta}$[I] and $\bar{\mathbf{A}}_l = \mathbf{A}_l$, indicating that the stiffness matrix used is $\mathbf{K}_l$, already described having zero instead of the nominal stiffness k_{u_l}.

Outside of freeplay: $\bar{\mathbf{b}}_l^\delta = \text{sign}(u_l)\delta^l k_{u_l}\,\{\mathbf{M}_a^{-1}\mathbf{w}_l\ 0\ \dots\ 0\}^T$ where $\mathbf{w}_l$ is the $n_{\text{dof}} \times 1$ vector $\mathbf{w}_l = \{0\ \ \dots\ \ 0\ \ \ 1|_l\ \ \ 0\ \ \dots\ \ 0\}^T$; and $\bar{\mathbf{A}}_l = \mathbf{A}$ employs the nominal stiffness k_{u_l} resulting in the linear system matrix.

Therefore, the general first order equation for which $\bar{\mathbf{A}}$ is the actual dynamic matrix of the system is $\dot{\mathbf{x}} = \bar{\mathbf{A}}\mathbf{x} + \bar{\mathbf{b}}^\delta$, where $\bar{\mathbf{A}}$ and $\bar{\mathbf{b}}^\delta$ are particular for each region created by the combination of all DOFs including freeplay. Particularly, scenario *iii.* has four different sub-linear systems, since the two regions (outside and inside) for each freeplay must be

[I] $\bar{\mathbf{b}}_l^\delta$ is a $N \times 1$ vector of zeros combined, resulting in $\bar{\mathbf{A}}$ and $\bar{\mathbf{b}}^{\delta}$ defined by the following table.

Sub-linear System	**CS Freeplay**	**Tab Freeplay**	$\bar{\mathbf{A}}$	$\bar{\mathbf{b}}^{\delta}$
Inner of both	IN	IN	$\mathbf{A}_{3,4}$	$\nexists$
Inner of CS	IN	OUT	$\mathbf{A}_3$	$\bar{\mathbf{b}}_4^{\delta}$
Inner of tab	OUT	IN	$\mathbf{A}_4$	$\bar{\mathbf{b}}_3^{\delta}$
Nominal System	OUT	OUT	$\mathbf{A}$	$\bar{\mathbf{b}}_3^{\delta} + \bar{\mathbf{b}}_4^{\delta}$

Table 4 – Aeroelastic dynamic matrices for the sub-linear systems.

A linear flutter analysis is performed for each of these four sub-linear systems risen from the combination of freeplay regions and the eigenvalues of the respective $\bar{\mathbf{A}}$ in Tab. 4 are extracted (see the V-g-f diagrams in the Fig. 36). For each of them, all the marginally stable flight conditions are kept, i.e., when there is at least one eigenvalue crossing the imaginary axis ($g = 0$). These computed velocities are summarized in the Tab. 5. The flutter velocity for the nominal system $V_F = 24.81$ m/s, above which all scenarios experience the oscillating divergence (the actual flutter), is chosen to refer to fligth conditions using the non-dimensional velocity V/V_F.

Sub-linear system	**Dimensional** $V_F^{(.)}$ [m/s]	**Non-dimensional** $V_F^{(.)}/V_F$
Inner of both $\mathbf{K}_{3,4} = \mathrm{diag}(k_h,\ k_\theta,\ 0,\ 0)$	–	–
Inner of CS $\mathbf{K}_3 = \mathrm{diag}(k_h,\ k_\alpha,\ 0,\ k_\gamma)$	$V_{F1}^{\beta} = 5.17$	$\bar{V}_{F1}^{\beta} = 20.8\%$
Inner of tab $\mathbf{K}_4 = \mathrm{diag}(k_h,\ k_\theta,\ k_\beta,\ 0)$	$V_{F1}^{\gamma} = 2.13$ $V_{F2}^{\gamma} = 5.47$ $V_{F3}^{\gamma} = 13.73$	$\bar{V}_{F1}^{\gamma} = 8.6\%$ $\bar{V}_{F2}^{\gamma} = 22.0\%$ $\bar{V}_{F3}^{\gamma} = 55.4\%$
Nominal System $\mathbf{K} = \mathrm{diag}(k_h,\ k_\alpha,\ k_\beta,\ k_\gamma)$	$V_F = 24.81$	$\bar{V}_F = 100\%$

Table 5 – Marginally stable flight velocities (eigenvalues with null real part) for the sub-linear systems

A mode tracking algorithm is considered to obtain Fig. 36, such that each symbol is an eigenvalue related to a single structural mode. The empty symbols in the g plots indicate positive real part whereas full symbols indicate negative real part. The vertical lines indicate the conditions at which $g = 0$, i.e., the symbol with same color of the vertical line changes its fill style. Although the sub-linear system inside both freeplays does not provide g crossing the imaginary axis, one eigenvalue has positive real part for the whole velocity range simulated, meaning also the system is unstable. Regarding the system inside the CS freeplay only, a vertical line is used to indicate the imaginary axis crossed from negative to positive real part. However, the empty green pentagon symbol indicates another eigenvalue that has $g > 0$ for the whole velocity range. Therefore, even before V_{F1}^{β} the sub-linear system is unstable. Similar behavior is verified for the system inside of tab freeplay only, which is unstable even for $V < V_{F1}^{\gamma}$ (see the empty black circle symbol). Also, in the range $V_{F1}^{\gamma} < V < V_{F2}^{\gamma}$, two eigenvalues have $g > 0$ (circle, square); in the range $V_{F2}^{\gamma} < V < V_{F3}^{\gamma}$, three eigenvalues have $g > 0$ (circle, square, star); and in the last range $V > V_{F3}^{\gamma}$, two eigenvalues have $g > 0$ (circle, star).

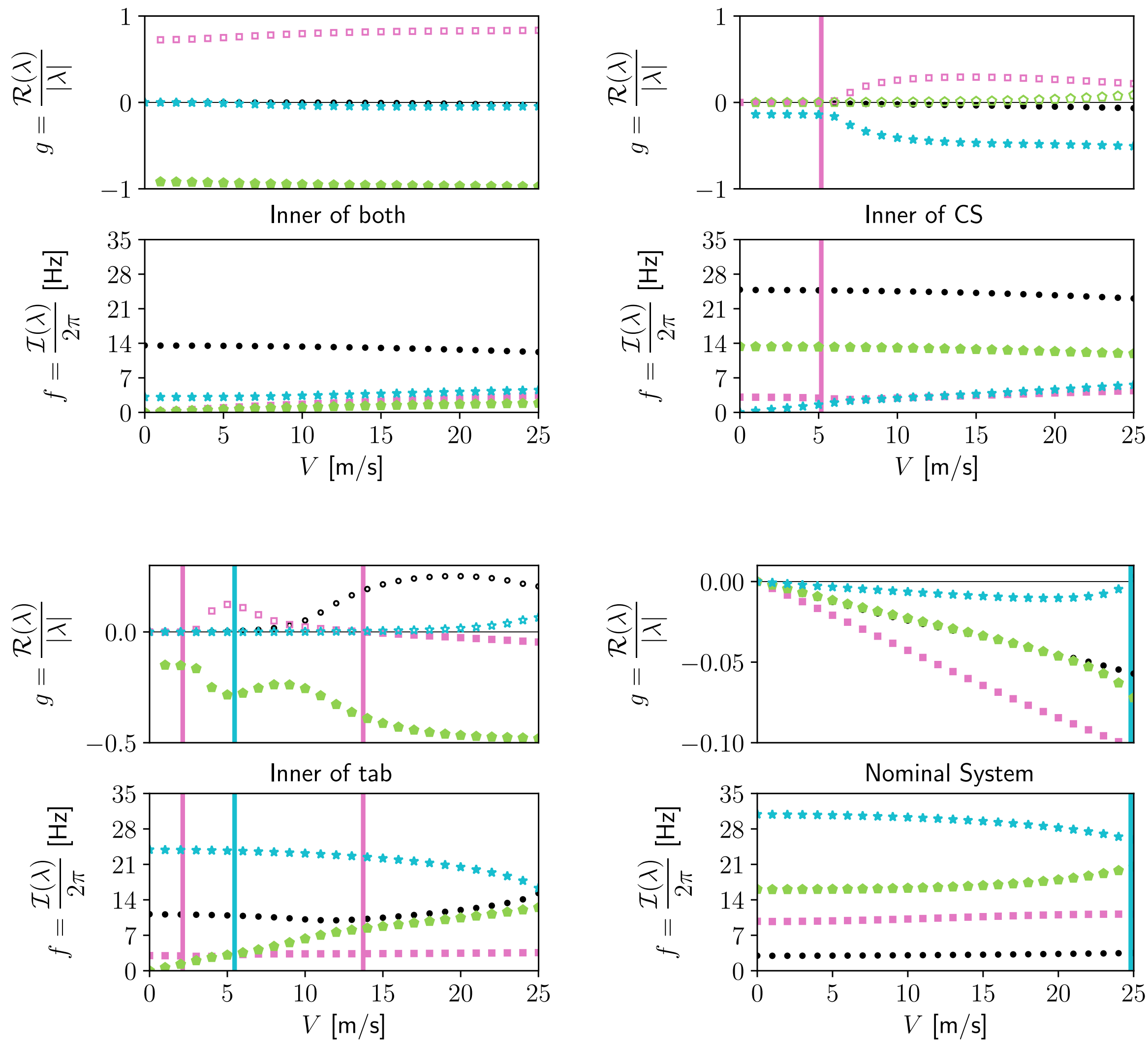

Figure 36 – V-g-f diagram for the four sub-linear systems: inner of both freeplays (top-left), inner of CS freeplay only (top-right), inner of tab freeplay only (bottom-left) and nominal system (bottom-right). Empty symbols ($g > 0$) and full symbols ($g < 0$) on V-g plots. The vertical lines indicate the values from Tab. 5

In general, these velocities of the individual sub-linear systems are important because they indicate a change in the stability of the nonlinear system as a whole, and this can usually be confirmed qualitatively by the behavior changes in the bifurcation diagrams present in this chapter.

5.3 Bifurcation Diagrams

Time marching simulations are performed to obtain the LCOs for different airspeeds. The Runge-Kutta method improved with the Hénon's technique is employed. Note that the technique is applied for both freeplays (CS and tab hinge) for the scenario *iii*. The procedure to construct bifurcation diagrams of the extremes (inversion points) against airspeed is performed as described in section 3.3, i.e., a state belonging to the steady solution for V_i is used as initial condition for V_{i+1}, making faster the computational convergence to find a LCO.

A range of airspeed $0 < V < V_F$ with step 0.25 m/s is used to construct the described bifurcation diagrams in both directions (increasing and decreasing airspeed) for all the three scenarios, as shown in Fig. 37. The diagrams show the extremes of the nonlinear DOF only, in the way that there are two diagrams for the scenario with multiple freeplay (*iii.*), showing the CS extremes (b) and the tab extremes (d).

Different responses are obtained for scenario *i.* when increasing or decreasing the airspeed, and there is no airspeed range reaching the same steady state when comparing these two situations. When decreasing the airspeed, a clear branch is followed with basically two inversion points in each flight condition, highlighted for $V/V_F = 30.0\%$ on the left-hand side in Figure 38. The red rectangle highlights a single period with only two inversion points marked by the diamond symbols (note them also in the phase space plot, where the closed trajectory crosses $\dot{\beta} = 0$ twice), which is an indicative of a simple LCO, i.e., mainly the first harmonic is present, as confirmed in the spectrum content of this steady state. On the other hand, for this same flight condition, the solution obtained when increasing the airspeed is not completely periodic (i.e., it is not a perfect LCO), but instead, it is a quasi-periodic solution (see right-hand side of Fig. 38). For this type of motion, the spectrum content includes some irreducible frequencies, i.e., not multiple of f_1, considered here the frequency of the component with the highest proportion. In this sense, the inversion points appear in several values of β (see the circle symbols in the time response and in the phase space plot on the right-hand side). Despite this behavior, these inversion points of the quasi-periodic solution are limited by a general CS position quite similar to the branch of the simple LCO.

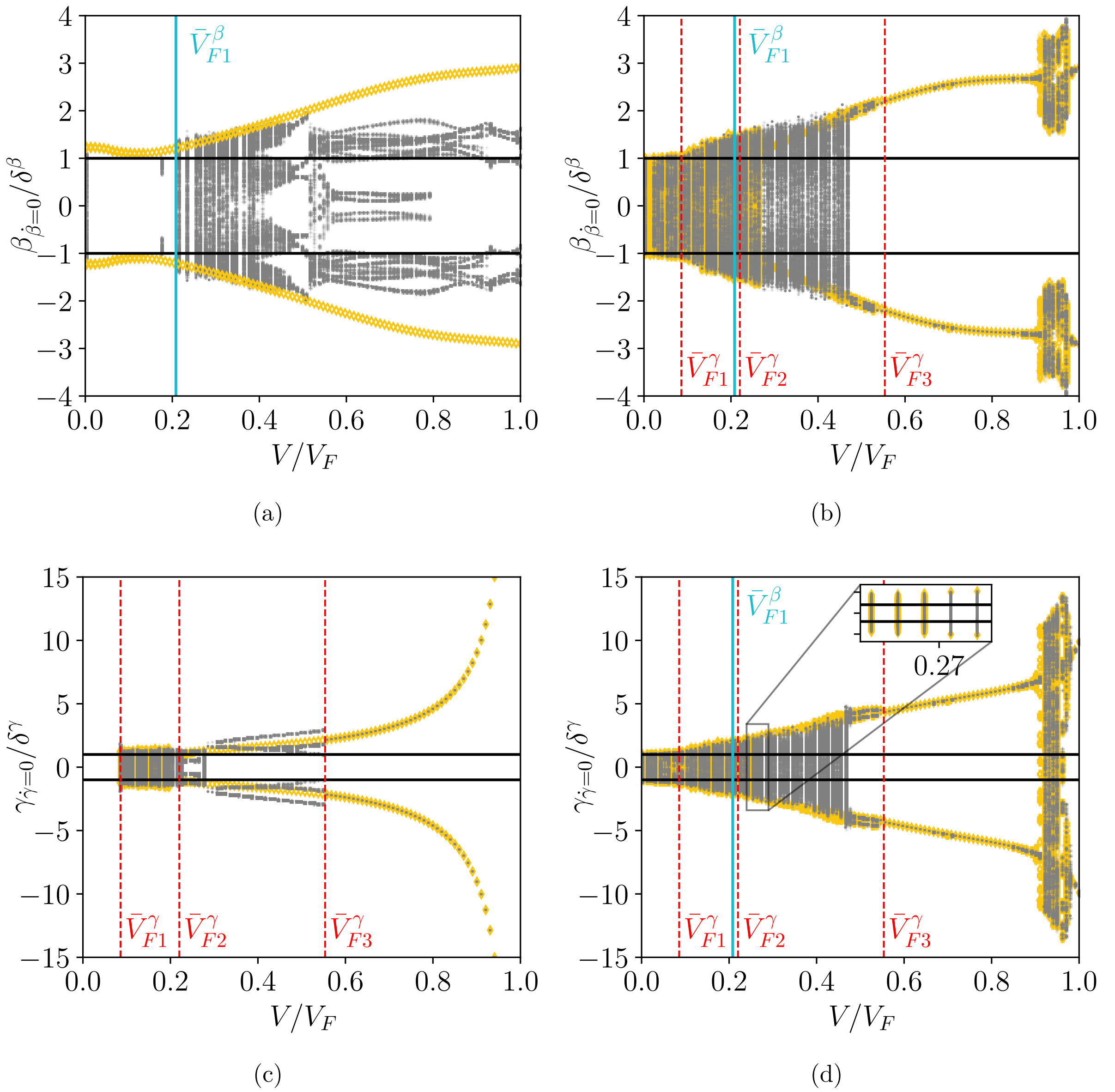

Figure 37 – Bifurcation diagrams for the CS and tab inversion points ($\dot{\beta} = 0$ and $\dot{\gamma} = 0$) when increasing (grey dot) and decreasing (yellow diamond) the airspeed. (a) scenario *i.*; (c) scenario *ii.*; (b) and (d) scenario *iii.*

Increasing the airspeed in scenario *i.*, the quasi-periodic solutions starts giving way to a different kind of LCO, which is established in a flight condition around $V/V_F \approx 46.0\%$. This new LCO is much more complex with several inversion points in a single period, and it is kept evolving with some changes in the spectral content until V_F (see Fig. 39).

In contrast to scenario *i.*, Fig. 37 shows that both scenarios *ii.* and *iii.* include some airspeed range for which both ways of varying the airspeed converge to the same response (either quasi-periodic or LCO). For example, for scenario *ii.* quasi-periodic solutions are observed for the range $V^{\gamma}_{F1} < V < V^{\gamma}_{F2}$ and the same LCO is obtained for $V > V^{\gamma}_{F3}$ regardless the direction. On the other hand, the solution for the range $V^{\gamma}_{F2} < V < V^{\gamma}_{F3}$ converges for

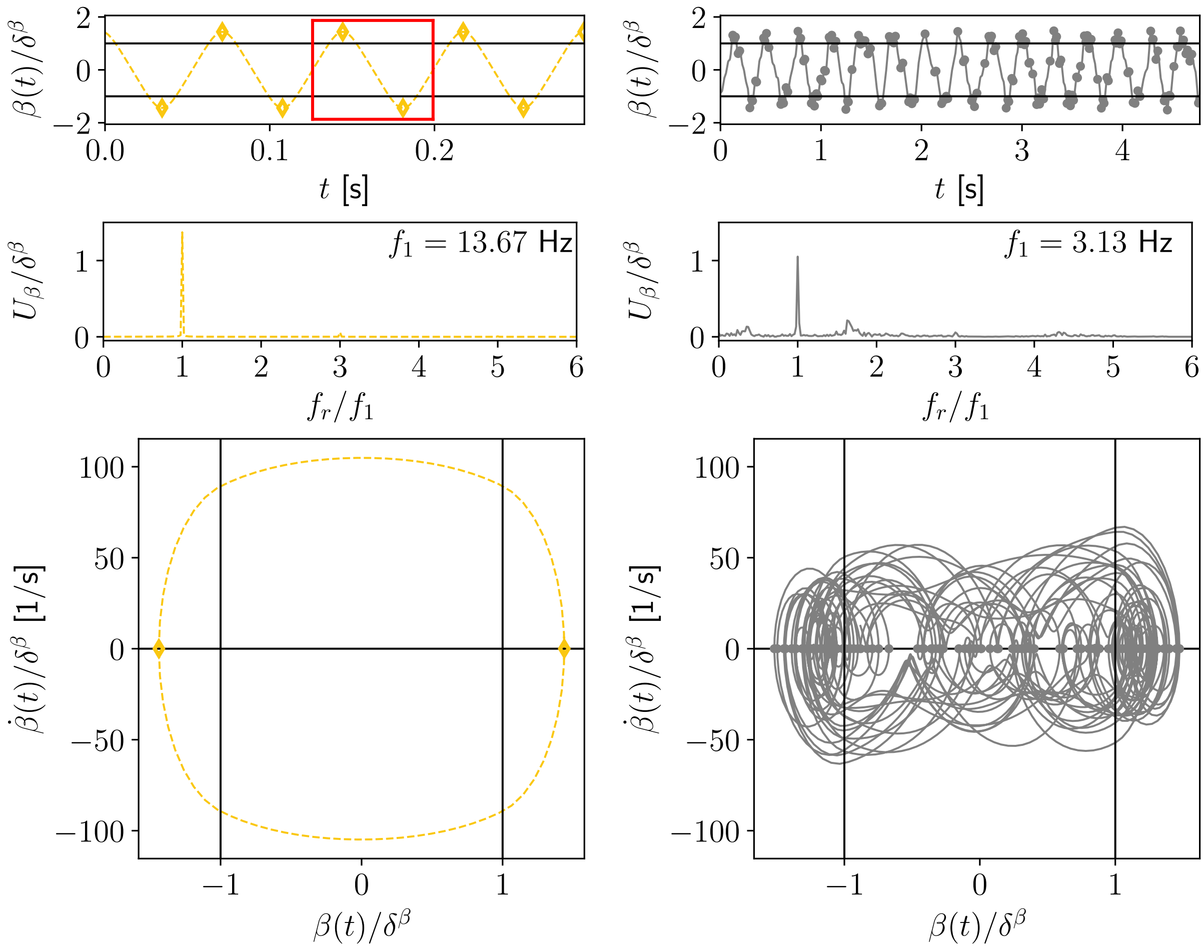

Figure 38 – Scenario *i.*: time response, portrait and spectrum for $V/V_F = 30.0\%$ when decreasing (left) and increasing (right) the airspeed. f_1 represents the frequency of the dominant harmonic of each response.

different LCOs, the branch of the simple LCO with two inversion points is kept when the airspeed is decreased, but a more complex LCO appears when increasing the airspeed (see Fig. 37c). Similar behavior can be observed for scenario *iii.*, where quasi-periodic solutions appear for $V/V_F < 27\%$ and simple LCO with two inversion points is reached for $47\% < V/V_F < 89\%$ regardless the direction. On the other hand, while the decreasing direction reaches a LCO for $27\% < V/V_F < 47\%$, the increasing direction presents quasi-periodic solutions.

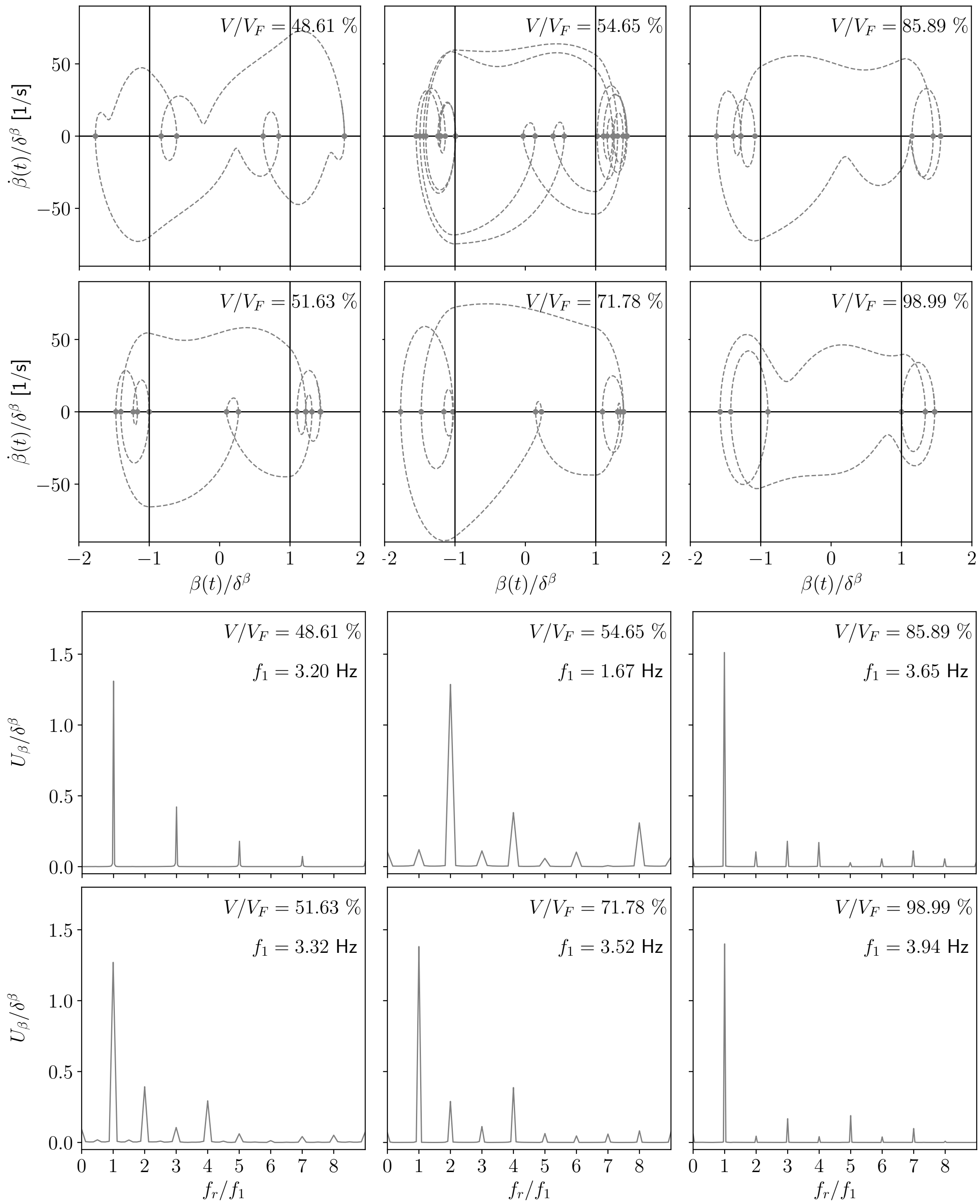

Figure 39 – Scenario *i.*: phase space portrait and spectrum content for particular flight conditions when increasing the airspeed.

5.3.1 Poincarè Sections

The phase portraits such those in Fig. 39 show $\beta(t_i)$ against $\dot{\beta}(t_i)$ for all time instants t_i of the steady state reached. A LCO can be well recognized in this kind of plot as a closed curve. However, a different approach to presenting the data in a phase plane involves plotting information specific to a particular event, rather than encompassing all t_i values. This plot is called Poincarè section and it is useful mainly to deal with quasi-periodic or chaotic solution (DIMITRIADIS, 2017b). If they do not present any pattern when plotted for all times t_i, they may present a recognizable behavior if plotted in a Poincarè section. Figure 40 shows Poincarè sections for scenario *ii.* when $\dot{\alpha} = 0$ and $\alpha > 0$. Qualitatively, the more spread out the points, the more chaotic the solution (from first to fourth airspeeds shown in this figure). When the points become more dense in particular regions, the solution is transformed in quasi-periodic motion, until it presents a single point indicating the LCO.

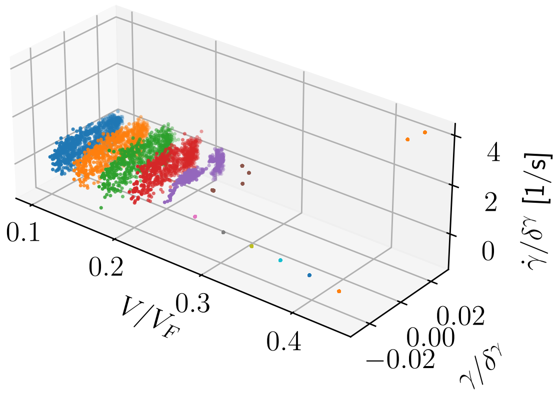

Figure 40 – Scenario *ii.*: Poincarè sections ($\dot{\alpha} = 0$ and $\alpha > 0$) for range between V_{F2}^{γ} and V_{F3}^{γ} (solutions obtained with initial conditions used when increasing airspeed).

Different ratios of freeplay $R = \delta^\gamma/\delta^\beta$ are considered to plot Poincarè sections for scenario *iii.*, keeping $\delta^\beta = 0.2°$ fixed. These sections are significant considering a time equal to 300 s for the simulation and the points corresponding to the last 200 s of data are considered to be plotted. Fig. 41a shows for $R = 2$ that the first two airspeeds plotted present chaotic solution, while LCO appears for the other flight conditions. If $R = 0.25$ (Fig. 41b), an additional airspeed presents chaotic solution. Finally, if the freeplay in tab becomes larger with $R = 4$, the solutions are mainly chaotic, and the second last airspeed starts presenting the points with defined pattern, going towards a quasi-periodic solution shown for the last airspeed.

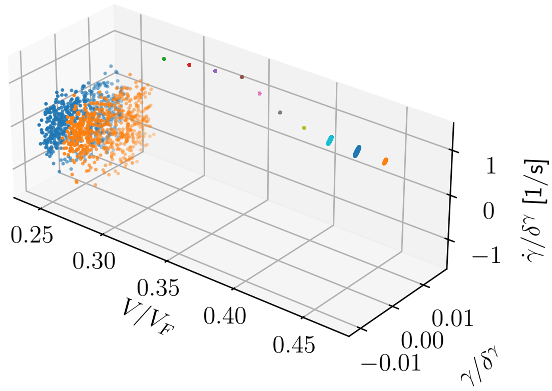

(a)

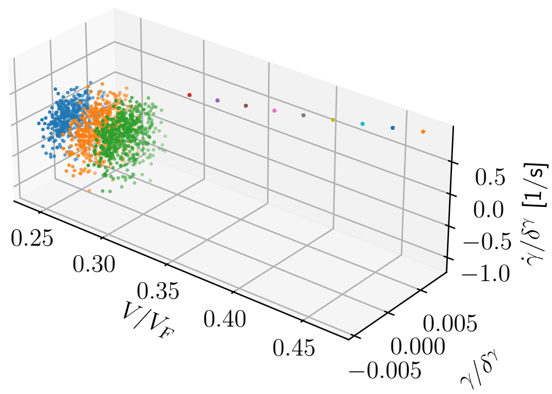

(b)

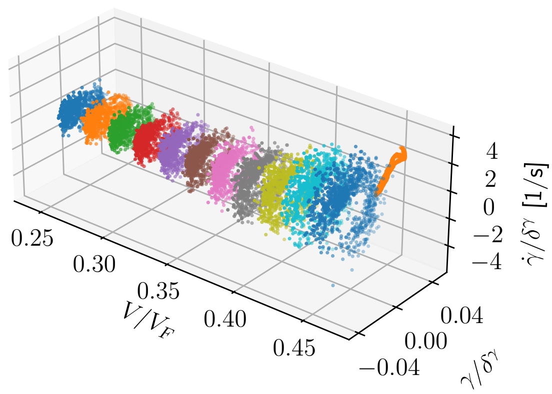

(c)

Figure 41 – Scenario *iii.*: Poincarè sections ($\dot{\beta} = \delta^{\beta}$ and $\dot{\beta} > 0$) for range between V^{γ}_{F2} and V^{γ}_{F3} (solutions obtained with initial conditions used when decreasing airspeed) for different freeplay ratio $R = \delta^{\gamma}/\delta^{\beta}$. (a) $R = 2$, (b) $R = 0.25$, (c) $R = 4$.

5.3.2 Initial Conditions

The bifurcation diagrams constructed by following the procedure described in section 3.3 consider the initial condition for the system evaluated in a parameter value depending on the last state of the solution for the previous parameter value. Then, the branch followed is defined by the initial solution chosen for the very first parameter (V_0). The maximum time defined by the user also has influence, since chaotic or quasi-periodic solutions are simulated until reaching the maximum time[I] and, therefore, different values defined can imply in different initial conditions for the next parameter. The diagrams in Fig. 37 are all constructed assuming $\gamma^0 = 0.5°$ when freeplay is present in tab, and $\beta^0 = 0.3°$ for scenario *i.* (the other states are zero). The maximum defined time is 70 s of time integration.

[I] The LCO is not identified by the LCO detector when chaotic or quasi-periodic solutions occur, and the time solution is not interrupted before maximum time.

A practical example of this influence can be shown for scenario i. The third airspeed simulated has time response oscillating inside the freeplay when $t = 70$ s (see Fig. 42a). However, note that $V/V_F = 2\% < V_{F1}^{\beta}$, and by checking the top-right V-g plot for the sub-system inside of CS, this particular airspeed belongs to a range where three different eigenvalues have real part quite close to zero (which indicate oscillations with amplitudes almost constant for the sub-linear system inside the freeplay). However, the eigenvalue represented by the green pentagon has real part actually positive and, although quite small, this positive value infers in growing oscillations inside the freeplay until eventually reaching the region outside the freeplay. Note by Fig. 42a that the maximum time 70 s does not allow the solution to reach the LCO with amplitude outside the freeplay and, therefore, the next airspeed parameter also uses an initial condition inside the freeplay. This condition goes on in a way that the branch of increasing airspeed shown in Fig. 37a is followed. On the other hand, if the simulation time is such that it allows the solution for the particular airspeed to reach the actual LCO highlighted in Fig. 42b, the branch followed is exactly the same of that one obtained when decreasing the airspeed (although it is omitted here).

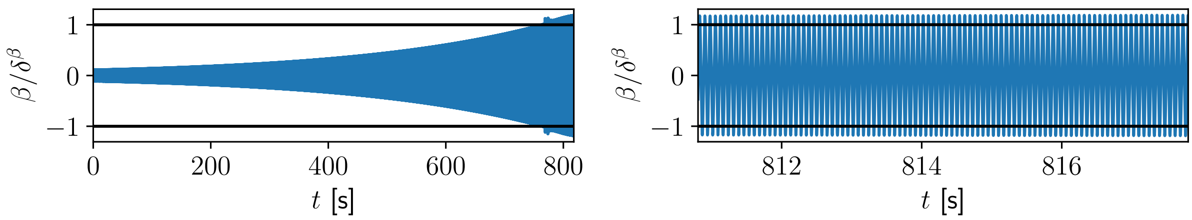

Figure 42 – Scenario $i.$: time solution for $V/V_F = 2\%$.

Another observation is that these two ways of constructing the bifurcation diagrams - increasing the airspeed starting from a very small value or decreasing the airspeed starting from a value close to flutter velocity of the nominal system - not necessarily allow to identify all LCOs. Note for scenario $ii.$ that a thorough investigation reveals a different LCO present in $21\% < V/V_F < 26\%$ not identified in any of those branches in Fig. 37c. This additional LCO is shown in phase portrait in Fig. 43a. Because of this missing LCOs, an interesting way of covering more LCO is integrating the system for four different initial conditions for each flight condition: each one activating a single structural mode of the nominal linear system. For a certain value V_i of the parameter V, the dynamic matrix for the nominal system is computed ($\mathbf{A}(V_i)$), and their eigenvalues and eigenvectors are extracted. In general, there are four complex eigenvalues (the conjugate pairs) referring to the structural degrees of freedom. Each single mode can be separately activated by considering an initial condition state vector in modal coordinates full of zeros, with 1 placed at the positions where a pair of conjugate eigenvalues appear. This strategy is used to more easily capture different types of LCO in a single parameter. However, it comes with the computational cost of running the simulations four times more. Actually, the diagrams in Fig. 37 basically miss the LCOs highlighted in Fig. 43, including two different ranges for scenario *ii.* only.

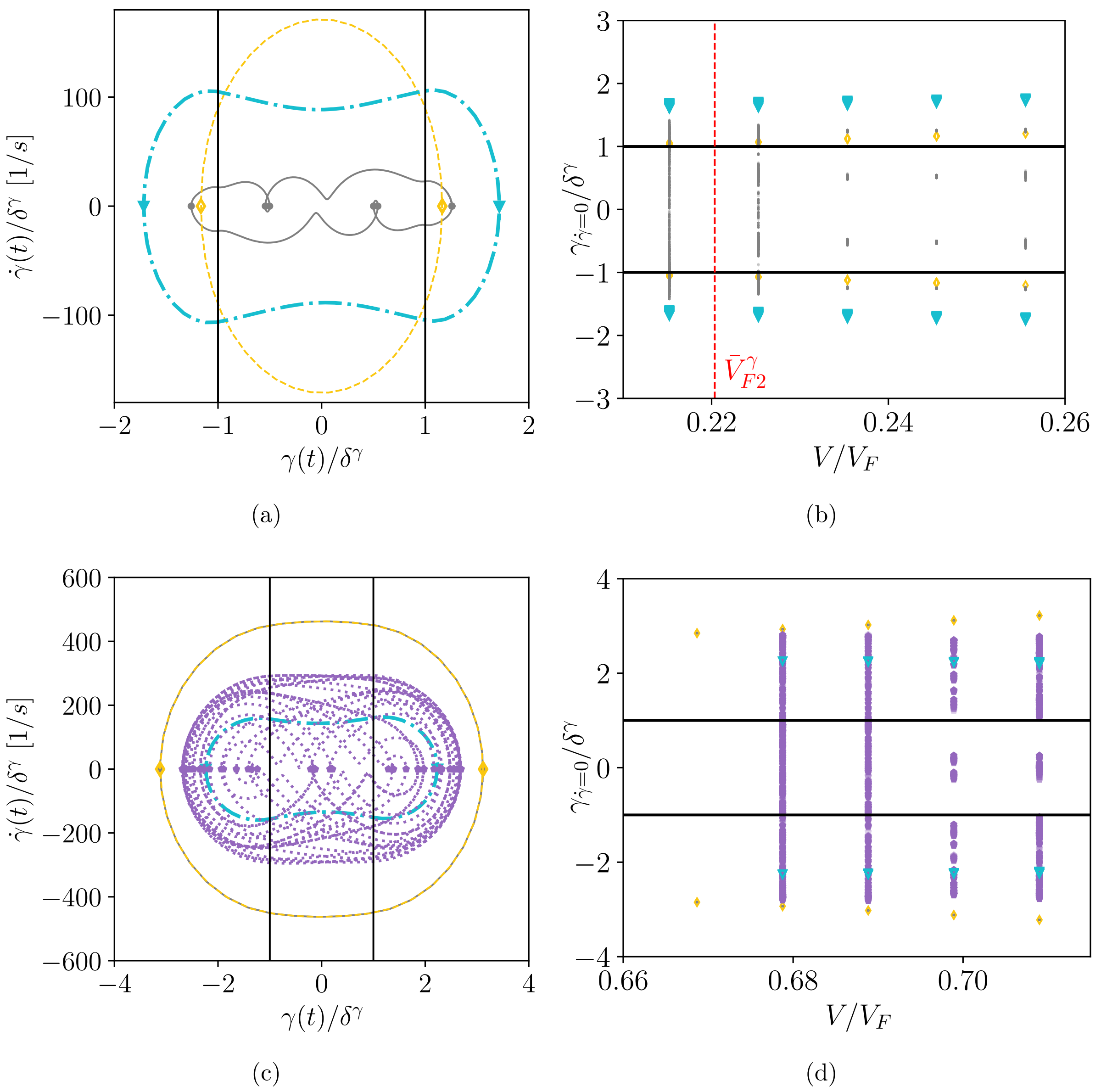

Figure 43 – Scenario *ii.*: portraits for (a) V/V_F = 25%, for (b) V/V_F = 70% and with LCO reached when increasing airspeed (gray circle, dashed line), decreasing (yellow diamond, solid line) and additional LCOs (other lines). (b) and (d) zoom of Fig. 37 with additional LCOs for two different ranges.

5.3.3 Phase Portraits and Frequency Bifurcation

The results corresponding to the analysis described by scenario i. present two types of LCO already discussed: the simple one with two inversion points and the more complex one, whose evolution is shown in Fig. 39 in terms of the phase portraits and spectral content. Regarding scenario ii. (Fig. 37c), a simple LCO is also obtained when decreasing the airspeed, but with a fundamental frequency f_1^{γ} close to the frequency of nominal flutter condition (f_F = 25.9 Hz), which is higher than the fundamental frequency of the simple LCO for scenario i. (see Fig. 44c and a). The smallest airspeed at which this simple LCO of scenario ii. appears is around V_{F2}^{γ}, with amplitude close to the freeplay boundary, and it keeps growing as the airspeed goes towards V_F. This evolution of the LCO indicated by yellow dashed line ( ) is shown in those phase portraits presented in Fig. 45. That figure also includes all LCO found for this scenario, where each phase portrait corresponds to a particular airspeed. In terms of frequency, Fig. 44c shows the effect of hysteresis when comparing increasing and decreasing direction, mainly at the range $V_{F2}^{\gamma} < V < V_{F3}^{\gamma}$. Note that the LCOs reached when increasing airspeed ( ) and when the additional search is performed ( ) can have a different but symmetrical LCO if simulated with an initial condition with opposite sign, particularly for phase portraits from V/V_F = 27.6 % to $V = V_{F3}^{\gamma}$. While shown in the Fig. 45, those symmetrical orbits are omitted from Fig. 39 for a cleaner visualization.

Regarding scenario iii., the evolution of the LCO in terms of airspeed is shown in Fig. 46. Its subfigure a. shows a LCO occuring for the range $\bar{V}_{F2}^{\gamma} < V/V_F < 36.5\%$ that is unique, i.e., even when simulated with the initial conditions with opposite sign, the LCO obtained is exactly the same. This LCO is not unique at $V/V_F \approx 36.5\%$, i.e., its symmetrical pair is achieved if the opposite sign is used for initial condition (Fig. 46b). This behavior explains the double branch of the bifurcation diagram (plots of Fig. 49), one indicating the response when $\mathbf{x}_0$ is the initial condition and the other one, when $-\mathbf{x}_0$ is used instead. This LCO persists until folds at V_{F3}^{γ}, where the unique LCO takes place (Fig. 46c). Finally, for speeds greater than V/V_F = 90%, different types of LCO appear until the speed gets close to V_F (see Fig. 47).

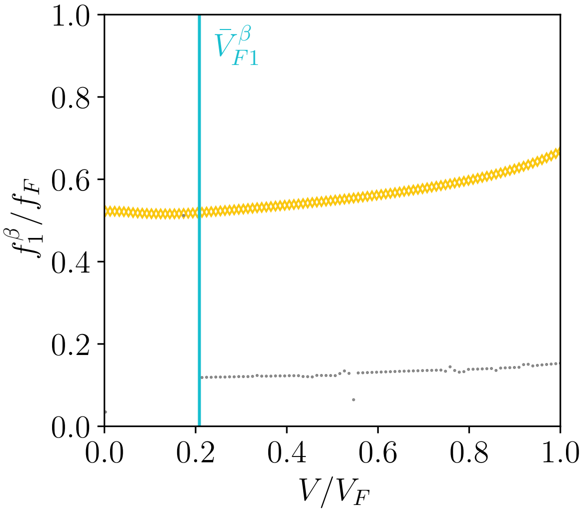

(a)

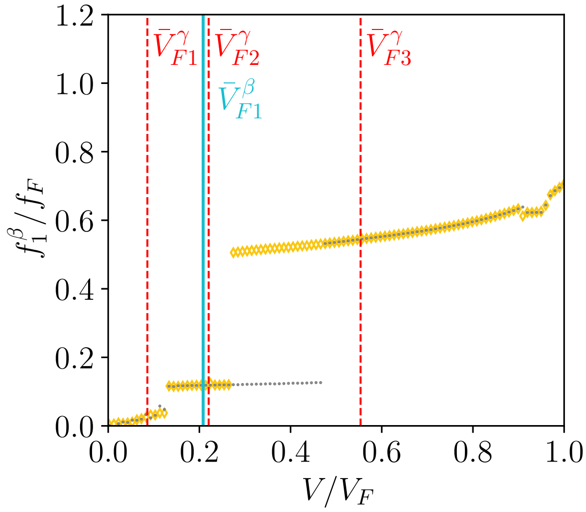

(b)

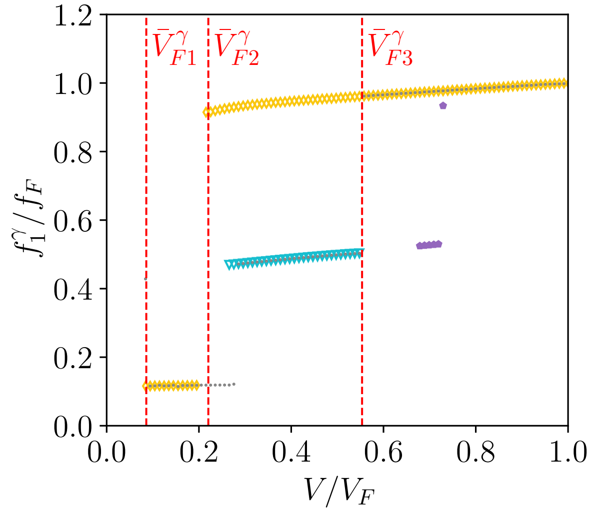

(c)

Figure 44 – Bifurcation diagrams for the fundamental frequency of CS and tab (f_1^{β} and f_1^{γ}) when increasing (gray dot) and decreasing (yellow diamond) the airspeed. (a) scenario *i.*; (c) scenario *ii.*; (b) scenario *iii.* (other symbols are for extra LCO found).

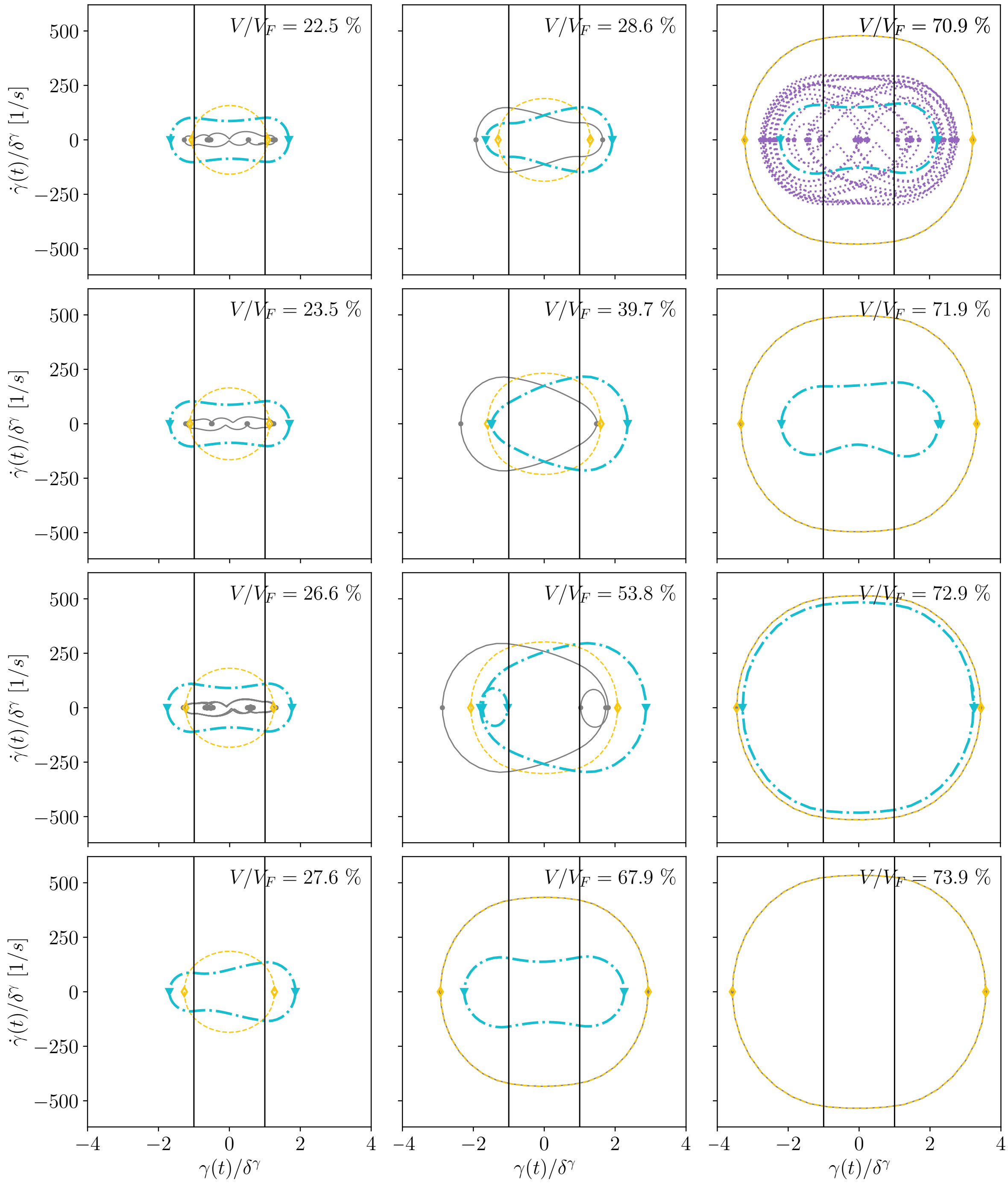

Figure 45 – Scenario *ii.*: phase space portrait for particular flight conditions (solid gray line - increasing airspeed; dashed yellow line - decreasing airspeed; other lines - found with the procedure involving modal initial conditions).

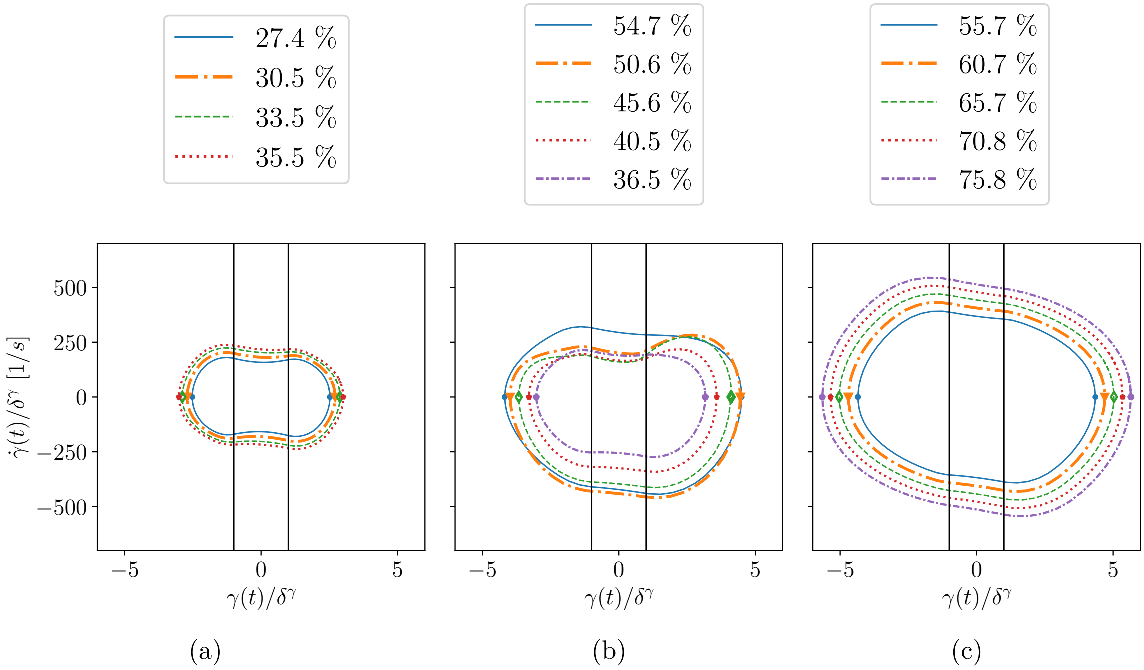

Figure 46 – Tab response for scenario *iii*. (freeplay in both hinges) at speeds for the range from V_{F2}^{γ} to V_{F3}^{γ} (left) and for the range from V_{F3}^{γ} to V_F (right).

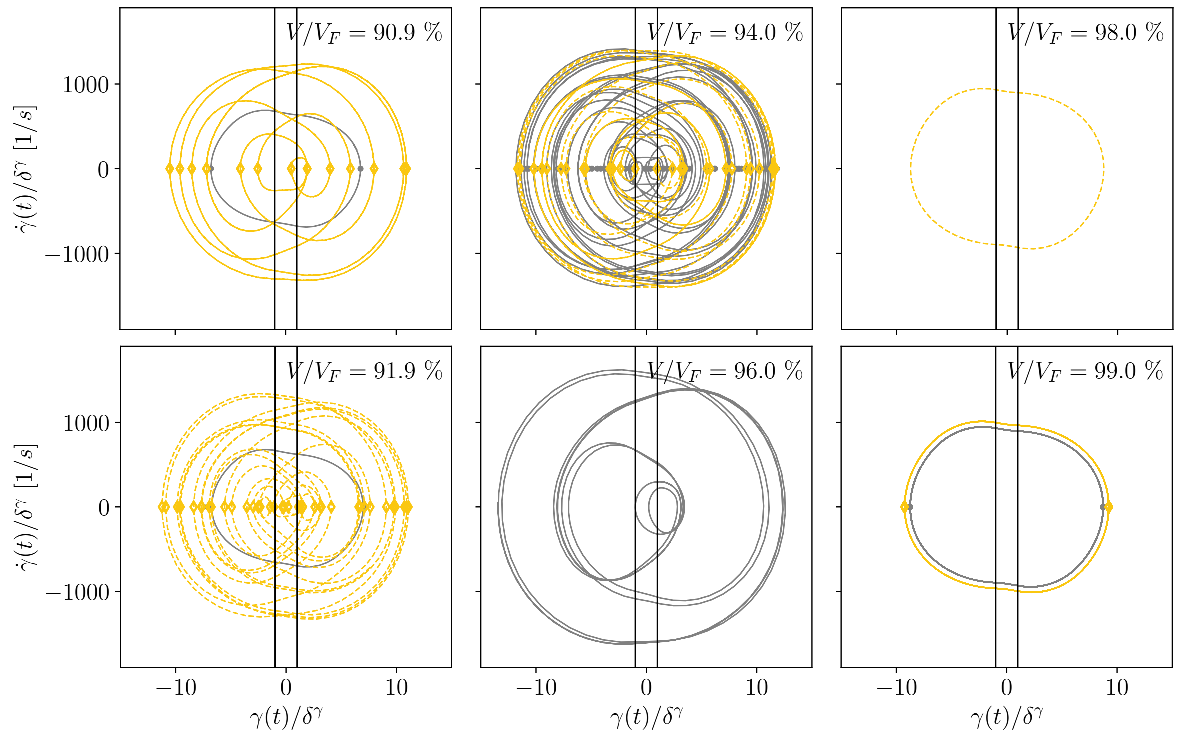

Figure 47 – Scenario *iii*.: phase space portrait for particular flight conditions (solid gray line - increasing airspeed; dashed yellow line - decreasing airspeed).

5.4 Final Direct Comparisions

Figure 48 shows the inversion points (top) and the frequency (bottom) for CS and tab comparing directly the scenario presenting freeplay in both hinges with the other ones presenting single freeplay. This figure omits the chaotic solutions to have a cleaner plot and includes the results for both increasing and decreasing directions, and also for the additional LCO found. Regarding the smallest airspeed for which LCO or quasi-periodic solutions are found, it needs to be any small amount larger than zero for scenario *i.*, whereas it is $V \approx V_{F2}^{\gamma}$ for scenario *ii.* and $V/V_F \approx 27.4\%$ for scenario *iii.*.

Comparing the results from scenario *iii.* with scenario *i.*, the maximum CS amplitudes for each flight condition are similar, in general. However, the upper side of the double branch has amplitudes slightly larger if freeplay is considered in both hinges (see right-hand side plot of Fig. 49). Also, the results from scenario *i.* present a larger range with more complex LCO, from $V/V_F \approx 48\%$ until V_F. No significant differences are found in the value of the fundamental frequency.

The comparison between scenarios *iii.* and *ii.* shows that the fundamental frequency is larger for scenario *ii.*, whereas scenario *iii.* clearly leads to LCO with amplitudes substantially larger than those from scenario *ii.*. For example, at $V/V_F = 52.6\%$, LCO for scenario *iii.* reaches tab amplitudes 1.6 times larger and CS amplitudes 3.5 times larger than those obtained from scenario *ii.* This is one of the most important conclusions of this study, highlighting the importance of considering freeplay in multiple degrees of freedom.

Regarding the describing function method, it works as described in chapter 4 for the cases with single freeplay. Note however, that pre-assumed motion with a single harmonic allows predicting the branches with the simplest LCO, and the results are not so rich when compared with those demonstrated in this chapter via time simulations. Also, for the case with multiple freeplays, a range of equivalent stiffness from 0 to the nominal value needs to be considered for both k_β and k_γ. However, there is not necessarily a LCO for each pair $(\hat{k}_\beta, \hat{k}_\gamma)$ resulting from the equivalent stiffness combination for both DOFs. Otherwise, it is equivalent to assume that all ratios of first harmonic amplitude U_β/U_γ exist, and this is not true. In this sense, Bai, Wu and Yang (2023) show an interesting approach to state how to use the information from an eigenvector to obtain a ratio U_β/U_γ and make it converges in an iterative method to the ratio assumed when relating the amplitude to the equivalent stiffness pair via describing function.

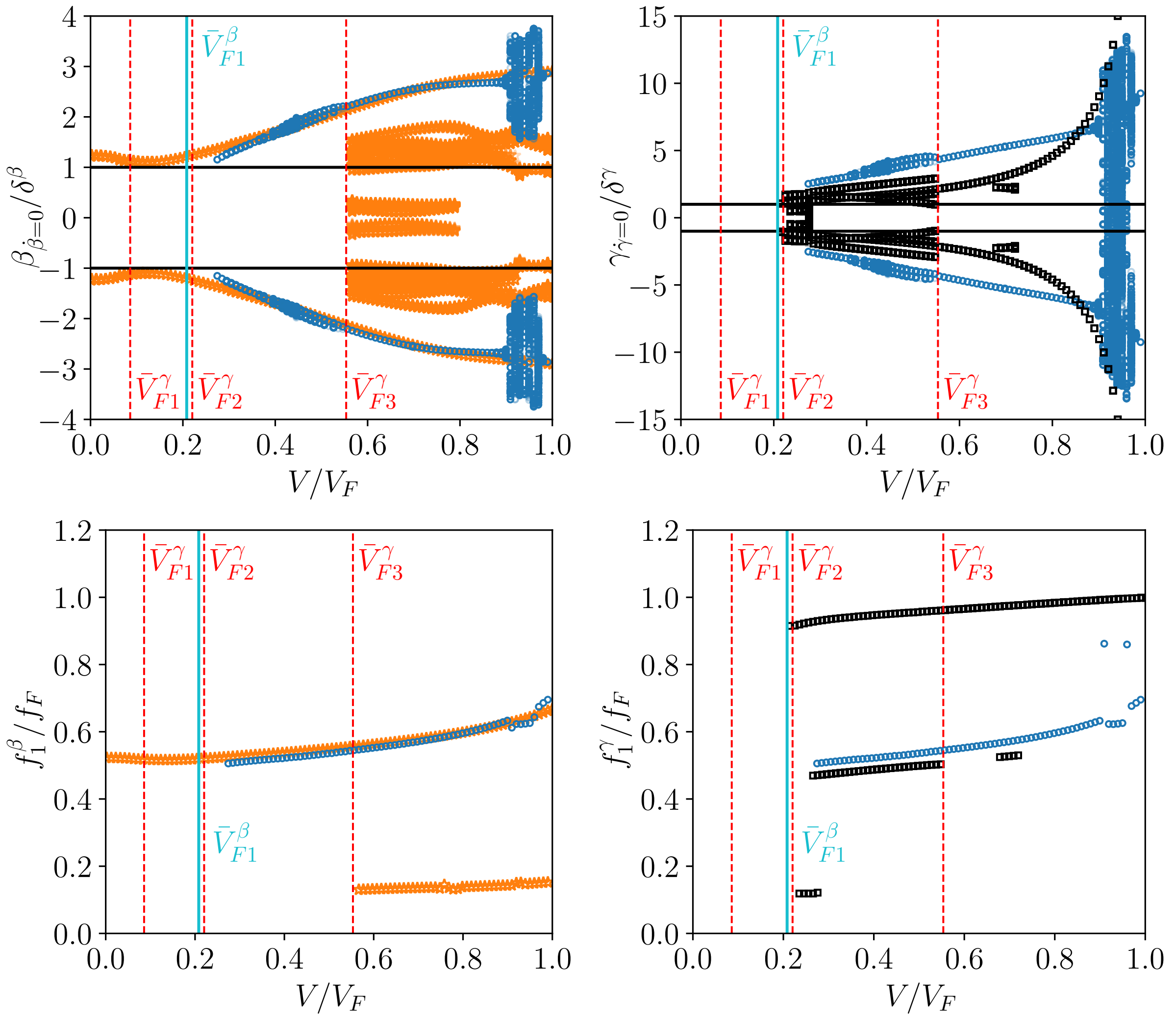

Figure 48 – Bifurcation diagram for the control surface and the tab inversion points ($\dot{\beta} = 0$ and $\dot{\gamma} = 0$) (top) and for fundamental frequency (bottom). Three scenarios of freeplay: *i.* CS only ($\star$); *ii.* tab only ($\square$); *iii.* both CS and tab (o). .

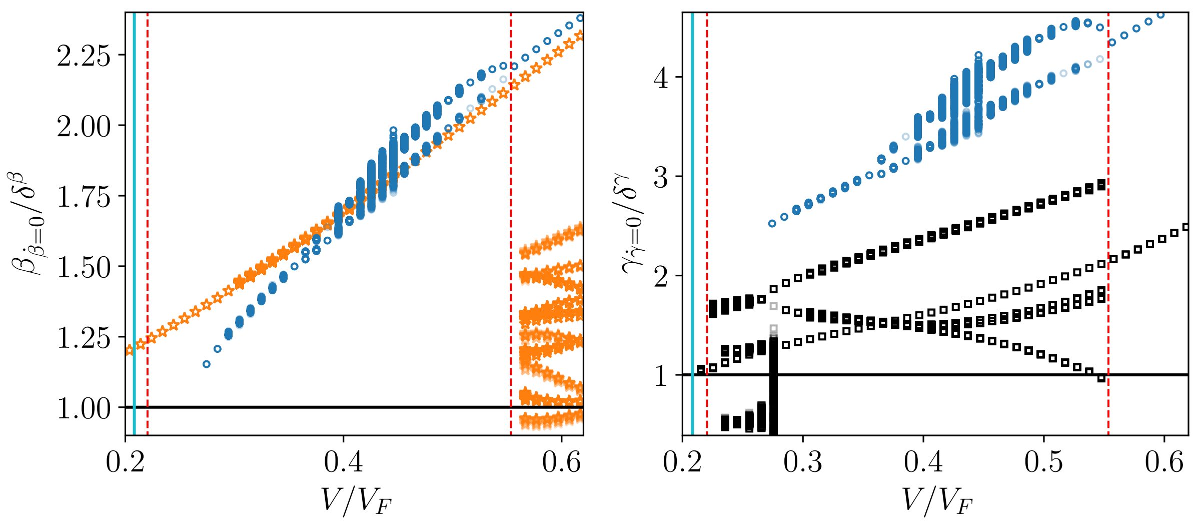

Figure 49 – Zoom of plots on top of Fig. 48.

6 Final Remarks

This work is focused on studying the limit cycle oscillations induced by freeplay in control surfaces. These oscillations can cause failure related to fatigue due to repetitive motion. Also, certification agencies such as the Federal Aviation Administration (FAA) indicates that it is necessary to consider nonlinearities in aeroelasticity, and the regulations mentions particularly freeplay. Therefore, contributions in the field are considered undoubtedly important.

Nonlinearities in general require different procedures during the numerical analysis. However, particularly those which are discontinuous, such as the freeplay, include additional issues to employ conventional numerical methods. In this context, the thesis defended in this research is: "*Alternative approaches for predicting limit cycle oscillations induced by control surface freeplay can contribute to understand the physics associated to this nonlinearity.*" Particularly, the work provides improvements in the Hénon's technique to perform time marching; and also introduces new describing functions to predict LCOs in the frequency domain. The introduced theoretical approaches allow one to show the influence of considering combined discontinuous nonlinearities, such as asymmetric freeplay, freeplay/friction and freeplay/freeplay.

The main contributions related to time integration methods include the development of a mathematical formulation in matrix form for the Hénon's technique using a general notation to include any discontinuous nonlinearity acting on an arbitrary degree of freedom. Also, a new generalized coordinates system is proposed to keep the state with the nonlinearity with physical unity to simplify the use of the Hénon's technique. Furthermore, the proposed technique is exposed in a way to be applied as an event location technique and it is particularly used in this research to capture the inversion points (extreme) during the integration. The strategy was useful to the LCO detection and also to produce data used to construct bifurcation diagrams, which are a typical qualitative tool of post-processing analysis of nonlinear systems.

Regarding the LCO prediction in frequency domain, the work provides two main contributions involving new describing functions to be combined with the classical linear stability analysis based on eigenvalues of a linear equivalent dynamic matrix. The new way of looking at the describing function (DF) is proposed with a general notation to consider any harmonic in the LCO. The idea behind it is similar to that one involved in the Harmonic Balance method, from where the classic DF to freeplay (first harmonic only) is derived. Particularly, the first application in this work considers the first and third harmonics. Another novelty in this aspect is a describing function developed to consider both freeplay and friction acting on a single degree of freedom. The equivalent friction force is considered proportional to the velocity by means of a linear equivalent viscous damping. The proposed solution with this new DF for friction requires an iterative procedure to apply the eigenvalue analysis, which was detailed in this present work.

The proposed improvements over conventional numerical methods open possibilities of studying the physical effects of combined discontinuous nonlinearities. As a first application, both time and frequency domains are considered respectively using the described Hénon's technique and the new DF to study the 3-DOF airfoil with freeplay and Coulomb friction in the control surface hinge. Results show that the friction force can reduce the frequency of a LCO, but with slight differences in relation to the no friction condition. Although it has a dissipative nature, this force is not enough to suppress the limit cycle when levels related to typical linear damping ratio (until ~ 4%) are used. On the other hand, the level of friction may modify the spectrum of the system response, introducing different harmonics. Also, the extremes of a LCO can be changed depending on the level of the freeplay asymmetry. This is an important aspect to be considered because the freeplay amplitude can change during the aircraft operation.

The second application described herein employs the Hénon's technique in time marching to explore the 4-DOF airfoil with freeplay in two different moving parts, i.e., main control surface (CS) and a tab. A complete study is performed, starting from constructing the V-g-f diagram (eigenvalue analysis) of the four sub-linear systems involved when two freeplays are present. The marginally stable conditions of all these systems are quite related to changes in stability of the corresponding nonlinear system, that is discussed using bifurcation diagrams of the nonlinear DOFs extremes against the airspeed. Poincarè sections are also used to show the effect of freeplay ratio between CS and tab on the transition from chaotic solutions to quasi-periodic and also to LCO. Phase portraits are also used to show the several different LCO that may exist in a single flight condition. The scenario when freeplay is considered in both moving parts (scenario *iii.*) is compared with the cases of single freeplay (scenario *i.*: on CS only, and scenario *ii.*:

on tab only). Besides considerable differences in the number and complexity of LCOs, although the CS amplitude levels are quite similar between scenarios *i.* and *iii.*, the tab amplitudes can be clearly larger when these two freeplay are considered, if compared with a single freeplay in tab. This is a relevant finding to demonstrate that aeroelastic analysis also needs to consider more than a single moving part with freeplay to properly characterize limit cycle oscillations.

6.1 Suggestions for Future Work

Future works can consider the new approaches presented herein to conduct further studies, as listed below.

- investigate the 4-DOF airfoil with both freeplay and friction acting on the two moving parts (CS and tab), utilizing the Hénon's technique for time marching analysis;
- construct bifurcation diagrams for the system with two freeplays using the Numerical Continuation shooting method (DIMITRIADIS, 2017a), which is valuable for identifying folding points and characterizing the system stability. Shooting methods employ a time marching approach and can leverage the Hénon's technique adapted in this work to include multiple nonlinearities;
- apply the Describing Function method to identify LCO for the system with two freeplays. The new look at the Equivalent Linearization Technique, as described in this work, is applicable to this scenario. An iterative process, similar to the one employed for freeplay and friction, may be utilized to achieve convergence between assumed LCO amplitudes and eigenvector information extracted from the equivalent dynamic matrix;
- utilize the Hénon's technique and the novel interpretation of the Equivalent Linearization Technique, as outlined in this work, to investigate aeroelastic systems with different forms of discontinuous nonlinearities, such as bilinear stiffness or hysteresis.

REFERENCES

ABDELKEFI, A.; VASCONCELLOS, R.; MARQUES, F. D.; HAJJ, M. R. Modeling and identification of freeplay nonlinearity. **Journal of Sound and Vibration**, v. 331, p. 1898--1907, 2012.

ABELL, M. L.; BRASELTON, J. P. Chapter 8 - introduction to the laplace transform. In: **Introductory Differential Equations**. Fifth edition. Academic Press, 2018. p. 399--460. ISBN 978-0-12-814948-5. Available from: https://www.sciencedirect.com/science/article/pii/B9780128149485000082.

AL-MASHHADANI, W. J.; DOWELL, E. H.; WASMI, H. R.; AL-ASADI, A. A. Aeroelastic response and limit cycle oscillations for wing-flap-tab section with freeplay in tab. **Journal of Fluids and Structures**, v. 68, p. 403 -- 422, 2017. ISSN 0889-9746.

ANDERSON, W. D.; MORTARA, S. Maximum control surface freeplay, design and flight testing approach on the f-22. In: **AIAA Paper 07-1767, AIAA/ASME/ASCE/AHS/ASC Structures, Structural Dynamics, and Materials Conference**. [S.l.: s.n.], 2007.

ARÉVALO, F. **Aeroelasticidad de una aeronave en presencia de nolinealidades estructurales concentradas**. Thesis (Ph. D.) --- Escuela Técnica Superior de Ingenieros Aeronáuticos ETSIA, Universidad politécnica de Madrid UPM, 2008.

ARÉVALO, F.; GARÍA-FOGEDA, P.; CLIMENT, H. Nonlinear time-domain structure/aerodynamics coupling in systems with concentrated structural nonlinearities. In: **Proceedings of 27th International congress of the aeronautical sciences**. [S.l.: s.n.], 2010.

AWREJCEWICZ, J.; OLEJNIK, P. Numerical analysis of self-excited by friction chaotic oscillations in two-degrees-of-freedom system using exact henon method. **Machine Dynamics Problems**, v. 26, n. 4, p. 9--20, 2002.

BAI, L.; WU, Z.; YANG, C. Nonlinear aeroelastic characteristics of a supersonic all-movable fin with single or multiple freeplay nonlinearities. **Applied Sciences**, v. 13, p. 1262, 01 2023.

BLOCK, J. J.; STRGANAC, T. W. Applied active control for a nonlinear aeroelastic structure. **Journal of Guidance, Control, and Dynamics**, v. 21, n. 6, p. 838--845, 1998.

BREITBACH, E. Effect of structural non-linearities on aircraft vibration and flutter. **Advisory Group for Aerospace Research & Development - AGARD**, n. 665, Feb. 1978.

BREITBACH, E. J. Flutter analysis of an airplane with multiple structural nonlinearities in the control system. **National Aeronautics and Space Administration - NASA**, n. 1620, 1980.

BUENO, D. D.; DOWELL, E. H. A note on the state space representation of aeroelastic systems for time domain analysis. **Journal of Fluids and Structures**, v. 104, p. 103294, 2021. ISSN 0889-9746.

BUENO, D. D.; GÓES, L. C. S.; GONÇALVES, P. J. P. Control of limit cycle oscillation in a three degrees of freedom airfoil section using fuzzy takagi-sugeno modeling. **Shock and Vibration**, v. 2014, June 2014.

BUENO, D. D.; GÓES, L. C. S.; GONÇALVES, P. J. P. Flutter analysis including structural uncertainties. **Meccanica**, v. 50, n. 8, p. 2093--2101, 2015.

BUENO, D. D.; WAYHS-LOPES, L. D.; DOWELL, E. H. Control-surface structural nonlinearities in aeroelasticity: A state of the art review. **AIAA Journal**, v. 60, n. 6, p. 3364--3376, 2022.

CHEN, P.; LEE, D.; LIU, D. Flight-loads effects on free-play induced limit cycle oscillation. **Collection of Technical Papers - AIAA/ASME/ASCE/AHS/ASC Structures, Structural Dynamics and Materials Conference**, v. 5, 01 2006.

CHUNG, K.; CHAN, C.; LEE, B. Bifurcation analysis of a two-degree-of-freedom aeroelastic system with freeplay structural nonlinearity by a perturbation-incremental method. **Journal of Sound and Vibration**, v. 299, n. 3, p. 520 -- 539, 2007. ISSN 0022-460X.

CONNER, M. D.; TANG, D. M.; DOWELL, E. H.; VIRGIN, L. N. Nonlinear behavior of a typical airfoil section with control surface freeplay: a numerical and experimental study. **Journal of Fluids and Structures**, Elsevier, v. 11, n. 1, p. 89--109, 1997.

CONNER, M. D.; VIRGIN, L. N.; DOWELL, E. H. Accurate numerical integration on state-space models for aeroelastic systems with freeplay. **AIAA Journal**, American Institute of Aeronautics and Astronautics, v. 34, n. 10, p. 2202--2205, 1996.

DAI, H.; YUE, X.; YUAN, J.; ATLURI, S. A time domain collocation method for studying the aeroelasticity of a two dimensional airfoil with a structural nonlinearity. **Journal of Computational Physics**, v. 270, p. 214–237, 08 2014.

DAI, H.; YUE, X.; YUAN, J.; XIE, D.; ATLURI, S. A comparison of classical runge-kutta and henon?s methods for capturing chaos and chaotic transients in an aeroelastic system with freeplay nonlinearity. **Nonlinear Dynamics**, v. 81, n. 1-2, p. 169--188, 2015.

DIMITRIADIS, G. Bifurcation analysis of aircraft with structural nonlinearity and freeplay using numerical continuation. **Journal of Aircraft**, v. 45, n. 3, p. 893--905, 2008.

DIMITRIADIS, G. Continuation of higher-order harmonic balance solutions for nonlinear aeroelastic systems. **Journal of Aircraft**, v. 45, p. 523--537, 03 2008.

DIMITRIADIS, G. Chapter 7 - numerical continuation. In: **Introduction to Nonlinear Aeroelasticity**. [S.l.]: John Wiley & Sons, 2017. (Wiley Aerospace series), p. 314--316. ISBN 9781118613474.

DIMITRIADIS, G. **Introduction to Nonlinear Aeroelasticity**. [S.l.]: John Wiley & Sons, 2017. (Wiley Aerospace series). ISBN 9781118613474.

DOWELL, E.; EDWARDS, J.; STRGANAC, T. Nonlinear aeroelasticity. **Journal of Aircraft**, v. 40, n. 5, p. 857--874, 2003.

DOWELL, E.; TANG, D. Nonlinear aeroelasticity and unsteady aerodynamics. **AIAA Journal**, v. 40, p. 1697--1707, 01 2002.

EDWARDS, J. W. **Unsteady aerodynamic modeling and active aeroelastic control**. Thesis (Ph. D.) --- Stanford University, 1977.

ELLER, D. Friction, freeplay and flutter of manually controlled aircraft. In: **IFASD - International Forum on Aeroelasticity and Structural Dynamics**. [S.l.: s.n.], 2007.

GERALD, C.; WHEATLEY, P. **Applied Numerical Analysis**. Addison-Wesley Publishing Company, 1994. (Addison-Wesley world student series). ISBN 9780201565539. Available from: https://books.google.com.br/books?id=bg7vAAAAMAAJ.

GORDON, J.; MEYER, E.; MINOGUE, R. Nonlinear stability analysis of control surface flutter with free-play effects. **Journal of Aircraft**, v. 45, n. 6, p. 1904--1916, 11 2008.

HARTOG, J. D. Forced vibrations with combined coulomb and viscous friction: Apm-53-9. **Trans ASME**, v. 15, n. 107, 1931.

HARTOG, J. D. **Mechanical Vibrations**. [S.l.]: Dover Publications, 1985. (Civil, Mechanical and Other Engineering Series). ISBN 9780486647852.

HE, S.; GUO, S.; LI, W.; YANG, D.; GU, Y.; YANG, Z. Nonlinear aeroelastic behavior of an airfoil with free-play in transonic flow. **Mechanical Systems and Signal Processing**, v. 138, p. 106539, 2020. ISSN 0888-3270.

HE, S.; YANG, Z.; GU, Y. Nonlinear dynamics of an aeroelastic airfoil with free-play in transonic flow. **Nonlinear Dynamics**, v. 87, n. 4, p. 2099--2125, 11 2017.

HENON, M. On the numerical computation of Poincaré maps. **Physica D: Nonlinear Phenomena**, Elsevier, v. 5, n. 2-3, p. 412--414, 1982.

KHOLODAR, D. Nature of freeplay-induced aeroelastic oscillations. **Journal of Aircraft**, v. 51, p. 571--583, 01 2014.

KHOLODAR, D.; DICKINSON, M. Aileron freepaly. In: **International Forum of Aeroelasticity and Structural Dynamics - IFASD**. [S.l.: s.n.], 2010.

KUZNETSOV, Y. A. **Elements of applied bifurcation theory**. 2. ed. Berlin: Springer, 1998. (Applied Mathematical Sciences, 112). ISBN 978-0387983820.

LAURENSON, R. M.; TRN, R. M. Flutter analysis of missile control surfaces containing structural nonlinearities. **AIAA Journal**, v. 18, n. 10, p. 1245--1251, 1980.

LEE, B.; PRICE, S.; WONG, Y. Nonlinear aeroelastic analysis of airfoils: bifurcation and chaos. **Progress in Aerospace Sciences**, v. 35, n. 3, p. 205 -- 334, 1999. ISSN 0376-0421.

LEE, C. L. An iterative procedure for nonlinear flutter analysis. **AIAA Journal**, v. 24, n. 5, p. 833--840, 1986.

LEE, D.-H.; CHEN, P.; TANG, D.; DOWELL, E. Nonlinear gust response of a control surface with free-play. In: **51st AIAA/ASME/ASCE/AHS/ASC Structures, Structural Dynamics, and Materials Conference**. [S.l.: s.n.], April 2010. AIAA 2010-3116.

LI, D.; GUO, S.; XIANG, J. Aeroelastic dynamic response and control of an airfoil section with control surface nonlinearities. **Journal of Sound and Vibration**, Elsevier, v. 329, n. 22, p. 4756--4771, 2010.

LIU, L.; DOWELL, E. Harmonic balance approach for an airfoil with a freeplay control surface. **AIAA Journal**, American Institute of Aeronautics and Astronautics, v. 43, n. 4, p. 802--815, 2005.

LIU, L.; DOWELL, E.; THOMAS, J. Higher order harmonic balance analysis for limit cycle oscillations in an airfoil with cubic restoring forces. In: **46th AIAA/ASME/ASCE/AHS/ASC Structures, Structural Dynamics and Materials Conference**. [S.l.: s.n.], 2005. AIAA 2005-1918.

LIU, L.; WONG, Y.; LEE, B. Application of the centre manifold theory in non-linear aeroelasticity. **Journal of Sound and Vibration**, v. 234, n. 4, p. 641 -- 659, 2000. ISSN 0022-460X.

LIU, L.; WONG, Y.; LEE, B. Non-linear aeroelastic analysis using the point transformation method, part 1: Freeplay model. **Journal of Sound and Vibration**, v. 253, n. 2, p. 447 -- 469, 2002. ISSN 0022-460X.

LIU, Y.; LI, J.; ZHANG, Z.; HU, X.; ZHANG, W. Experimental comparison of five friction models on the same test-bed of the micro stick-slip motion system. **Mechanical Science**, n. 5, p. 15--28, 2015.

NAYFEH, A.; MOOK, D. **Nonlinear Oscillations**. [S.l.]: John Wiley & Sons, Ltd, 1979. ISBN 9780471035558.

PADMANABHAN, M.; DOWELL, E. Calculation of aeroelastic limit cycles due to localized nonlinearity and static preload. **AIAA Journal**, v. 55, n. 8, p. 2762--2772, 06 2017.

PADMANABHAN, M.; DOWELL, E.; PASILIAO, C. Computational study of aeroelastic limit cycles due to localized structural nonlinearities. **Journal of Aircraft**, v. 55, n. 4, p. 1531--1541, 01 2018.

PRICE, S.; ALIGHANBARI, H.; LEE, B. The aeroelastic response of a two-dimensional airfoil with bilinear and cubic structural nonlinearities. **Journal of Fluids and Structures**, v. 9, n. 2, p. 175 -- 193, 1995. ISSN 0889-9746.

RIBEIRO, F. A.; DOWELL, E. H.; BUENO, D. D. Enhancement to least square-based approach for time-domain unsteady aerodynamic approximation. **Journal of Aircraft**, v. 58, n. 1, p. 111--124, 2021.

RODRIGUES, D. L.; DOWELL, E. H.; BUENO, D. D. On the stiffness and damping characteristics of magnetorheological dampers and their implications for flutter analysis. **Engineering Research Express**, IOP Publishing, v. 2, n. 1, p. 015049, mar 2020. Available from: https://dx.doi.org/10.1088/2631-8695/ab7dd6.

ROGER, K. Airplane math modelling methods for active control design. **AGARD Conference Proceeding**, v. 9, p. 4.1--4.11, 1977.

SCHNEIDER, G.; MARTIN, T. Memorandum, **Policy for Certification and Continued Airworthiness of Unbalanced and Mass-Balanced Control Surfaces, FAA Federal Aviation Administration, Department of Transportation USA**. Nov. 2007.

SHEN, S. F. An approximate analysis of nonlinear flutter problem. **Journal of the Aerospace Sciences**, v. 26, n. 1, p. 25--32, 1959.

SILVA, J. A. I. da; MARQUES, F. D. Characterization of typical aeroelastic sections under combined structural concentrated nonlinearities. **Journal of Vibration and Control**, v. 28, n. 13-14, p. 1739--1753, 2022.

TAMURA, H.; TSUDA, Y.; SUEOKA, A. Higher approximation of steady oscillations in nonlinear systems with single degree of freedom: Suggested multi-harmonic balance method. **Bulletin of JSME**, v. 24, p. 1616--1625, 09 1981.

TANG, D.; DOWELL, E. Aeroelastic response induced by free play, part 1: Theory. **AIAA Journal**, v. 49, p. 2532--2542, 11 2011.

TANG, D.; DOWELL, E. Experimental aeroelastic response for a freeplay control surface in buffeting flow. **AIAA Journal**, v. 51, p. 2852--2861, 12 2013.

TANG, D.; DOWELL, E. H. Flutter and limit-cycle oscillations for a wing-store model with freeplay. **Journal of Aircraft**, v. 43, n. 2, p. 487--503, 2006.

TANG, D.; DOWELL, E. H.; VIRGIN, L. N. Limit cycle behaviour of an airfoil with a control surface. **Journal of Fluids and Structures**, v. 12, p. 839--858, 1998.

TANG, D.; KHOLODAR, D.; DOWELL, E. H. Nonlinear response of airfoil section with control surface freeplay to gust loads. **AIAA Journal**, v. 38, n. 9, p. 1543--1557, 2000.

THEODORSEN, T. General theory of aerodynamic instability and the mechanism of flutter. **NACA Rept. 496**, v. 13, p. 374--387, 1935.

THEODORSEN, T.; GARRICK, I. Non-stationary flow about a wing-aileron-tab combination including aerodynamic balance. **NACA Rept. 736**, p. 132--138, 1942.

TIAN, W.; YANG, Z.; GU, Y. Dynamic analysis of an aeroelastic airfoil with freeplay nonlinearity by precise integration method based on padé approximation. **Nonlinear Dynamics**, v. 89, n. 3, p. 2173--2194, Aug 2017. ISSN 1573-269X.

TRICKEY, S.; VIRGIN, L.; DOWELL, E. The stability of limit--cycle oscillations in a nonlinear aeroelastic system. **Proceedings of the Royal Society of London. Series A: Mathematical, Physical and Engineering Sciences**, The Royal Society, v. 458, n. 2025, p. 2203--2226, 2002.

VASCONCELLOS, R.; ABDELKEFI, A.; HAJJ, M.; MARQUES, F. Grazing bifurcation in aeroelastic systems with freeplay nonlinearity. **Communications in Nonlinear Science and Numerical Simulation**, v. 19, n. 5, p. 1611 -- 1625, 2014. ISSN 1007-5704.

VASCONCELLOS, R.; ABDELKEFI, A.; MARQUES, F. D.; HAJJ, M. R. Representation and analysis of control surface freeplay nonlinearity. **Journal of Fluids and Structures**, v. 31, p. 79--91, 2012.

VERSTRAELEN, E.; DIMITRIADIS, G.; ROSSETTO, G. D. B.; DOWELL, E. H. Two-domain and three-domain limit cycles in a typical aeroelastic system with freeplay in pitch. **Journal of Fluids and Structures**, v. 69, p. 89 -- 107, 2017. ISSN 0889-9746.

VIO, G. A.; COOPER, J. E. Limit cycle oscillation prediction for aeroelastic systems with discrete bilinear stiffness. **International Journal of Applied Mathematics and Mechanics**, v. 3, p. 100--119, 2005.

VISHAL, S.; RAAJ, A.; BOSE, C.; J., V. Routes to synchronization in a pitch–plunge aeroelastic system with coupled structural and aerodynamic nonlinearities. **International Journal of Non-Linear Mechanics**, v. 135, p. 103766, 2021. ISSN 0020-7462.

VISHAL, S.; RAAJ, A.; BOSE, C.; VENKATRAMANI, J.; DIMITRIADIS, G. Numerical investigation into discontinuity-induced bifurcations in an aeroelastic system with coupled non-smooth nonlinearities. **Nonlinear Dynamics**, v. 108, n. 4, p. 3025--3051, 2022.

WAYHS-LOPES, L. D.; DOWELL, E. H.; BUENO, D. D. Influence of friction and asymmetric freeplay on the limit cycle oscillation in aeroelastic system: An extended hénon's technique to temporal integration. **Journal of Fluids and Structures**, v. 96, p. 103054, 2020. ISSN 0889-9746.

WAYHS-LOPES, L. D.; DOWELL, E. H.; BUENO, D. D. A new look at the equivalent linearization technique to predict lco in aeroelastic systems with discrete nonlinearities. **Journal of Fluids and Structures**, v. 119, p. 103867, 2023. ISSN 0889-9746.

WENZINGER, C. J. Notes on tabs. **Journal of the Aeronautical Sciences**, v. 4, n. 9, p. 386--389, 1937.

WOOLSTON, D. S.; RUYAN, H. L.; ANDREWS, R. E. An investigation of effects of certain types of structural nonhnearities on wing and control surface flutter. **Journal of the Aeronautical Sciences**, v. 24, n. 1, p. 57--63, 1957.

WOOLSTON, D. S.; RUYAN, H. L.; BYRDSONG, T. A. Some effects of system nonlinearities in the problem of aircraft flutter. **Technical Note 3539, National Advisory Committee for Aeronautics (NACA), USA, Langley Aeronautical Laboratory, Washington.**, 1955. Available from: https://ntrs.nasa.gov/search.jsp?R=19930084263.

YANG, Z.; HE, S.; GU, Y. Transonic limit cycle oscillation behavior of an aeroelastic airfoil with free-play. **Journal of Fluids and Structures**, v. 66, p. 1 -- 18, 2016. ISSN 0889-9746.

YANG, Z.; ZHAO, L. Analysis of limit cycle flutter of an airfoil in incompressible flow. **Journal of Sound and Vibration**, v. 123, n. 1, p. 1 -- 13, 1988. ISSN 0022-460X.

YEH, G. C. K. Forced vibrations of a two-degree of freedom system with combined coulomb and viscous damping. **The Journal of the Acoustical Society of America**, n. 39, 1966.

YU, Q.; DAMODARAN, M.; KHOO, B. Nonlinear aeroelastic analysis of a multi-element airfoil with free play using continuation method. **Journal of Fluids and Structures**, v. 109, p. 103482, 2022. ISSN 0889-9746. Available from: https://www.sciencedirect.com/science/article/pii/S0889974621002371.

YUAN, W.; ZHANG, X.; POIREL, D. C. Flutter analysis solution stabilization for the pk-method. In: **AIAA AVIATION 2021 FORUM**. [S.l.: s.n.], Aug. 2021. AIAA Paper 2021-2473.

ZHANG, H.; WU, J. The aeroelastic characteristic of a wing with preload asymmetry freeplay. **Procedia Engineering**, v. 99, p. 51 -- 56, 2015.

APPENDIX A – Matrices of Theodorsen Formulation

This appendix shows the state space matrices; the mass and stiffness matrices for the 3-DOF and 4-DOF airfoil of Theodorsen (1935), the particular equations for inertia and static moments of mass given the masses and the geometrical parameters for each part of the airfoil. The aerodynamic matrices involved in Theodorsen's formulation are also presented, as well the method of Roger (1977) used to approximate the aerodynamics to be used in time domain.

A.1 State Space Matrices

The aeroelastic dynamic matrix (Eq. 22) of the overlying system (outside of freeplay, with nominal stiffness) and submatrices (Eq. 23) used to define the state space model.

$$\mathbf{A} = \begin{bmatrix} [\bar{\mathbf{A}}]_{2n_{\mathrm{dof}}\times 2n_{\mathrm{dof}}} & [\bar{\mathbf{Q}}]_{2n_{\mathrm{dof}}\times n_{\mathrm{lag}}n_{\mathrm{dof}}} \\ [\bar{\mathbf{IO}}]_{n_{\mathrm{lag}}n_{\mathrm{dof}}\times 2n_{\mathrm{dof}}} & [\bar{\mathbf{\Gamma}}]_{n_{\mathrm{lag}}n_{\mathrm{dof}}\times n_{\mathrm{lag}}n_{\mathrm{dof}}} \end{bmatrix}_{N\times N} \tag{22}$$

$$\bar{\mathbf{A}} = \begin{bmatrix} -\mathbf{M}_a^{-1}\mathbf{D}_a & -\mathbf{M}_a^{-1}\mathbf{K}_a \\ \mathbf{I}_{n_{\mathrm{dof}}} & \mathbf{0}_{n_{\mathrm{dof}}} \end{bmatrix} \quad \bar{\mathbf{Q}} = \begin{bmatrix} q\mathbf{M}_a^{-1}\mathbf{Q}_{1+2} & \cdots & q\mathbf{M}_a^{-1}\mathbf{Q}_{(n_{\mathrm{lag}}+2)} \\ \mathbf{0}_{n_{\mathrm{dof}}} & \cdots & \mathbf{0}_{n_{\mathrm{dof}}} \end{bmatrix}$$

$$\bar{\mathbf{I0}} = \begin{bmatrix} \mathbf{I}_{n_{\mathrm{dof}}} & \mathbf{0}_{n_{\mathrm{dof}}} \\ \vdots & \vdots \\ \mathbf{I}_{n_{\mathrm{dof}}} & \mathbf{0}_{n_{\mathrm{dof}}} \end{bmatrix} \qquad \bar{\mathbf{\Gamma}} = -\frac{V}{b}\begin{bmatrix} \varrho_1\mathbf{I}_{n_{\mathrm{dof}}} & \cdots & \mathbf{0}_{n_{\mathrm{dof}}} \\ \vdots & \ddots & \vdots \\ \mathbf{0}_{n_{\mathrm{dof}}} & \cdots & \varrho_{n_{\mathrm{lag}}}\mathbf{I}_{n_{\mathrm{dof}}} \end{bmatrix} \tag{23}$$

and, also,

$$\mathbf{M}_a = \mathbf{M} - q\left(\frac{b}{V}\right)^2 \mathbf{Q}_2 \quad ; \quad \mathbf{D}_a = \mathbf{D} - q\left(\frac{b}{V}\right)\mathbf{Q}_1 \quad ; \quad \mathbf{K}_a = \mathbf{K} - q\mathbf{Q}_0 \tag{24}$$

where $q = \rho V^2/2$ is the dynamic pressure and IT determines the flight condition. $\mathbf{0}_{n_{\mathrm{dof}}}$ and $\mathbf{I}_{n_{\mathrm{dof}}}$ are the $n_{\mathrm{dof}} \times n_{\mathrm{dof}}$ matrices of zeros and the identity matrix, respectively. Each $\mathbf{Q}_j$, with $j = 0, ..., (n_{\mathrm{lag}} + 2)$ contains the aerodynamics effects and they are obtained by the Roger's method (see section A.4). The structural matrices of mass, damping and stiffness $\mathbf{M}$, $\mathbf{D}$ and $\mathbf{K}$ are presented particularly for 3-DOF and 4-DOF airfoils in next sections. Note that the subscript $(.)_a$ indicates the aeroelastic matrix which accounts for both structural and aerodynamic effects.

A.2 3-DOF airfoil matrices

The structural damping matrix is neglected in this work. Mass and stiffness[I] matrices are given by

$$\mathbf{M} = \begin{bmatrix} m & S_\alpha & S_\beta \\ S_\alpha & I_\alpha & I_\beta + b(c-a)S_\beta \\ S_\beta & I_\beta + b(c-a)S_\beta & I_\beta \end{bmatrix}; \qquad \mathbf{K} = \mathrm{diag}(k_h,\ k_\alpha,\ k_\beta) \tag{25}$$

$$\begin{aligned} I_\alpha &= b^2\left[m_w {g_w}^2 + m_{CS}\left(g_{CS} + c - a\right)^2\right] + I_w + I_{CS} \\ I_\beta &= b^2\left[m_{CS} {g_{CS}}^2\right] + I_{CS} \end{aligned} \tag{26}$$

$$\begin{aligned} S_\alpha &= b\left[m_w g_w + m_{CS}\left(g_{CS} + c - a\right)\right] \\ S_\beta &= b\left[m_{CS} g_{CS}\right] \end{aligned} \tag{27}$$

where $m = m_w + m_{CS}$ is the total mass, and m_w is the mass of the wing only and m_{CS} is the mass of control surface only. g_w is the the non-dimensional distances w.r.t b from the elastic center of the wing to the gravitational center of the wing only $g.c.^w$; g_{CS} is from the elastic center of the CS to the gravitational center of the CS only $g.c.^{CS}$(see Fig. 2). Also, I_w is the inertia moment of mass of the main wing only around its own gravitational center

[I]In chapter 4, the linear equivalent matrix $\hat{\mathbf{K}} = \mathrm{diag}(k_h, k_\alpha, \hat{k}_\beta)$ is employed in Eq. (24) instead of $\mathbf{K}$ to compute the linear equivalent aeroelastic matrix $\hat{\mathbf{A}}$ (instead of $\mathbf{A}$), used in the equivalent linear stability analysis on the Equivalent Linearization Technique (ELT). Also, the structural damping matrix $\mathbf{D}$ is assumed to be zero, and, a linear equivalent $\hat{\mathbf{D}} = \mathrm{diag}(0, 0, \hat{d}_\beta)$ is defined to employ the iterative procedure of ELT.

$g.c.^w$, and I_{CS} is the inertia moment of mass of the CS only around its own gravitational center $g.c.^{CS}$. The description of other geometrical and mass properties for the 3-DOF airfoil is shown in Tab. 1. The aerodynamic matrices used in Eq. (6) consider the first, second and third rows and columns of the matrices in Eq. (31).

A.3 4-DOF airfoil matrices

The structural matrices for the 4-DOF system are given by (THEODORSEN; GARRICK, 1942; AL-MASHHADANI *et al.*, 2017)

$$\mathbf{K} = \operatorname{diag}(k_h,\ k_\alpha,\ k_\beta,\ k_\gamma)$$
$$\mathbf{M} = \begin{bmatrix} m & S_\alpha & S_\beta & S_\gamma \\ S_\alpha & I_\alpha & I_\beta + b(c-a)S_\beta & I_\gamma + b(d-a)S_\gamma \\ S_\beta & I_\beta + b(c-a)S_\beta & I_\beta & I_\gamma + b(d-c)S_\gamma \\ S_\gamma & I_\gamma + b(d-a)S_\gamma & I_\gamma + b(d-c)S_\gamma & I_\gamma \end{bmatrix} \tag{28}$$

$$\begin{aligned} I_\alpha &= b^2\left[m_w {g_w}^2 + m_{CS}\left(g_{CS} + c - a\right)^2 + m_t\left(g_t + d - a\right)^2\right] + I_w + I_{CS} + I_t \\ I_\beta &= b^2\left[m_{CS}{g_{CS}}^2 + m_t\left(g_t + d - c\right)^2\right] + I_{CS} + I_t \\ I_\gamma &= b^2\left[m_t g_t^2\right] + I_t \end{aligned} \tag{29}$$

$$\begin{aligned} S_\alpha &= b\left[m_w g_w + m_{CS}\left(g_{CS} + c - a\right) + m_t\left(g_t + d - a\right)\right] \\ S_\beta &= b\left[m_{CS} g_{CS} + m_t\left(g_t + d - c\right)\right] \\ S_\gamma &= b\left[m_t g_t\right] \end{aligned} \tag{30}$$

where $m = m_w + m_{CS} + m_t$ is the total mass, and m_w is the mass of the wing only, m_{CS} is the mass of control surface only and m_t is the mass of tab only. g_w is the the non-dimensional distances w.r.t b from the elastic center of the wing to the gravitational center of the wing only $g.c.^w$; g_{CS} is from the elastic center of the CS to the gravitational center of the CS only $g.c.^{CS}$; and, g_t is from the elastic center of the tab to the gravitational center of the tab only $g.c.^t$ (see Fig. 3). Also, I_w is the inertia moment of mass of the main wing only around its own gravitational center $g.c.^w$; also, I_{CS} is the inertia moment of mass of the CS only around its own gravitational center $g.c.^{CS}$; and I_t is the inertia moment of mass of the tab only around its own gravitational center $g.c.^t$. The description of other geometrical and mass properties for the 4-DOF airfoil is shown in Tab. 1.

The aerodynamic matrices used in Eq. (6) are given by

$$\mathbf{M}_{nc} = \begin{bmatrix} -\pi & \pi a & T_1 & T_1^d \\ \pi a & -\left(\frac{1}{8} + a^2\right)\pi & -2T_{13} & -2T_{13}^d \\ T_1 & -2T_{13} & \frac{T_3}{\pi} & \frac{Y_6}{\pi} \\ T_1^d & -2T_{13}^d & \frac{Y_6}{\pi} & \frac{T_3^d}{\pi} \end{bmatrix} \circ [\mathbf{p}\mathbf{p}^T]$$

$$\mathbf{D}_{nc} = \begin{bmatrix} 0 & -\pi & T_4 & T_4^d \\ 0 & \pi\left(a - \frac{1}{2}\right) & -T_{16} & -T_{16}^d \\ 0 & -T_{17} & -\frac{T_{19}}{\pi} & -\frac{Y_{10}}{\pi} \\ 0 & -T_{17}^d & -\frac{Y_{18}}{\pi} & -\frac{T_{19}^d}{\pi} \end{bmatrix} \circ [\mathbf{p}\mathbf{p}^T]$$

$$\mathbf{K}_{nc} = \begin{bmatrix} 0 & 0 & 0 & 0 \\ 0 & 0 & -T_{15} & -T_{15}^d \\ 0 & 0 & -\frac{T_{18}}{\pi} & -\frac{Y_9}{\pi} \\ 0 & 0 & -\frac{Y_{17}}{\pi} & -\frac{T_{18}^d}{\pi} \end{bmatrix} \circ [\mathbf{p}\mathbf{p}^T] \tag{31}$$

$$\mathbf{R} = \left[\left\{-2\pi \quad 2\pi\left(a + \tfrac{1}{2}\right) \quad -T_{12} \quad -T_{12}^d\right\} \circ \mathbf{p}^T\right]^T$$

$$\mathbf{S}_1 = \left\{0 \quad 1 \quad \tfrac{T_{10}}{\pi} \quad \tfrac{T_{10}^d}{\pi}\right\} \circ \mathbf{p}^T$$

$$\mathbf{S}_2 = \left\{1 \quad \left(\tfrac{1}{2} - a\right) \quad \tfrac{T_{11}}{2\pi} \quad \tfrac{T_{11}^d}{2\pi}\right\} \circ \mathbf{p}^T$$

where $\mathbf{p} = [1 \quad b \quad b \quad b]^T$ and $\circ$ is the Hadamard product, i.e., the multiplication is performed element by element. See section A.5 for T_i, T_i^d and Y_i expressions.

A.4 Roger's Method to Approximate Aerodynamics

This method is detailed by Ribeiro, Dowell and Bueno (2021) and it refers to the minimum square methods to write Eq. (6) by an approximated expression (Eq. 7).

The coefficients to be converged that are present in the approximated expression are $\mathbf{C}_Q = \begin{bmatrix} \mathbf{Q}_0 & \mathbf{Q}_1 & \mathbf{Q}_2 & \dots & \mathbf{Q}_{n_{\text{lag}}+2} \end{bmatrix}$, where each $\mathbf{Q}_i$ is a $n_{\text{dof}} \times n_{\text{dof}}$ matrix. Note that they appear explicitly in the dynamic matrix (Eq. 22). The coefficients can be solved by

$$\mathbf{C}_Q = \mathbf{P}_1^{-1}\mathbf{P}_2 \tag{32}$$

This work consider $n_{\text{lag}} = 7$ and ϱ_j is the j-th lag parameter. Also,

$$\mathbf{P}_2 = -\textstyle\sum_{u=1}^{N_k} \left(\mathbf{Q}_{a,u}^R \mathbf{B}_u^R + \mathbf{Q}_{a,u}^I \mathbf{B}_u^I\right) \qquad \mathbf{P}_1 = \textstyle\sum_{u=1}^{N_k} \left(\mathbf{B}_u^R \mathbf{B}_u^R + \mathbf{B}_u^I \mathbf{B}_u^I\right) \tag{33}$$

where the notation $(.)^R$ and $(.)^I$ refer to real and imaginary parts of $(.)$, respectively. N_k is the number of reduced frequencies used to evaluate the Eq. (6) and $\mathbf{Q}_{a,u}$ (Eq. 6) must be computed for the u-th reduced frequency k_u. Finally,

$$\mathbf{B}_u^R = \begin{bmatrix} 1 & 0 & -k_u^2 & \frac{k_u^2}{k_u^2+\varrho_1^2} & \dots & \frac{k_u^2}{k_u^2+\varrho_{n_{\text{lag}}}^2} \end{bmatrix};\ \mathbf{B}_u^I = \begin{bmatrix} 0 & k_u & 0 & \frac{\varrho_1 k_u}{k_u^2+\varrho_1^2} \dots & \frac{\varrho_{n_{\text{lag}}} k_u}{k_u^2+\varrho_{n_{\text{lag}}}^2} \end{bmatrix} \tag{34}$$

A.5 Theodorsen's Constants

Each constant T_i captures the effect of the main control surface and it depends on c and a (they are given in Eq. 35). Each constant T_i^d captures the effect of the tab and it depends on d and a. T_i^d can be computed by using d instead of c on the expression for T_i. Finally, Y_i captures the combined effect of both trailing-edge control surfaces (see Eq. 36 (THEODORSEN; GARRICK, 1942)). Note that particularly T_9, T_{13}, T_{16}, T_{17}, T_{23}, T_{13} carry the effect of pitch through a.

$$\begin{aligned}
T_1 &= \frac{-(2+c^2)}{3} s_c + c\ o_c \\
T_2 &= c(1-c^2) - (1+c^2) s_c\ o_c + c\ o_c^2 \\
T_3 &= \frac{-(1-c^2)}{8}(5c^2+4) + \frac{1}{4} c(7+2c^2) s_c\ o_c - \left(\frac{1}{8} + c^2\right) o_c^2 \\
T_4 &= c s_c - o_c \\
T_5 &= -(1-c^2) - o_c^2 + 2c s_c\ o_c \\
T_7 &= \frac{c}{8}(7+2c^2) s_c - \left(\frac{1}{8} + c^2\right) o_c \\
T_8 &= -(1+2c^2)\frac{s_c}{3} + c\ o_c \\
T_9 &= \frac{1}{2}\left(\tfrac{s_c}{3}(1-c^2) + a T_4\right)
\end{aligned} \tag{35}$$

$$
\begin{aligned}
T_{10} &= s_c + o_c \\
T_{11} &= (2-c)s_c + (1-2c)o_c \\
T_{13} &= -\frac{1}{2}\left(T_7 + (c-a)T_1\right) \\
T_{12} &= (2+c)s_c - (1+2c)o_c \\
T_{15} &= T_4 + T_{10} \\
T_{16} &= T_1 - T_8 - (c-a)T_4 + \frac{T_{11}}{2} \\
T_{17} &= -2T_9 - T_1 + \left(a - \frac{1}{2}\right)T_4 \\
T_{18} &= T_5 - T_4 T_{10} \\
T_{19} &= -\frac{1}{2}T_4 T_{11}
\end{aligned}
\tag{35}
$$

where $s_c = \sqrt{1-c^2}$ and $o_c = \arccos(c)$

$$
\begin{aligned}
Y_1 &= -s_c\ s_d - o_c\ o_d + d\ s_d\ o_c + c\ s_c\ o_d - (d-c)^2\ \log N_T \\
Y_3 &= \frac{(c+2\ d)}{3}\ s_c\ s_d + d\ o_c\ o_d - \frac{(2+d^2)}{3}\ s_d\ o_c - \frac{(1+3\ c\ d-c^2)}{3}\ s_c\ o_d + \frac{(d-c)^3}{3}\ \log N_T \\
Y_4 &= \frac{(d+2\ c)}{3}\ s_d\ s_c + c\ o_d\ o_c - \frac{(2+c^2)}{3}\ s_c\ o_d - \frac{(1+3\ d\ c-d^2)}{3}\ s_d\ o_c + \frac{(c-d)^3}{3}\ \log N_T \\
Y_6 &= \frac{-s_c\ s_d}{2}\ \left(1 + \frac{c^2}{6} + \frac{d^2}{6} + c\ d\ \frac{11}{12}\right) - \left(\frac{1}{8} + c\ d\right)\ o_c\ o_d + \\
&\quad + \frac{1}{3}\left[\tfrac{d}{4}\ \left(\tfrac{5}{2} - d^2\right) + c\ \left(2+d^2\right)\right]\ s_d\ o_c + \\
&\quad + \frac{1}{3}\left[\tfrac{c}{4}\ \left(\tfrac{5}{2} - c^2\right) + d\ \left(2+c^2\right)\right]\ s_c\ o_d + \frac{(d-c)^4}{12}\ \log N_T \\
Y_9 &= Y_1 - T_4\ T_{10}^d \\
Y_{17} &= Y_1 - T_4^d\ T_{10} \\
Y_{10} &= Y_3 - Y_4 - T_4\ T_{11}^d/2 \\
Y_{18} &= Y_4 - Y_3 - T_4^d\ T_{11}/2
\end{aligned}
\tag{36}
$$

where $s_c = \sqrt{1-c^2}$, $o_c = \arccos(c)$, $s_d = \sqrt{1-d^2}$ and $o_d = \arccos(d)$. Also, $N_T = \left|\dfrac{(1-cd-s_c s_d)}{(d-c)}\right|$.

A.5.1 Non-Dimensional Structural Dynamics

The equations of motion in Eq. (5) are typically written in a non-dimensional form by dividing the plunge equation by mb, and the others equations by mb^2, then, the result for 4-DOF airfoil, highlighting the structural part only, is given by

$$
\begin{aligned}
&\ddot{\bar{h}} + x_\alpha \ddot{\alpha} + x_\beta \ddot{\beta} + x_\gamma \ddot{\gamma} + \frac{k_h}{m}\bar{h} = 0 \\
&x_\alpha \ddot{\bar{h}} + r_\alpha^2 \ddot{\alpha} + \left[r_\beta^2 + (c-a)x_\beta\right]\ddot{\beta} + \left[r_\gamma^2 + (d-a)x_\gamma\right]\ddot{\gamma} + \frac{k_\alpha}{mb^2}\alpha = 0 \\
&x_\beta \ddot{\bar{h}} + \left[r_\beta^2 + (c-a)x_\beta\right]\ddot{\alpha} + r_\beta^2 \ddot{\beta} + \left[r_\gamma^2 + (d-c)x_\gamma\right]\ddot{\gamma} + \frac{k_\beta}{mb^2}\beta = 0 \\
&x_\gamma \ddot{\bar{h}} + \left[r_\gamma^2 + (d-a)x_\gamma\right]\ddot{\alpha} + \left[r_\gamma^2 + (d-c)x_\gamma\right]\ddot{\beta} + r_\gamma^2 \ddot{\gamma} + \frac{k_\gamma}{mb^2}\gamma = 0
\end{aligned}
\tag{37}
$$

where $\bar{h} = h/b$.

An important note is that the non-dimensional parameters $x_{(\ )}$ and $r_{(\ )}$ appears particularly as a result of this divisions, i.e., $x_{(\ )} = S_{(\ )}/(mb)$ and $r_{(\ )}^2 = I_{(\ )}/(mb^2)$, for $(\ ) = h, \alpha, \beta, \gamma$, and their description must be carefully interpreted since there some small mistakes in typical literature for such system.

APPENDIX B – Details of Time Integration

As introduced in section 3.1, a general explicit method to integrate a first order ODE $\dot{\mathbf{y}} = \mathbf{g}(v, \mathbf{y})$, where v is the independent variable and $\mathbf{y}$ is the state vector with the dependent variables, has the marching equation given by $\mathbf{y}_{i+1} = \mathbf{y}_i + s_v\ F(v_i, \mathbf{y}_i)$, for s_v the integration step. The fourth order Runge-Kutta (RK4) is defined by

$$
\begin{aligned}
F(v_i, \mathbf{y}_i) &= \frac{1}{6}\left(\mathbf{k}_1 + 2\mathbf{k}_2 + 2\mathbf{k}_3 + \mathbf{k}_4\right) \\
\\
\mathbf{k}_1 &= \mathbf{g}\left(v_i, \mathbf{y}_i\right) \\
\mathbf{k}_2 &= \mathbf{g}\left(v_i + \tfrac{s_v}{2}, \mathbf{y}_i + \tfrac{s_v}{2}\mathbf{k}_1\right) \\
\mathbf{k}_3 &= \mathbf{g}\left(v_i + \tfrac{s_v}{2}, \mathbf{y}_i + \tfrac{s_v}{2}\mathbf{k}_2\right) \\
\mathbf{k}_4 &= \mathbf{g}\left(v_i + s_v, \mathbf{y}_i + s_v\mathbf{k}_3\right)
\end{aligned}
\tag{38}
$$

Also, the fith order Runge-Kutta method (RK5) is given by (GERALD; WHEATLEY, 1994)

$$
\begin{aligned}
F(v_i, \mathbf{y}_i) &= \frac{16}{135}\mathbf{k}_1 + \frac{6656}{12825}\mathbf{k}_3 + \frac{28561}{56430}\mathbf{k}_4 - \frac{9}{50}\mathbf{k}_5 + \frac{2}{55}\mathbf{k}_6 \\
\\
\mathbf{k}_1 &= \mathbf{g}\left(v_i, \mathbf{y}_i\right) \\
\mathbf{k}_2 &= \mathbf{g}\left(v_i + \tfrac{s_v}{4}, \mathbf{y}_i + \tfrac{s_v}{4}\mathbf{k}_1\right) \\
\mathbf{k}_3 &= \mathbf{g}\left(v_i + \tfrac{3}{8}s_v, \mathbf{y}_i + \tfrac{s_v}{32}\left[3\mathbf{k}_1 + 9\mathbf{k}_2\right]\right) \\
\mathbf{k}_4 &= \mathbf{g}\left(v_i + \tfrac{12}{13}s_v, \mathbf{y}_i + \tfrac{s_v}{2197}\left[1932\mathbf{k}_1 - 7200\mathbf{k}_2 + 7296\mathbf{k}_3\right]\right) \\
\mathbf{k}_5 &= \mathbf{g}\left(v_i + s_v, \mathbf{y}_i + s_v\left[\tfrac{439}{216}\mathbf{k}_1 - 8\mathbf{k}_2 + \tfrac{3680}{513}\mathbf{k}_3 - \tfrac{845}{4104}\mathbf{k}_4\right]\right) \\
\mathbf{k}_6 &= \mathbf{g}\left(v_i + \tfrac{s_v}{2}, \mathbf{y}_i + s_v\left[-\tfrac{8}{27}\mathbf{k}_1 + 2\mathbf{k}_2 - \tfrac{3544}{2565}\mathbf{k}_3 + \tfrac{1859}{4104}\mathbf{k}_4 - \tfrac{11}{40}\mathbf{k}_5\right]\right)
\end{aligned}
\tag{39}
$$

Particularities of the iteration in time *vs* Hénon's iteration

The Runge-Kutta equations applied in a regular iteration in time for the aeroelastic systems studied in this work consider the independent variable $v \equiv t$ and the state vector of dependent variables $\mathbf{y} \equiv \mathbf{x}$. The ODE to be integrated $\dot{\mathbf{x}} = \mathbf{h}(t, \mathbf{x})$ is given in Eq. (10), in a way that in the Runge-Kutta equation context, $\mathbf{g} \equiv \mathbf{h}$. The regular time step is $s_v \equiv \Delta t$. In contrast, in the context of discontinuous nonlinear equations, when a switching point is jumped, the Hénon's iteration is performed by integrating the ODE $\tilde{\mathbf{x}}' = \tilde{\mathbf{h}}(x_k, \tilde{\mathbf{x}})$ with the independent variable $v \equiv x_k$ and the state vector of dependent variables $\mathbf{y} \equiv \tilde{\mathbf{x}}$. Finally, note that $\mathbf{g} \equiv \tilde{\mathbf{h}}$, derived as a contribution of this work and given in Eq. (13). The step to reach the switching point is $s_v \equiv x_k^{sp} - x_{k,i}$.

Note that computing $\tilde{\mathbf{h}}(x_k, \tilde{\mathbf{x}})$ according to Eq. (13) includes to compute $\mathbf{h}(t, \mathbf{x})$, and for the Hénon's iteration, t can be found in the k-th row of $\tilde{\mathbf{x}}$. Also, the k-th row of $\mathbf{x}$ contains the independent variable x_k for this iteration. So, the increments of independent and dependent variables during the computation of $\mathbf{k}_{(\ )}$ in Runge-Kutta methods must be done carefully.

Particularities of the Hénon's iteration for single freeplay

It is possible that an inversion of the motion occurs between two consecutive time instants t_i and t_{i+1} and the position of this extreme is outside the freeplay, although for both time instants, u_l is inside the freeplay. Therefore, even if a single freeplay is the only discontinuous nonlinearity in the system, it is recommended that the extremes of u_l occurring between all pairs t_i and t_{i+1} to be computed to check if the freeplay region is changed from t_i and the extreme point. If so, it is possible to employ the Hénon iteration to achieve the freeplay boundary before computing the extreme value, assuring that the correct corresponding equation is properly considered.

Particularities of the Hénon's technique for multiple freeplay

If freeplay is considered in two DOFs, for example, it is possible that between two consecutive time instants t_i and t_{i+1}, both freeplays have their zones changed. In such cases, the Hénon iteration must be performed for each freeplay to define the correct sequence of crossed switching points. This can be achieved by examining the zones for all nonlinearities within the system during each Hénon iteration. The sequence is carefully selected to ensure that the nonlinearity undergoing the Hénon technique reaches its switching point without causing zone changes in other nonlinearities. Therefore, more than one Hénon iteration may be required between t_i and t_{i+1} to assure that the correct corresponding equation is used.

Convergence of Methods

The conventional Runge-Kutta method (RK) with a time step of $\Delta t = 1.10^{-6}$ is utilized as the reference solution to assess the convergence of both RK and the Runge-Kutta method improved with Hénon's technique (H). Different time steps are employed for running the numerical simulations with RK and H. The reference solution is synchronized with these latter solutions to enable a time-by-time comparison, and the root mean square of the relative difference vector is computed.

The results are plotted against the time step for both RK and H, as shown in Figure 50a. These findings indicate that the H method exhibits an optimum time step of approximately $\Delta t \approx 5.10^{-4}$ s. Notably, this value aligns with the recommended optimum time step of $1/(20\omega_{max})$ suggested by Bai, Wu and Yang (2023), where ω_{max} represents the maximum modal frequency of the considered model modes. In this specific case, for airfoil $\mathcal{A}_1$ at $V = 30$ m/s, ω_{max} is equal to 111.5 rad/s, resulting in an optimum time step of 4.5×10^{-4} s. Furthermore, it is evident that H, when utilizing $\Delta t = 1.10^{-3}$ s, achieves a level of accuracy comparable to RK with $\Delta t = 1.10^{-5}$ s. This underscores a significant advantage of enhancing the Runge-Kutta method with Hénon's technique: it allows for the use of larger time steps, considerably reducing computation time while still ensuring convergence, as illustrated in Figure 50b.

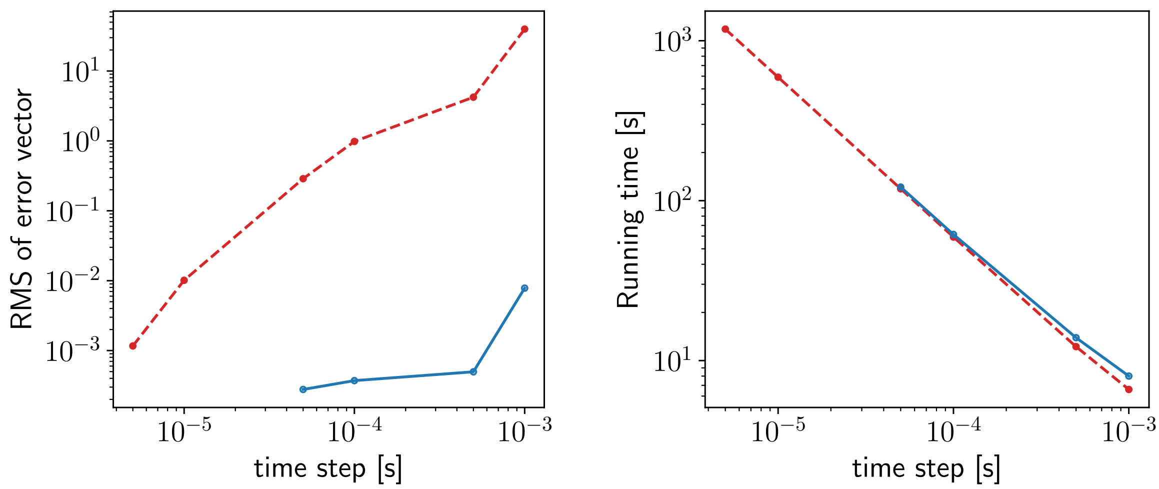

(a) (b)

Figure 50 – (a) RMS of the relative error between solutions of RK (dashed line) and H (solid line) when compared respectively with the reference solution (RK with $\Delta t = 1.10^{-6}$ s). (b) Running time for each time step.

APPENDIX C – Coefficients of Fourier Series

This appendix shows details of computing the coefficients of Fourier series of the nonlinear efforts of freeplay (f_l^δ) and of friction (f_l^C). Equation (40) shows explicitly how to compute the coefficients F_{c_n}, F_{s_n} for freeplay referring to the n-th harmonic, where N_{reg} is the number of sub-linear regions in a complete period from 0 to 2π in which the nonlinear effort f_l^δ is not zero ($f_l^\delta \neq 0$), and therefore, must be considered in the integration. This number may change according to the supposed motion, since this assumption modifies the number of times that the freeplay boundary is crossed.

$$
\begin{aligned}
F_{c_n} &= \frac{1}{\pi}\int_0^{2\pi} f_l^\delta \cos(n\theta)\, d\theta = \frac{1}{\pi}\sum_{i=1}^{N_{reg}} F_{c_n,i}^\delta \qquad & F_{s_n} &= \frac{1}{\pi}\int_0^{2\pi} f_l^\delta \sin(n\theta)\, d\theta = \frac{1}{\pi}\sum_{i=1}^{N_{reg}} F_{s_n,i}^\delta \\
&\text{where,} \\
F_{c_n,i} &= \int_{\theta_{i_1}}^{\theta_{i_2}} f_{l,i}^\delta \cos(n\theta)\, d\theta & F_{s_n,i} &= \int_{\theta_{i_1}}^{\theta_{i_2}} f_{l,i}^\delta \sin(n\theta)\, d\theta
\end{aligned}
\tag{40}
$$

where i refers to each one of those linear regions; θ_{i_1} and θ_{i_2} are the inferior and superior limits to integrate the i-th region; F_{c_n}, F_{s_n} are the coefficients of Fourier series. Based on nonlinear effort due to freeplay f_l^δ of Eq. (1), an expression for the i-th region is generalized as a line equation $f_{l,i}^\delta(t) = \bar{f}_i + \bar{k}_i \hat{u}_l(t)$, where $\bar{f}_i = f_{0,i} - \bar{k}_i u_{l0,i}$.

Although shown explicitly for freeplay, this equation can also be used to compute the coefficients of the Fourier series $F_{c_n}^C$, $F_{s_n}^C$ of friction, where the nonlinear effort f_l^C is in Eq. (2). For this case, $f_{l,i}^C(t) = f_{c,i}$ indicates the equation for friction. Specific parameters of such equations are detailed in tables of this appendix.

Motion with a single harmonic: $\hat{u}_l = U_1 \sin\theta$

When a single harmonic is supposed for the motion, the results of the integration for a general i-th region are presented for the first harmonic ($n = 1$), in Eq. (41) and (42) for freeplay ($F_{c_1,i}$, $F_{s_1,i}$) and for friction ($F^C_{c_1}$, $F^C_{s_1}$), respectively.

$$\begin{aligned} F_{c_1,i} &= \bar{f}_i[\sin\theta_{i_2} - \sin\theta_{i_1}] + \frac{\bar{k}_i U_1}{2}[\sin^2\theta_{i_2} - \sin^2\theta_{i_1}] \\ F_{s_1,i} &= \bar{f}_i[\cos\theta_{i_1} - \cos\theta_{i_2}] + \frac{\bar{k}_i U_1}{2}\left[\theta_{i_2} - \theta_{i_1} - \frac{(\sin 2\theta_{i_2} - \sin 2\theta_{i_1})}{2}\right] \end{aligned} \tag{41}$$

$$\begin{aligned} F^C_{c_1,i} &= f_{c,i}(\sin\theta_{i_2} - \sin\theta_{i_1}) \\ F^C_{s_1,i} &= f_{c,i}(\cos\theta_{i_1} - \cos\theta_{i_2}) \end{aligned} \tag{42}$$

For this case, there are $N_{reg} = 2$ for freeplay and $N_{reg} = 4$ for friction (see Fig. 23) and the Tab. 6 and 7 present the values of θ_{i_1}, θ_{i_2} and the required parameters of $f^\delta_{l,i}(t)$ and $f^C_{l,i}(t)$ for each i-th region to be integrated, respectively, for freeplay and friction. The results of each i-th region can be computed employing its respective parameters of the tables in Eq. (41) and (42). After that, they are summed as Eq. (40) indicates, obtaining the final coefficients for the first harmonic,

$$F_1 \equiv F_{s_1} = U_1 k_{u_l}\left[\pi - 2\theta_\delta - \sin(2\theta_\delta)\right]/\pi \tag{43}$$

for freeplay, where $\theta_\delta = \arcsin(\delta/U_1)$; and

$$F^C_{c_1} = 4C\left[1 - \tfrac{\delta}{U_1}\right]/\pi \tag{44}$$

for friction (note that $F_{c_1} = 0$ and $F^C_{s_1} = 0$).

Region $i = i_\delta$	θ_{i_1}	θ_{i_2}	$f_{0,i}$	$u_{l0,i}$	$\bar{k}_i$
1	θ_δ	$\pi - \theta_\delta$	0	δ	k_{u_l}
2	$\pi + \theta_\delta$	$2\pi - \theta_\delta$	0	$-\delta$	k_{u_l}

where $f_{0,i}$ and $u_{l0,i}$ are the effort and the displacement on the beginning of linear region i, whose stiffness (slope) is $\bar{k}_i$ (see Eq. 1)

Table 6 – Parameters of the nonlinear effort due to freeplay of each region from 0 to 2π when the assumed motion is $\hat{u}_l = U_1 \sin\theta$.

Region $i = i_c$	θ_{i_1}	θ_{i_2}	$f_{c,i}$
1	θ_δ	$\pi/2$	C
2	$\pi/2$	$\pi - \theta_\delta$	$-C$
3	$\pi + \theta_\delta$	$3\pi/2$	$-C$
4	$3\pi/2$	$2\pi - \theta_\delta$	C

$f_{c,i}$ is the effort due to friction, in region i (see Eq. 2)

Table 7 – Parameters of the nonlinear effort due to friction of each region from 0 to 2π when the assumed motion is $\hat{u}_l = U_1 \sin\theta$.

Motion with first and third harmonics: $\hat{u}_l = U_1 \sin\theta + U_3 \sin 3\theta$

When the first and third harmonics are assumed for the motion, considering only the particular case studied in this work, i.e., only freeplay is present for this condition, the results of the integration for a general i-th region are presented for the first ($n = 1$) and third ($n = 3$) harmonics in Eq. (45) and (46), respectively.

$$F_{s_1,i} = \left[-\bar{f}_i \cos(\theta) + \frac{\theta U_1 \bar{k}_i}{2} - \frac{U_1 \bar{k}_i \sin(2\theta)}{4} + \frac{U_3 \bar{k}_i \sin(2\theta)}{4} - \frac{U_3 \bar{k}_i \sin(4\theta)}{8} \right] \Bigg|_{\theta_{i_1}}^{\theta_{i_2}} \tag{45}$$

$$F_{s_3,i} = \left[-\frac{\bar{f}_i \cos(3\theta)}{3} + \frac{\theta U_3 \bar{k}_i}{2} + \frac{U_1 \bar{k}_i \sin(2\theta)}{4} - \frac{U_1 \bar{k}_i \sin(4\theta)}{8} - \frac{U_3 \bar{k}_i \sin(6\theta)}{12} \right] \Bigg|_{\theta_{i_1}}^{\theta_{i_2}} \tag{46}$$

There are $N_{reg} = 4$ regions for freeplay (see Fig. 22) and the Tab. 8 present the values of parameters for each i-th region to be integrated for freeplay, which can be applied in Eq. (45) and (46). The results of all regions are summed as Eq. (40) indicates, obtaining the final coefficients for the first (Eq. 47) and third (Eq. 48) harmonics. Note that $F_{c_1} = F_{c_3} = 0$ for odd functions and because of that they are omitted here.

Region $i = i_\delta$	θ_{i_1}	θ_{i_2}	$f_{0,i}$	$u_{l0,i}$	$\bar{k}_i$
1	$\theta_{\delta 1}$	$\theta_{\delta 2}$	0	δ	k_{u_l}
2	$\pi - \theta_{\delta 2}$	$\pi - \theta_{\delta 1}$	0	δ	k_{u_l}
3	$\pi + \theta_{\delta 1}$	$\pi + \theta_{\delta 2}$	0	$-\delta$	k_{u_l}
4	$2\pi - \theta_{\delta 2}$	$2\pi - \theta_{\delta 1}$	0	$-\delta$	k_{u_l}

where $f_{0,i}$ and $u_{l0,i}$ are the effort and the displacement on the beginning of linear region i, whose stiffness (slope) is $\bar{k}_i$ (see Eq. 1)

Table 8 – Parameters of the nonlinear effort due to freeplay of each region from 0 to 2π when the assumed motion is $\hat{u}_l = U_1 \sin\theta + U_3 \sin 3\theta$.

$$
\begin{aligned}
F_1 \equiv F_{s_1} &= -\frac{k_\beta \delta}{\pi} \quad \big[4\cos\theta_{\delta 1} - 4\cos\theta_{\delta 2} + \\
&\quad +\bar{U}_1\left(2\theta_{\delta 1} - 2\theta_{\delta 2} - \sin 2\theta_{\delta 1} + \sin 2\theta_{\delta 2}\right) + \\
&\quad +\bar{U}_3\left(\sin 2\theta_{\delta 1} - \tfrac{1}{2}\sin 4\theta_{\delta 1} - \sin 2\theta_{\delta 2} + \tfrac{1}{2}\sin 4\theta_{\delta 2}\right)\big]
\end{aligned} \tag{47}
$$

$$
\begin{aligned}
F_3 \equiv F_{s_3} &= -\frac{k_\beta \delta}{6\pi} \quad \big[8\cos 3\theta_{\delta 1} - 8\cos 3\theta_{\delta 2} \\
&\quad +\bar{U}_1\left(6\sin 2\theta_{\delta 1} - 3\sin 4\theta_{\delta 1} - 6\sin 2\theta_{\delta 2} + 3\sin 4\theta_{\delta 2}\right) + \\
&\quad +\bar{U}_3\left(12\theta_{\delta 1} - 12\theta_{\delta 2} - 2\sin 6\theta_{\delta 1} + 2\sin 6\theta_{\delta 2}\right)\big]
\end{aligned} \tag{48}
$$

where $\bar{U}_1 = U_1/\delta$ and $\bar{U}_3 = U_3/\delta$. The non-dimensional form of these coefficients are $\bar{F}_1 = F_{s_1}/(k_\beta \delta)$ and $\bar{F}_3 = F_{s_3}/(k_\beta \delta)$.